이학박사 학위논문

A Study on Applications of High-Frequency Optical Satellite Data to Oceanic Disastrous Phenomena

: Focused on Oil Spill and Red Tide

해양 재해현상에 대한 고빈도 광학위성자료
응용에 관한 연구
: 유류 유출 및 적조를 중심으로

2017년 2월

서울대학교 대학원
과학교육과 지구과학전공

이 민 선

Abstract

The spatial distribution of an oil spill and its temporal dispersion within a coastal bay were investigated using high-resolution optical images. A neural network method was applied to Landsat and DubaiSat-2 images to detect the oil spill. We conducted field observations to measure spectral characteristics of the oil spill and the oil-free sea surface. We were able to detect and eliminate pixels corresponding to ships and ship shadows on the satellite image, resulting in successful oil spill detection. A new recursive neural network method using a near-infrared band was developed to classify oil types into thick or film-like oil and to estimate their areal extents. To understand potential causes of the temporal evolution of the oil spill, we performed numerical modeling with atmospheric and oceanic inputs. Overall, trajectories of oil particles controlled by tidal currents showed good agreement with the detection results from satellite data. Slight discrepancies occurred between satellite data and results from the model simulation using only tidal currents, particularly in the southeastward dispersion or in the spreading of film-like oils into the northern inner channels. This was attributed to the effect of wind-driven Ekman drift. This study suggests that tidal currents played an important role in the temporal dispersion of oil in the bay during initial phases, when wind conditions were relatively weak, and that the Ekman drift became the dominant control on oil movement during periods of weak tidal currents and strong winds.

Speckles in the suspended particulate matter (SPM) data of the Geostationary Ocean Color Imager (GOCI) were spatiotemporally analyzed. The speckles were classified into four types based on their appearance: isolated speckle, speckle near cloud, patch-type speckle, and slot-related speckle. The spectral characteristics of

the speckles were analyzed. We developed a speckle removal procedure to detect the speckles. The speckle removal improved the quality of the GOCI SPM data. We conclude that the speckles were generated by the unmasked clouds edge, water vapor, and small clouds that move during the spectral scanning sequences.

From field cruises around the Korean coast, we found that red tide had a bimodal spectral distribution, having two peaks at 555 nm and 680 nm. A red tide index (RTI) algorithm was developed based on *in situ* spectral characteristics of red tide bloom and validated by *in situ* red tide measurements. The RTI algorithm was applied to reprocessed GOCI data with speckle removal for the period from 2011 to 2016. The phenology of red tide, such as starting time, ending time, duration, and spatial probability, was estimated using satellite RTI data. Migration and propagation of red tide along and across the coast was investigated spatially and temporally. The relationship between RTI and environmental parameters, such as sea surface temperature, cloudiness, sea surface wind, river discharge, colored dissolved organic matter, Chlorophyll-a, SPM, were clarified.

Keyword : Oil spill, Speckle, Red tide, Optical feature, Satellite remote sensing, Geostationary Ocean Color Imager

Student Number : 2011-30457

Table of Contents

Acronyms

CDOM	Colored Dissolved Organic Matter
Chl-a	Chlorophyll-a
COMS	Communication Ocean and Meteorological Satellite
CZCS	Coastal Zone Color Scanner
ECMWF	European Centre for Medium-Range Weather Forecasts
EFDC	Environmental Fluid Dynamics Code
GOCI	Geostationary Ocean Color Imager
KHOA	Korea Hydrographic and Oceanographic Administration
NASA	National Aeronautics and Space Administration
NIFS	National Institute of Fisheries Science
NIR	Near-infrared
NN	Neural Network
OLI	Operational Land Imager
PAR	Photosynthetically Active Radiation
RMSE	Root Mean Square Errors
R_{rs}	Remote Sensing Reflectances
RTI	Red Tide Index
SAR	Synthetic Aperture Radar
Satrec-I	Satrec Initiative
SPM	Suspended Particulate Matter
SST	Sea Surface Temperature
USGS	U. S. Geological Survey
YOC	Yellow Sea Large Marine Ecosystem Ocean Color Work Group

List of Tables

Part I. Oil Spill

Part III. Red Tide

List of Figures

Part I. Oil Spill

Part II. Speckle

Part III. Red Tide

Overview

Remote sensing data is classified into three types based on wavelength: visible, infrared, and microwave. The infrared region typically represents clouds and sea surface temperature measurements. The microwave range is mainly used to measure sea surface roughness, height, and sea surface temperature. Visible radiation enables observations of visible phenomena, such as chlorophyll-a, suspended particulate matter (SPM), and colored dissolved organic matter. These satellite images have the advantage of periodically observing large areas and are also useful for monitoring disastrous events. Dividing disaster according to cause, there are natural disasters and man-made disasters. An example of an observable ocean natural disaster is red tide; examples of man-made disasters in the oceans are oil spills due to ship accidents or oil field collapses. These disastrous events can be observed with optical sensors and GOCI, the world's first geostationary ocean color sensor, onboard the Communication Ocean and Meteorological Satellite (COMS). GOCI provides ocean color data for the region around Korea eight times per day with a high temporal resolution of one hour.

Part I. Oil Spill

Chapter 1. Introduction

1.1. Previous Study

Oil spills have long occurred as a result of operative discharge from ships, accidents on ships, accidents on platforms, or other types of accident around the world' s oceans (National Research Council, 2003; Brekke and Solberg, 2005; Jha et al., 2008). There have been numerous, large-scale, accidental oil leakages, including the Deep Water Horizon incident in 2009 (Garcia-Pineda et al., 2009; Camilli et al., 2010; McNutt et al., 2012; Marghany, 2014), the Exxon-Valdez spill in 1989 (National Response Team, 1989; Bragg et al., 1994), and the Hebei Spirit accident in the sea off Korea in 2007 (Kim et al., 2010; Kim et al., 2015). All these events constituted huge disasters, for coastal areas in particular, and their effects ranged from short-term devastation of fisheries to long-term marine environmental damage lasting decades (Barron, 2012; White et al., 2012). Due to its various chemical constituents and poisonous materials, spilled oil can be enormously harmful to marine plants and animals, including small species of fish, coral reefs, and mangroves.

In an attempt to identify the discharge source and monitor the extent of oil spills for clean-up processes, ship and aircraft surveillance has often been utilized. In most cases, however, accidents are likely to occur under poor weather conditions. This

creates drawbacks in terms of time delays and narrow spatial coverage (Marghany, 2014; Mera et al., 2014). In contrast, satellite remote sensing, including visible and microwave frequency ranges, could offer the chance to overcome these spatial and temporal limitations (Jha et al., 2008; Fingas and Brown, 2014; Marghany, 2014). Due to increasing observational opportunities and satellite spatial resolution, oil spill detection using satellite data can play an important role in immediately identifying oil-contaminated regions (Leifer et al., 2012). Unlike human based observations using ships and aircraft, satellite images can provide near-real time maps of large-scale oil slick distributions (Hu et al., 2015).

Synthetic aperture radar (SAR) is an active microwave sensor, and thus it can provide good-quality images under all-weather atmospheric conditions. Many attempts have been made to develop algorithms to detect oil spills, using both single-polarized and full-polarized SAR imagery. The SAR data methodologies employed can be classified into four representative techniques: adaptive threshold methods (Vachon et al., 2000; Solberg et al., 1999; Kim et al., 2015), bimodal histogram methods (Skøelv and Wahl, 1993; Kim et al., 2013), neural network (NN) methods (Frate et al., 2000; Garcia-Pineda et al., 2009; Kim et al., 2015) for single-polarized data, and decomposition analysis and conformity coefficient methods for full-polarized SAR data (Migliaccio et al., 2007; Liu et al., 2011; Zhang et al., 2011; Li et al., 2014). Among these techniques, the neural network method has the advantage of identifying nonlinear

relationships between the satellite data and oil (Topouzelis et al., 2007), while other machine learning methods, including a decision tree method and a genetic algorithm, have also been developed and applied to oil spill detection (Mera et al., 2012; Marghany, 2014).

In spite of the many advantages of SAR imagery, SAR-based methodologies may give rise to some problems at small Normalized Radar Cross Section (NRCS) values, because many features tend to look alike over the calm sea surface in weak wind conditions. A moderate range of wind speeds (2–12 m/s) is reported to provide more preferable conditions for oil detection from SAR imagery than extremely low (< 2 m/s) or high wind speeds (> 12 m/s) (Bern et al., 1993; Brekke and Solberg, 2005). Additionally, the satellite' s long revisit period and the limited number of available observations represent another drawback of SAR data when attempting temporal sampling and analysis (Solberg et al., 1999; Zhao et al., 2014).

In addition to microwave remote sensing, satellite sensors measuring the visible/thermal-infrared channel can detect oil spills based on in-situ measurements comparing the spectral characteristics of oil to those of seawater (Macdonald et al., 1993; Salisbury et al., 1993; Hu et al., 2015), and can classify the oil spills based on appearance and thickness (Carpenter, 2007; Clark et al., 2010; Zhao et al., 2014; Hu et al., 2015). Compared with the many and diverse applications of SAR images to oil detection, studies that employ satellite optical sensors at visible and near-infrared wavelengths are rare. Most have focused on the overall spatial

distributions of oil from various multi-satellite images, while the spectral responses of oil spills detected by multi-spectral optical sensors have also been investigated to understand their characteristics and relationships to oil thickness (Hu et al., 2003; Wettle et al., 2009; Bulgarelli and Djavidnia, 2012). Recently, hyperspectral data from the Hyperion satellite have been used to examine the spatial extent of oil spills in the Bohai Sea (Lu et al., 2013). The methodology for the analysis of optical imagery is very similar to that employed for SAR images. In this respect, it is anticipated that high-resolution satellite optical images, such as those from DubaiSat-2 and Landsat, can effectively monitor spilled oil in a similar manner to SAR images under clear-sky conditions, using the same methodology as for SAR data. Application of the neural network method to optical imagery is also expected to discriminate oil pixels with high accuracy.

1.2. Objectives of This Study

On the January 31, 2014, the oil tanker WuYiSan crashed into an oil pipeline (Fig. 1c) at the Gwangyang bay in Korea (Fig 1a). The Gwangyang bay is located off the south coast of Korea. It is 17 km long, 9 km across, and relatively shallow, with a depth of less than 40 m, as shown in Fig. 1a. An estimated 754,000 L of crude oil, naphtha and oil mixtures from the pipeline leaked into the Gwangyang bay (Fig 1d). Fig 1b shows the oil spill distribution from a Landsat satellite image about two hours after the accident. In spite of the great endeavor to remove oil at the coastal area (Fig. 1e), oil deposited in the soil and mud flats is still present today.

The objectives of this study are (1) to develop techniques to discriminate pixels corresponding to ships and their shadows to allow for successful oil spill detection, (2) to detect the oil spill within the coastal area from high-resolution optical images using the neural network method, (3) to apply recursive neural network methods for the classification of thick and film-like oils from the satellite images, (4) to achieve an algorithm for oil detection by conducting a field campaign to measure the spectral characteristics of the oil spill by spectroradiometer and in-situ measurements, (5) to understand temporal movements of oil through both satellite images and numerical model simulations using tide and wind field inputs, and (6) to understand the atmospheric and oceanic environments affecting the evolution of oil spills by tracing oil-

contaminated water particles.

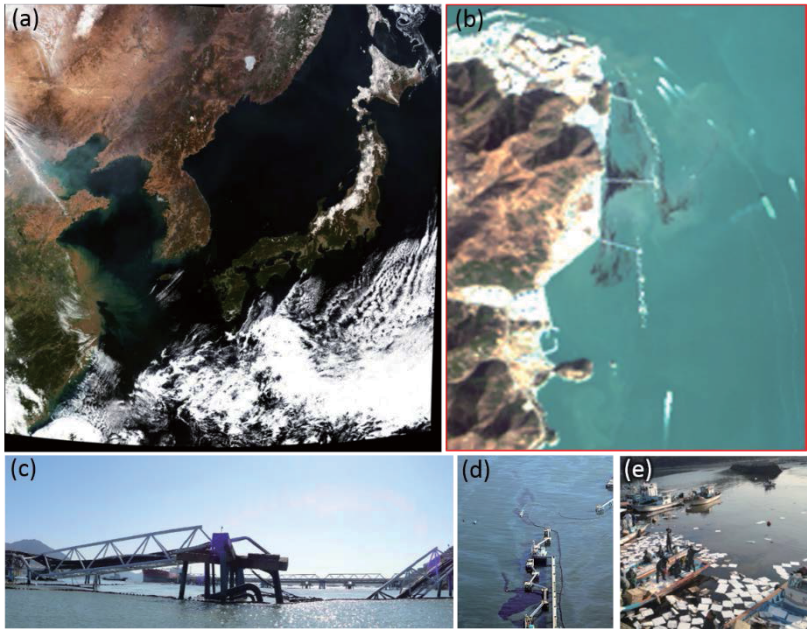

Fig. 1. (a) Satellite RGB image of the Korean peninsula including the study area, marked by red box, (b) enlarged Landsat image of the oil spill at 2:06 AM on January 31, 2014, (c) photo of the collapsed pipeline, (d) view of the pipeline and spilled oil, and © photo of the oil removal process at the coastal area.

Chapter 2. Data Description

2.1. Satellite Data

2.1.1. Landsat ETM+/OLI

Since the study region is a small bay, 17 km long and 9 km wide, off the southern coast of Korea (Fig. 1a and Fig. 2), satellite images with a high spatial resolution are required to observe small-scale features such as oil spills. SAR data, such as that from RADARSAT-2, COSMO-SkyMed and PALSAR-2 could provide such high-resolution spatial features, however, there were no observations by SAR sensors during the oil spill event studied here. As a result of this, and despite the presence of several satellites utilizing optical, infrared, and microwave sensors, we were only able to obtain a small number of optical images of the oil spill event from Landsat and DubaiSat-2 satellites.

The Landsat-8 Operational Land Imager (OLI), a series of Landsat satellites launched in 2013 by National Aeronautics and Space Administration (NASA), encompasses the research area with a swath area of 238 km × 233 km and a 16 day revisit period. It has four visible (443, 487.5, 562.5, 655 nm central wavelengths), one near infrared (865 nm), two short wave infrared (1.61, 2.25 μm), and two thermal infrared (10.90, 12.00 μm) wavelengths with 30 - 60

m spatial resolution. We obtained Landsat OLI data from the U. S. Geological Survey (USGS) website (http://earthexplorer.usgs.gov). Acquisition time of the Landsat image was 02:06 UT on January 31, 2014, which is about two hours after the accident. Detailed information on the satellite image specifications, such as center location, sun azimuth angle, and sun elevation of the image, is listed in Table 1.

Table 1. Specifications of satellite images used in this study.

Satellite	Landsat	DubaiSat-2	DubaiSat-2
Acquisition Time (UT)	02:06 UTC January 31, 2014	02:22 UTC February 2, 2014	02:40 UTC February 4, 2014
Wavelength (nm)	443, 487.5, 562.5, 655, 865	492, 552, 667, 832	492, 552, 667, 832
Resolution (m)	30×30	4×4	4×4
Center Location	127.33ºE, 34.60ºN	127.78ºE, 34.88ºN	127.73ºE, 34.75ºN 127.76ºE, 34.85ºN 127.79ºE, 34.94ºN
Sun Azimuth (º)	151.99	156.50	156.56
Sun Elevation (º)	33.20	34.47	34.41
Swath (km)	238 × 233	11 × 12	11 × 12

2.1.2. DubaiSat-2

DubaiSat-2, launched on November 21, 2013, is an Earth observing satellite built by the Emirates Institution for Advanced Science and Technology under an agreement with Satrec Initiative (Satrec-I), a satellite manufacturing company, in Korea. We obtained the DubaiSat-2 images from Satrec-I Imaging Services (http://www.si-imaging.com/). It can provide us with high-resolution multi-spectral images over the research area with a relatively short revisit period of about a few days. It has three visible (492, 552, 667 nm) and one near IR (832 nm) channel with a high spatial resolution of 4 m. Since DubaiSat-2 has the capability of changing its viewing angle, it can observe the research area several times in a few days at different angles, even if not from the same path. With this type of capability, a high-resolution optical image from DubaiSat-2 could be immediately scheduled to observe the bay only two days after the accident, at 02:22 UT on February 2 and 02:40 UT on February 4, 2014 (Figs. 2b and c). The first DubaiSat-2 image was obtained for only one scene but the second image covered a wider region composed of three adjacent scenes, as shown in Fig. 2c.

Fig. 3 shows spectral images of each wavelength band from DubaiSat-2, from 492 nm (Fig. 3b) to 832 nm (Fig. 3e). The oil spill is shown clearly in the enlarged near-IR image, the area of which is indicated by the red box in Fig. 3a. An interesting feature is that a significant number of ships and their shadows were detected in the images, which need to be eliminated or masked prior to oil detection. At short wavelength ranges (492, 552 nm) the reflectance values corresponding to oil pixels were relatively small compared to their neighboring non-oil pixels, as shown in Figs. 3b and c. In contrast to this, long-wavelength bands exhibited a reverse trend with relatively high reflectances for oil pixels and small values for non-oil pixels.

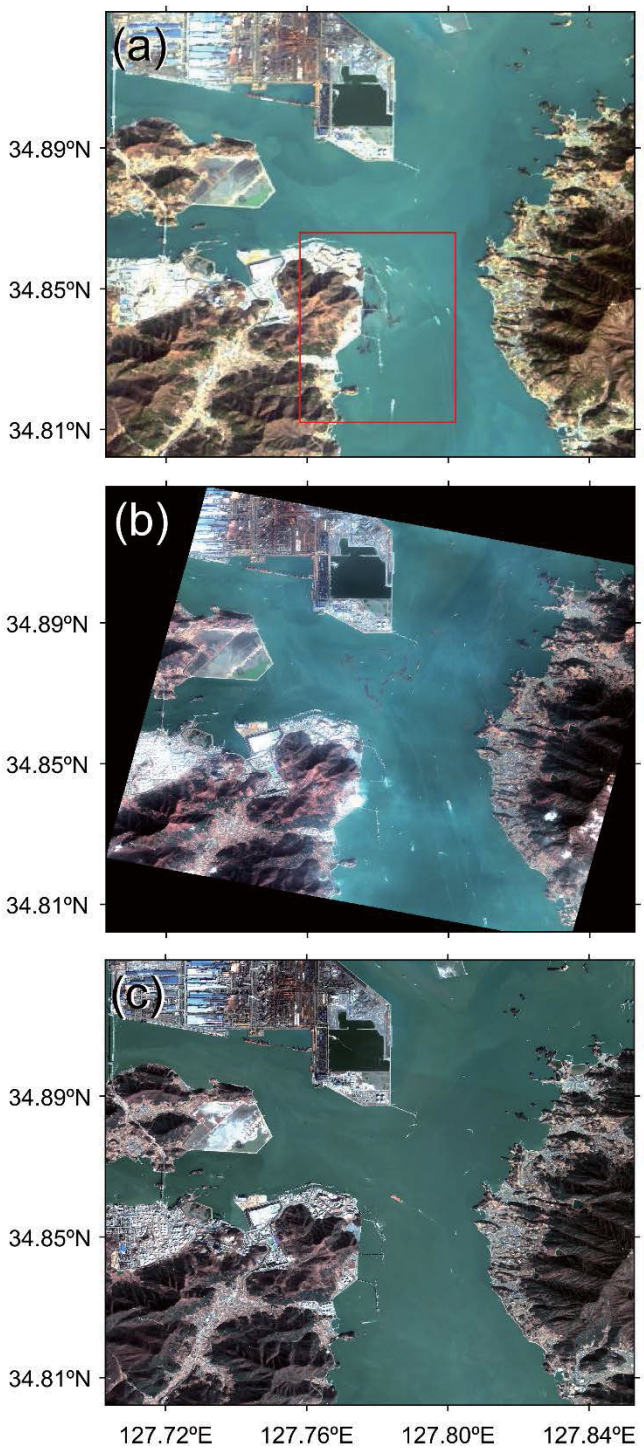

Fig. 2. Satellite RGB images used in this study: (a) Landsat data on January 31, 2014 DubaiSat-2 data on (b) February 2 and (c) February 4, 2014 after the oil spill accident, at a location within the red box in (a).

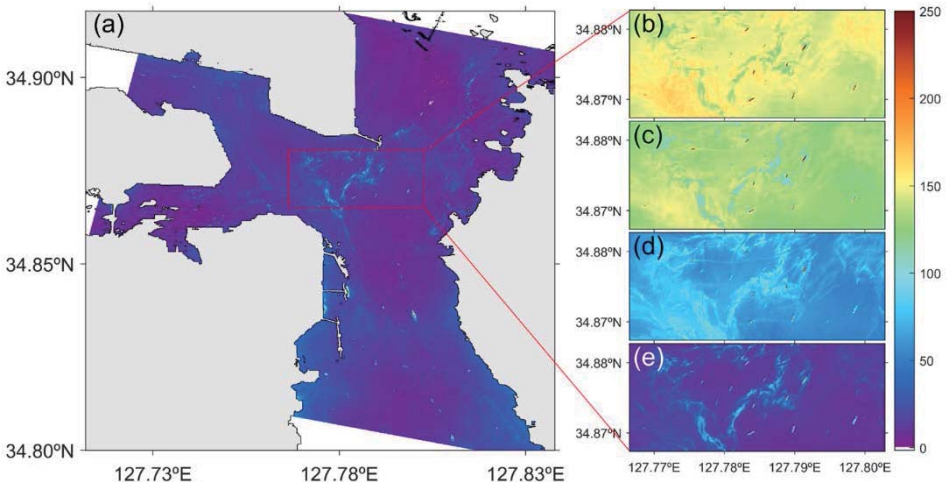

Fig. 3. (a) A satellite image of 832 nm DubaiSat-2 on February 2, 2014 and enlarged images of each band with a central wavelength of (b) 492 nm, (c) 552 nm, (d) 667 nm, and (e) 832 nm.

2.2. Field Observation

2.2.1. Oceanic Optical Measurement

We conducted a field campaign to carry out shipboard observations on February 4, 2014, while DubaiSat-2 was passing over the research area. We made in-situ measurements at 7 stations in the study region over 4 hours. We measured surface reflectances for different types of oil spill using a wide spectrum spectroradiometer, from 350 nm to 1050 nm. We observed two main types of oil spills: thick oil near the source region, and film-like oil both close to and far away from the thick oil. In general, thick oil is thicker than 50 μm and appears dark in the satellite optical images. In contrast, film-like oil looks bright and rainbow colored and is 0.04-50 μm thick (OSPAR, 2012; Macdonald et al., 2015). After several days later, the film-like oil was dispersed widely and appeared as much thinner sheen oil (0.04-0.3 μm) at the southern region far from the source region (Leifer et al., 2012).

2.2.2. Wind Data

As most of the oil spill is spread at or near the sea surface, wind-driven Ekman drift can be one of the major factors responsible for oil movements (Garcia-Pineda et al., 2009; Macdonald et al., 2015). Wind data, including wind direction (°) and wind speed (m/s) at 1-hour intervals, were collected at the meteorological tidal gauge station Yeosu (127.77 °E, 34.75 °N) of Korea Hydrographic and Oceanographic Administration (KHOA) and then used to calculate Ekman surface drift from January 31 to February 4, 2014.

Chapter 3. Methods

3.1. Field Observation

We conducted a field campaign to carry out shipboard observations on February 4, 2014, while DubaiSat-2 was passing over the research area. We made in-situ measurements at 7 stations in the study region over 4 hours. We measured surface reflectances for different types of oil spill using a wide spectrum spectroradiometer, from 350 nm to 1050 nm. We observed two main types of oil spills: thick oil near the source region, and film-like oil both close to and far away from the thick oil. In general, thick oil is thicker than 50 μm and appears dark in the satellite optical images. In contrast, film-like oil looks bright and rainbow colored and is 0.04-50 μm thick (OSPAR, 2012; I. R. Macdonald et al., 2015). After several days later, the film-like oil was dispersed widely and appeared as much thinner sheen oil (0.04-0.3 μm) at the southern region far from the source region (Leifer et al., 2012).

3.2. Conversion of In-Situ Measurements

To compare the in-situ optical measurements with the satellite signal, measured radiances needed to be converted to remote sensing reflectances (R_{rs}), defined as

$$R_{rs} = \frac{L_w}{E_d} = \frac{L_{wT} - (L_{sky} - F_r)}{E_d} \quad (1)$$

where L_w (W/m^2/nm/sr) is the water leaving radiance, E_d (W/m^2/nm) is the down-welling irradiance, L_{wT} (W/m^2/nm/sr) is the total water leaving radiance, L_{sky} (W/m^2/nm/sr) is the sky radiance, and F_r is the Fresnel reflection coefficient at the water surface(Fig. 4). L_w was calculated from measured L_{wT}, L_{sky}, and E_d. These optical data were measured with 1 nm spectral resolution using a spectroradiometer. Measured L_{wT} included skylight reflection effects, therefore it was corrected by measured sky radiance L_{sky} and F_r (Mobley, 1999). Several values of F_r have been suggested by previous studies (Ball, 1954; Austin, 1974), but F_r = 0.025 is an appropriate value for the Korean near shore environment (Ahn, 1990).

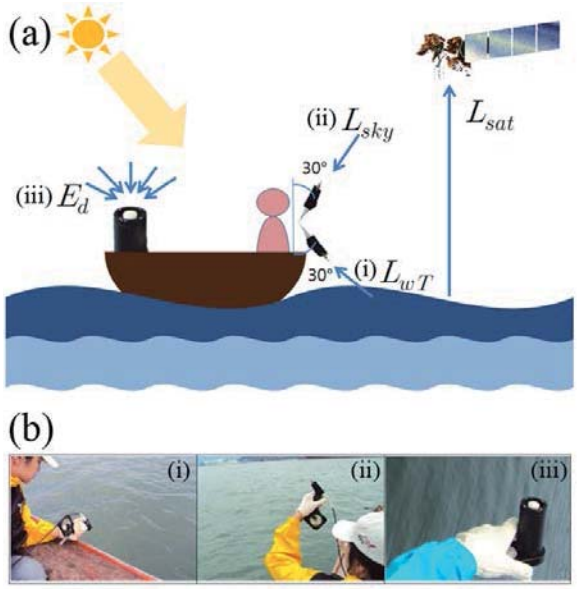

Fig. 4. (a) Schematic diagram of on-board measurement procedures for L_{wT} (total water leaving radiance), L_{sky} (sky radiance), E_d (down-welling irradiance), and L_{sat} (satellite observing radiance), where (i), (ii), and (iii) of (b) are the photos to measure L_{wT}, L_{sky}, and E_d, respectively.

3.3. Neural Network

The Neural Network (NN) method is a computational method, inspired by the human central nervous system, which is capable of pattern recognition (Charalambous, 1992; Møller, 1993). The NN method generally refers to a system of interconnected neurons that can compute values from inputs (Topouzeliz et al., 2007; Garcia-Pineda et al., 2009; Zhang et al., 2011; Leifer et al., 2012; Marghany, 2014; Mera et al., 2014; Zhao et al., 2014; Hu et al., 2015; Macdonald et al., 2015)(Fig. 5). We employ this methodology as a target detection technique, to detect oil spill pixels from satellite images. For this, a neural network was designed with a total of 40 datasets (28 samples in a training data set, 6 samples for validation, and 6 sample points for the testing process), two layers (including a hidden layer and an output layer), and ten neurons in the hidden layer, determined by considering the number of input and output neurons (Heaton, 2008). Details of the input datasets are described as follows.

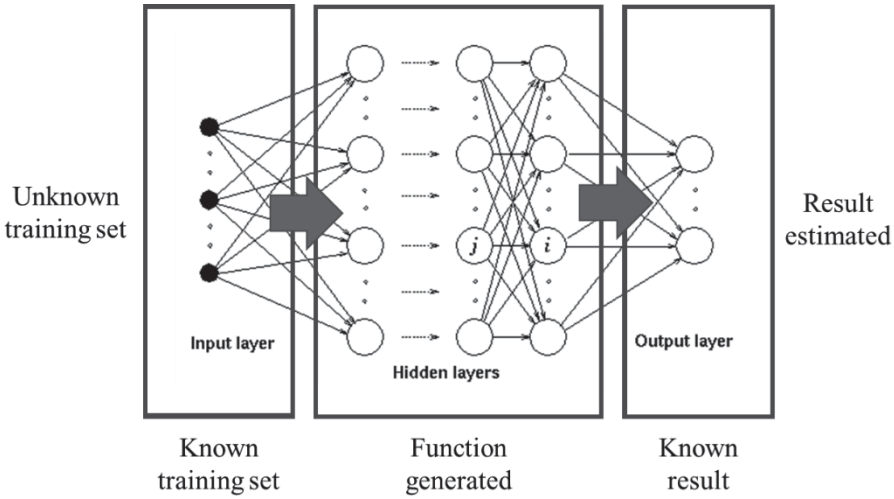

Fig. 5. Schematic diagram of Neural Network method.

3.4. Ship and Ship Shadow Masking

3.4.1 Ship Mask

Many previous studies have attempted to distinguish pixels corresponding to ships from those corresponding to the sea using a variety of methods (Wu et al., 2009; Corbane et al., 2010). Normally, ships have high reflectance values in most channels, as shown in Fig. 3. Subjective visual inspection showed that pixels corresponding to ships had significantly higher reflectances in the 492 nm channel. Thus, we made a ship mask by eliminating from the sequential procedure those ship pixels with digital numbers greater than those in the 492 nm channel (>200).

3.4.2. Ship Shadow Mask

In contrast to satellite images with relatively low spatial resolution, high-resolution satellite data like DubaiSat-2 can observe the spatial structure of the sea surface, including ships, ship wakes, or ship shadows, in great detail. Thus, it is possible to discriminate ship shadow and pier pixels by making mask files in the oil spill detection procedure.

It is noted that the low reflectance values of ship shadows can be confused with those of oil spills. Therefore, pixels corresponding to ship shadows needed to be eliminated by producing a shadow mask file. To mask the shadow, we considered the height of the ship and pier and also sun elevation and azimuthal angle. Additionally, smoke from factories near the research area and ship wakes were eliminated by removing high reflectances in visible channels. In the case of optical images, techniques for the masking of clouds and cloud shadows are well developed and can be easily employed. However, no methods to detect and eliminate pixels with cloud shadows were needed in this study, because all of the satellite images used for analysis were captured under clear sky conditions.

First of all, we collected all available image data including target and non-flagged pixel values. For oil spill detection, we used 16 types of data as inputs to the NN model, i.e. the R_{rs} of the four spectral channels, 5×5 window sized means (m), standard deviations (std), and the standard deviation normalized to the mean over mean (std/m),

for each channel value (Fig. 4). Using the detection results, we estimated the areal extent of the oil spill. As illustrated by the spatial distribution of oil in Fig. 2, oil thickness can vary depending on the degree of dispersion. Therefore, we classified oil types by developing a recursive neural network system consisting of three separate stages: thick oil, film-like oil, and sheen. The pixels identified as thick oil in the first stage were excluded from the input for the second step, which detected film-like oil. The initially classified oil pixels were removed from the oil spill, and then the secondly classified pixels were classed as thinner oil pixels through a recursive searching procedure. Using this type of methodology, we finally categorized the oil spill into four classes: thick oil, film-like oil, sheen, and non-oil, and the areal extents of each type were estimated separately. This procedure is illustrated in the flow chart in Fig. 4.

3.5. Particle Tracking

Thick oil spills tend to disperse over time, by being modified into other types of film-like oil or sheen oils that are distributed across the entire region. To investigate the spatial coverage of the spilled oils, we traced the oils using a tracking method based on a numerical tide model and the calculation of Ekman drift, as follows.

3.5.1. Numerical Tide Model

The numerical tidal model 'Environmental Fluid Dynamics Code (EFDC)' was used to estimate the movement of seawater around the time of the accident. This model, developed by the Virginia Institute of Marine Science has been used in many studies to simulate seawater movement and three dimensional particle transport in coastal areas like the study region, as well as estuaries and wet-lands (Hamrick, 1992). As input bathymetry data for the model, we used both KHOA data and our own data based on intensive field measurements investigating bathymetry complexity throughout the study region.

To validate the tidal model results, we compared tidal elevation and currents with in-situ measurements and 1-h interval tidal gauge data of sea surface elevation at Yeosu (127.77° E, 34.75° N) and Gwangyang (127.75° E, 34.90° N) from January 28 to February 28,

2014 (KHOA). There was a strong correlation between tidal elevation measurements, with Root Mean Square Errors (RMSE) of approximately 0.2% (M_2), 0.9% (S_2), 1.5% (K_1), and 1.4% (O_1), and bias errors of approximately −0.2 cm, 0.5 cm, 0.2 cm, and 0.2 cm, for each of the four tidal constituents. The phase errors in the four tidal constituents ranged from −0.1° to 0.0°. Tidal currents from the model showed good agreement with in−situ measurements (127.47° E, 34.51° N), with RMSE of 2.6 – 33.3 % and bias errors of −2.2 – 0.1 cm/s from 4 September 2005 to 10 May 2005.

3.5.2. Ekman Drift Surface Current

We assumed that wind-driven currents play an important role in oil spill movement and therefore calculated the Ekman drift surface current using wind data from the Yeosu tidal gauge station. The following equation, from (Mao and Heron, 2008) was used:

$$U_E = \frac{\rho_a C_D U_{10}^2}{\rho_w \sqrt{f A_z}} \quad (2)$$

where ρ_a and ρ_w are the density of air and seawater respectively, C_D is the drag coefficient as a function of wind speed, f is the Coriolis parameter, A_z is the vertical eddy viscosity, and U_{10} is the wind speed at a height of 10 m (Anderson, 1993; Park et al., 2006). The direction of the Ekman drift is tilted 15° rightward of the wind direction, as suggested by (Mao and Heron, 2008). As the wind data from KHOA buoy was measured at a height of about 1.2 m, it first needed to be converted into 10 m height winds using the Liu, Katsaros, and Businger model (Liu et al., 1979).

3.5.3. Oil Spill Trajectory

Oil spill movements derived from satellite data were compared to tracking results retrieved by the General National Oceanic and Atmospheric Administration Operational Modeling Environment of National Oceanic and Atmospheric Administration (Cheng et al., 2014; Xu et al., 2015). The model results, based on the Lagrangian tracking method, included both the effects of oceanic tides as well as wind fields. Some of the models, for example Seatrack Web, produced a trajectory of spilled oil using satellite-tracked surface drifter data (Price et al., 2006; Kostianoy et al., 2005). Since the Korean coastal region not only has strong tides and tidal currents but also a dominant monsoon system, we utilized the tidal current vectors from numerical tide models and wind vectors to track oil particles from the source region of the oil spill. To trace the oil spill, we incorporated the effect of tidal currents and Ekman drift to understand the movements estimated by satellite images. Under the assumption that the random displacements of oil particles and the small diffusivity of oil can be ignored (Hamam, 1987), we estimated the geolocation of each displaced oil particle at a given time step by multiplying the current speed by the time interval for each zonal and meridional direction. The initial point from which to trace the oil was chosen from the pixels assigned as oil pixels in the Landsat image from 31 January 2014.

Chapter 4. Result

4.1. Removal of Ship and Ship Shadow Pixels

As shown in Fig. 3, there were several ships and vessels present to monitor the oil spill and conduct clean-up operations. Pixels corresponding to the ships appear white due to predominantly high reflectances. In addition to the higher brightness, ships tend to cast a shadow because of the oblique solar insolation. As the size and height of the ship increases, so does the areal extent of the shadow. Ships and their corresponding shadows can be obstacles to oil detection, particularly because the shadow has similar characteristics to the oil pixels. Thus, we eliminated both ship pixels and their shadow pixels by adopting the objective method as described in the previous section. Fig. 6 shows flags of the subsampled region, where green, yellow, and red colors indicate land, ships, and shadows, respectively. Flagged pixels were not included in the calculation to determine whether a pixel is oil or non-oil. When compared to the RGB image (Fig. 6c), small and dim objects appear in high resolution in the flagged pixel image (Fig. 6b).

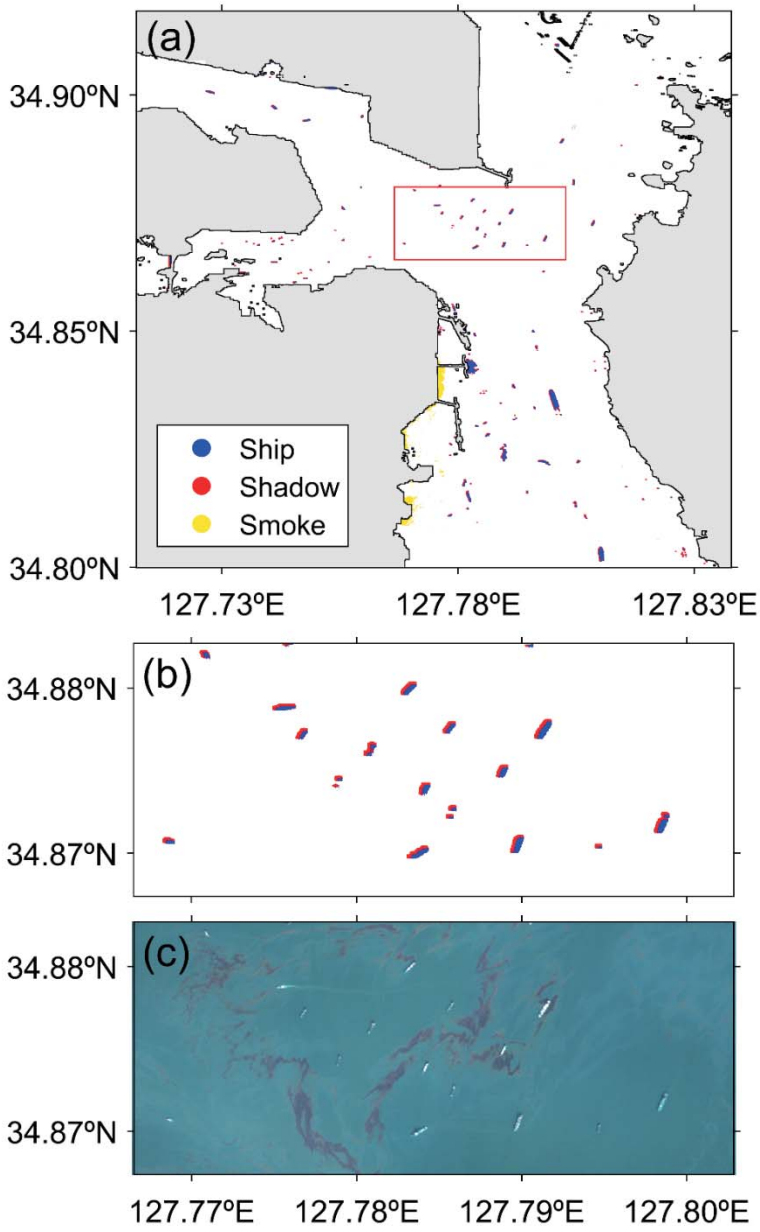

Fig. 6. (a) An example of a DubaiSat-2 image (February 2, 2014) classification for 3 pixel types: ship (blue), ship shadows (red), and smoke (yellow), (b) a subset image of the classification results, and (c) RGB image of the area shown by the red box in (a).

4.2. Spectral Characteristics of Oil

To determine the spectral characteristics of oil spilled on the sea surface, we conducted field observations with a spectroradiometer (350–1050 nm) on February 4, 2014. From this we obtained spectral R_{rs} of oil and non−oil, indicated by solid and dashed lines, respectively, in Fig. 7. Dotted lines show the response functions of DubaiSat−2 bands. At wavelengths of 350–500 nm, oil and non−oil have similar values and R_{rs} patterns. However, R_{rs} of oil are approximately 2–6 times higher than those of non−oil in the 500–930 nm range, as demonstrated by the peaks at 580, 690, and 810 nm (Fig. 7a). As these peaks are located near the centered wavelength of satellite channels, we conclude that oil detection is possible using satellite images.

Since both the patterns and spectral characteristics of oil and non−oil pixels appear to be similar, reflectances seem to be a robust discriminator in oil classification. Considering this, we amplified the signal by deriving a ratio of the reflectances of oil to the reflectances of the non−oil sea surface (Fig. 7b). Although the measured spectral characteristics of the oil spills were used as the input data for our neural network method for oil detection, the ratio of reflectances showed clear spectral peaks and different responses at longer wavelengths, from 700 to 800 nm, so the ratios were added to the input field of the NN model.

The variation in oil characteristics at different wavelengths is in

agreement with the spatial distribution and distinction shown in Fig. 3. It is relatively easy to recognize thick oil from the RGB image due to its darker color compared to film-like oil. In contrast, the fact that film-like oil appears only slightly brighter than non-oil seawater and spreads over a wide area makes it difficult to discriminate between the two. Relative spectral characteristics of film-like oil are also similar to non-oil seawater, although absolute values of film-like oil are higher than those of non-oil.

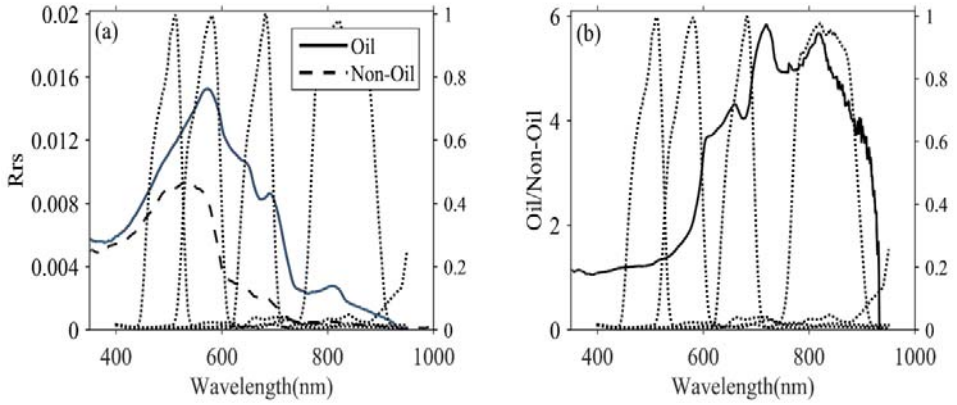

Fig. 7. (a) In-situ measurements of spectral remote sensing reflectances, as a function of wavelength (nm), for oil (solid) and non-oil (dashed) pixels and (b) variations in the ratio of reflectances of oil to non-oil pixels, as a function of wavelength, where the dotted lines in (a) and (b) represent the spectral response functions of the DubaiSat-2 sensor.

4.3. Ship and Ship Shadow Masking

Many previous studies have attempted to distinguish pixels corresponding to ships from those corresponding to the sea using a variety of methods (Wu et al., 2009; Corbane et al., 2010). Normally, ships have high reflectance values in most channels, as shown in Fig. 7. Subjective visual inspection showed that pixels corresponding to ships had significantly higher reflectances in the 492 nm channel. Thus, we made a ship mask by eliminating from the sequential procedure those ship pixels with digital numbers greater than those in the 492 nm channel (>200).

In contrast to satellite images with relatively low spatial resolution, high-resolution satellite data like DubaiSat-2 can observe the spatial structure of the sea surface, including ships, ship wakes, or ship shadows, in great detail. Thus, it is possible to discriminate ship shadow and pier pixels by making mask files in the oil spill detection procedure.

It is noted that the low reflectance values of ship shadows can be confused with those of oil spills. Therefore, pixels corresponding to ship shadows needed to be eliminated by producing a shadow mask file. To mask the shadow, we considered the height of the ship and pier and also sun elevation and azimuthal angle. Additionally, smoke from factories near the research area and ship wakes were eliminated by removing high reflectances in visible channels. In the case of optical images, techniques for the masking of clouds and cloud

shadows are well developed and can be easily employed. However, no methods to detect and eliminate pixels with cloud shadows were needed in this study, because all of the satellite images used for analysis were captured under clear sky conditions.

First of all, we collected all available image data including target and non-flagged pixel values. For oil spill detection, we used 16 types of data as inputs to the NN model, i.e. the R_{rs} of the four spectral channels, 5×5 window sized means (m), standard deviations (std), and the standard deviation normalized to the mean over mean (std/m), for each channel value (Fig. 3). Using the detection results, we estimated the areal extent of the oil spill. As illustrated by the spatial distribution of oil in Fig. 6, oil thickness can vary depending on the degree of dispersion. Therefore, we classified oil types by developing a recursive neural network system consisting of three separate stages: thick oil, film-like oil, and sheen. The pixels identified as thick oil in the first stage were excluded from the input for the second step, which detected film-like oil. The initially classified oil pixels were removed from the oil spill, and then the secondly classified pixels were classed as thinner oil pixels through a recursive searching procedure. Using this type of methodology, we finally categorized the oil spill into four classes: thick oil, film-like oil, sheen, and non-oil, and the areal extents of each type were estimated separately. This procedure is illustrated in the flow chart in Fig. 8.

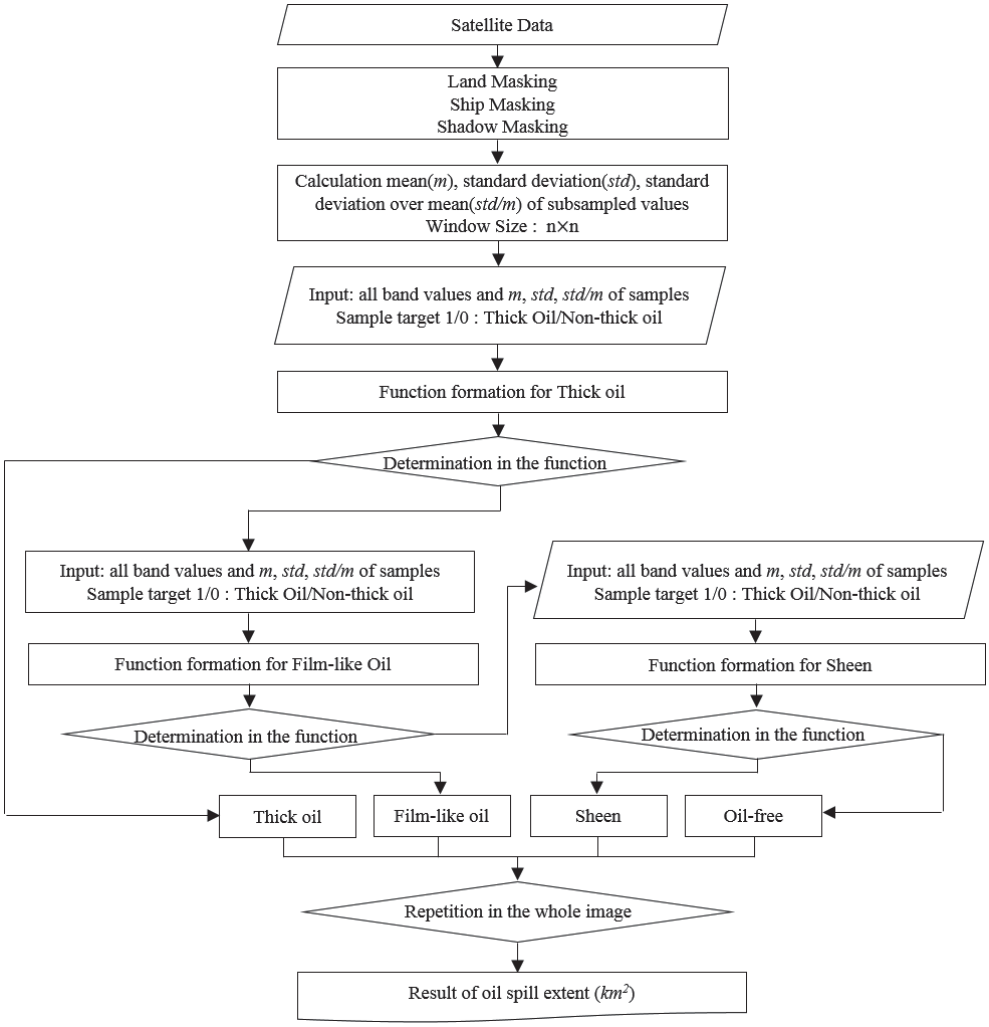

Fig. 8. Flow chart of the oil spill detection procedure using satellite images.

4.4. Image Classification into Thick oil/Film-like oil

The recursive NN method resulted in classification of the oil into thick oil (red) and film-like oil (green), shown in Fig. 9. Red regions in Fig. 9a indicate the oil distribution on the first day of the oil spill, observed by Landsat OLI about two hours after the event, which shows that the oil was mainly located near the oil pipeline and had not yet spread far from the site of the accident. The areal extent of thick oil on the day was 0.22 km^2, corresponding to 0.29% of the total area of the study region. On February 2, the thick oil in Fig. 9b, marked in red, had dispersed several kilometers away from the pipeline and occupied an area of approximately 1.60 km^2 (2.11%). Since there was continual leakage of oil into the sea, the extent of oil had increased from that of the first day. On February 4, the oil seemed to disappear across the entire region. However, small amounts were found near the coast, as shown in the enlarged southeastern part of the study region, which clearly indicates oil pixels with an area extent of 0.20 km^2 (0.27%), illustrated by the red dots in Fig. 9g. The estimated areal extent of thick oil from satellite images from the three days is presented in Table 2.

As Fig. 6c shows, another type of oil was found around the thick oil as a thin film. Green regions in Figs. 9b, d, and f indicate these film-like oils, estimated by the recursive NN method. It is noted that the areal extent on the first day was approximately eight times larger than that of the thick oil on the same day, i.e. 1.77 km^2, corresponding

to 2.33% of the total area of the study region. The most interesting feature is that the film-like oil was dispersed throughout the majority of the study region, particularly in the western part of the bay, as well as the southern region. The areal extent was a large as 20.10 km^2 (26.54%), covering almost the entire research area by February 2 (Fig. 9e). The sheen oil type quickly disappeared, and had only a small areal extent of 0.76 km^2 (1.01%) in the DubaiSat-2 image on February 4, 2014. The extent of the film-like oil in the second image and the sheen oil type in the third satellite image are shown in Table 2.

Table 2. Extent of thick oil and film-like oil, estimated from satellite images, by area (km^2) and by percentage of the study area (%).

Satellite Time	Extent of oil spill (km^2)		
	Thick oil	Film-like oil	Total
Landsat OLI 31 January 2014 02:06 UT	0.2221 (0.29%)	1.7677 (2.33%)	1.9898 (2.63%)
DubaiSat-2 2 February 2014 02:22 UT	1.5957 (2.11 %)	20.1039 (26.54 %)	21.6996 (28.65%)
DubaiSat-2 4 February 2014 02:40 UT	0.2034 (0.27%)	0.7628 (1.01%)	0.9662 (1.28%)

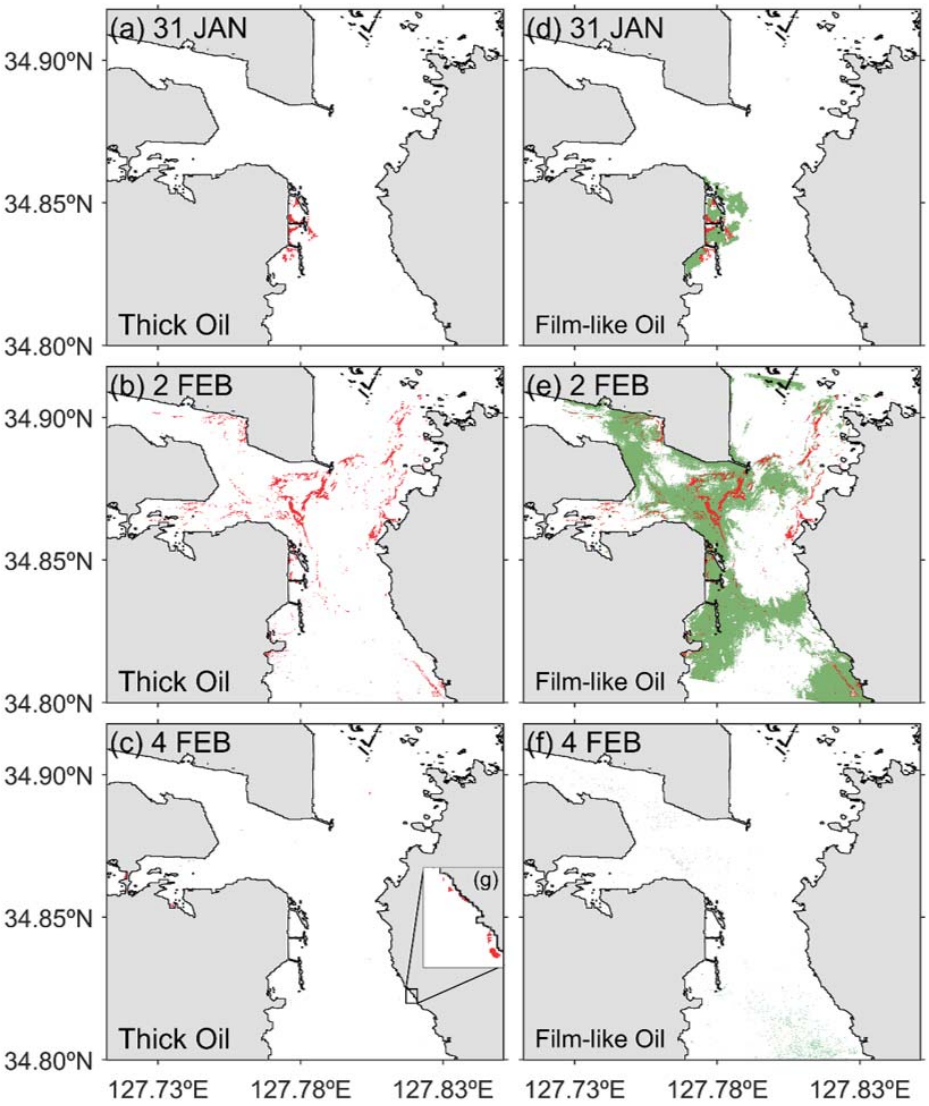

Fig. 9 Results of image classification into thick oil (red) and film-like oil (green) from January 31, 2014 to February 4, 2014, where (g) is the enlarged portion shown in (e).

4.5. Tidal Effects on Oil Spill Dispersion

There are strong tidal currents in the study region near the site of the oil spill. As a result, we investigated the magnitude and direction of these tidal currents. On 31 January 2014, the maximum tidal current velocity gradually declined from 0.6 m/s to 0.4 m/s. Most of the tidal currents were directed southward or northward (Fig. 10a and c). The velocity of tidal currents ranged from 0.01 to 0.65 m/s, as shown by the histograms in Fig. 10b.

Fig. 11 shows the tidal current maps at the times when the satellite images were taken, from 31 January to 4 February 2014. During the initial stages after the oil spill, most of the tidal currents were directed to the south but were then gradually deflected to the north. The predominant tidal constituents of this region are M_2 and S_2, so the tidal ellipse has almost a half-day period, as shown in Fig. 11d. The major axis of the ellipse is aligned in the north-south direction, in accordance with the geological characteristics of the research area (Fig. 11d). Thus, it is anticipated that the spilled oil should have followed the tidal currents, as long as other atmospheric or oceanic forcings were not as strong as the tidal effect.

As can be seen in the oil spill images in Fig. 9, the oil slick moved with time. To explain the mechanisms of this movement, we performed numerical tidal modeling from 31 January 13 to February 4, 2014, with 10-minute time intervals and an applied

tidal current velocity at the source of the spill. We then calculated changes in the locations of particles that correspond to oil pixels during those four days.

Fig. 12 shows a time series of the spatial distribution of oil particles every 12 hours, simulated using a numerical model including tidal currents. The initial location of the oil spill is denoted by the green dot in Fig. 12a. Fig. 12b highlights the oil spill dispersion estimated from the Landsat data about two hours after the accident on 31 January. The series of simulation results shown in Figs. 12c–j shows that the oil particles generally fluctuated between moving to the north and to the south. Areas with a high intensity of oil pixels were oriented in a north–south direction during the initial stages and then became dispersed over the entire bay, as shown by the bright red colors in Fig. 12. Fig. 12f illustrates the particle distribution at the time when the second satellite image was taken. Oil dispersion at that time appears very similar to the oil slick pattern estimated by the NN method in Fig. 9b. The time of Fig. 12j corresponds to the time of the satellite image in Fig. 9g. This pattern, however, is quite different between the two figures, indicating significant differences between the results from satellite images and those from the numerical simulation. One of the reasons for this may be that the forcing data in the simulation consisted of tidal information only. Thus, in the following section we investigate other atmospheric effects by considering the role of winds during the oil spill event as well as the period covering all the satellite

images.

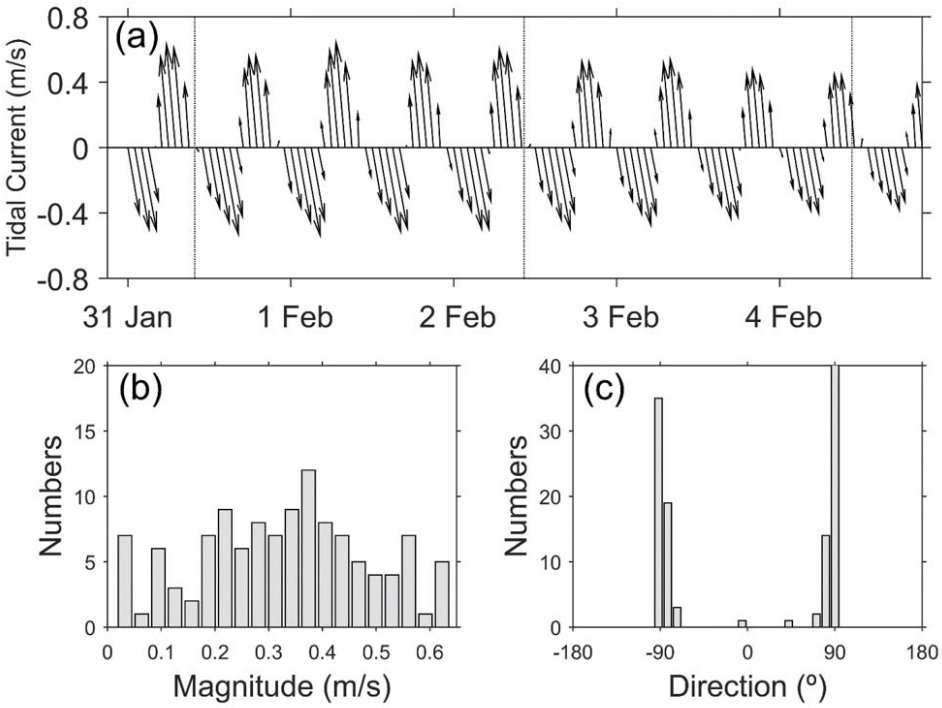

Fig. 10. (a) Hourly variations in tidal current vectors (m/s) at the accident location from January 31 to February 4, 2014, where the dotted lines represent the acquisition time of each satellite image, histograms showing number density of (b) tidal current.

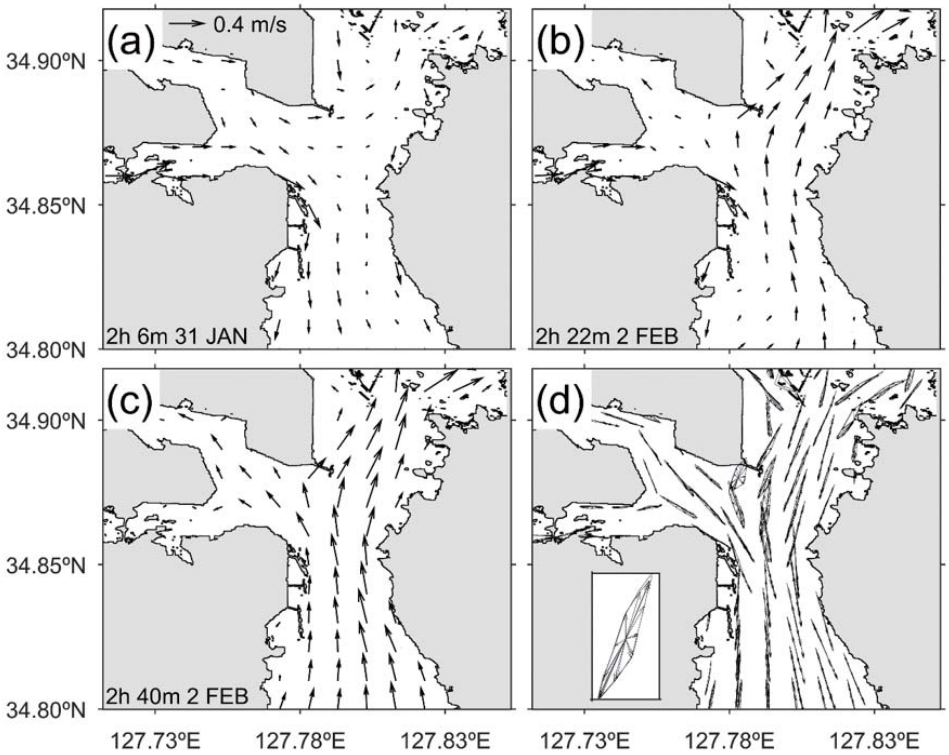

Fig. 11. Spatial distribution of tidal current vectors of 4 major tidal components ((M_2, S_2, K_1, O_1) at (a) 2h 6m on January 31, 2014 (UT), (b) 2h 22m on February 2, 2014, (c) 2h 40m on February 4, 2014, and (d) tidal ellipses, where the enlarged portion shows the rotating tidal current vectors forming the tidal ellipse.

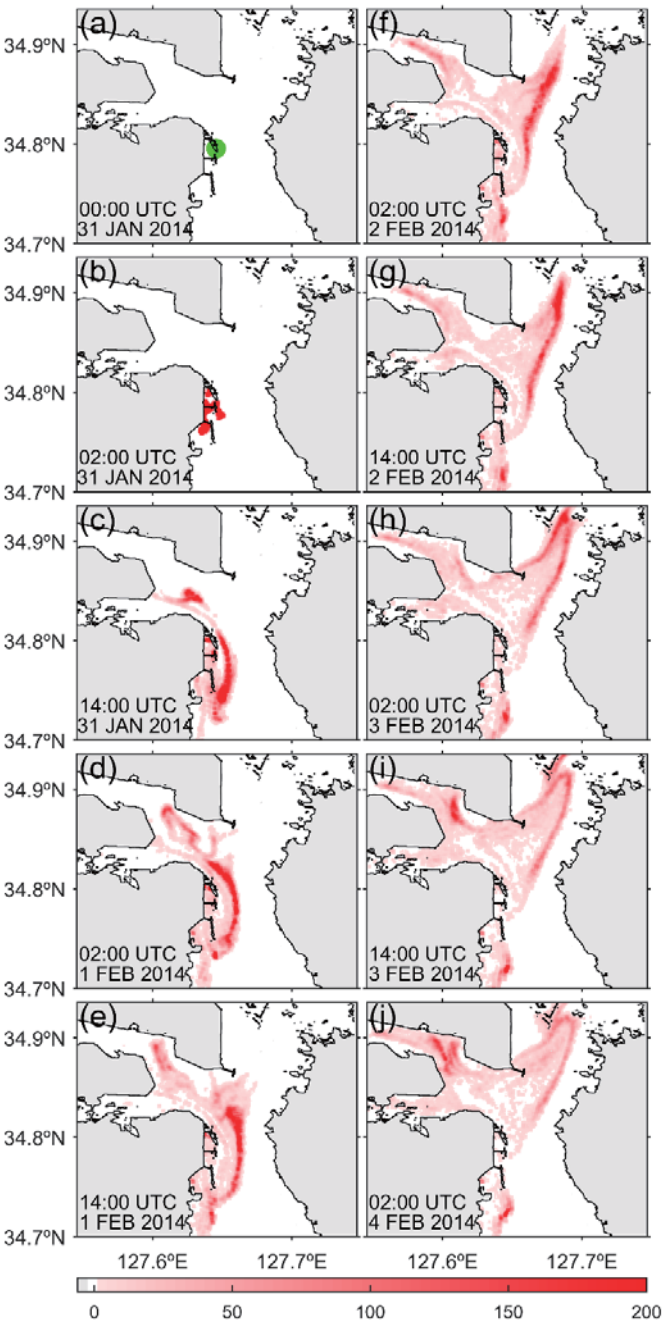

Fig. 12. (a) Location of the oil pipeline (green dot) at 9h 30m on January 31, 2014, (b) detected oil pixels from the first satellite image of Landsat, and the temporal dispersion of the oil spill from tidal model simulations run every 12 hours, (c) to (j), for the period of January 31 to February 4, 2014. The variation in red color is an estimate of oil-pixel numbers within a 3×3 window.

4.6. Effect of Wind on Oil Spill Dispersion

To determine the effect of wind on oil movement, we calculated the Ekman drift using equation (2). Fig. 13a presents the time series of wind vectors at the buoy station from January 31 to February 2. There was a characteristic variation in the wind field, which was very weak at first, with a magnitude of less than 3 m/s. Afterwards, it increased in speed to 3–8 m/s and changed direction to the north. The Ekman surface drift current corresponding to these wind speeds shows very small values of about 0.01 m/s for the first three days after the accident. However, it abruptly intensified to 0.1 m/s, directed to the south, as inferred from wind directions in Fig. 13b.

Discrepancies in oil spill dispersion between simulated and satellite–observed results imply that other effects should be considered to explain the southeastward movement of oil, as previously described. We traced the dispersion of oil from the model results, this time forced by both tides and wind, as shown in Fig. 14. During the first two days, when the wind speed was low, oil particle distributions did not change significantly, as indicated from Fig. 14a to Fig. 14h. However, from February 3, when the wind speed began to increase to approximately 7 m/s, oil particles moved southward, following the direction of the Ekman drift (Fig. 14). To highlight the differences in spatial dispersion, we plotted the distribution of oil particles produced by the two model simulations in Fig. 13c. When taking into account the wind field, oil particles were dispersed to the

south, as denoted by the red dots in Fig. 13c. This is evidence for the significant role of the Ekman drift. Temporal variations in the ratio of Ekman drift to tidal current speed (Fig. 13d) are very small, less than 0.1 for the first two days, however, they reached a peak of about 1.3 from February 3, 2014, when ratios were much higher than those during the initial period.

The dispersion of oil particles is dependent not on linear processes but on non-linear processes. Oil trajectories can be affected by the initial locations of particles near the collision point that produced the oil spill. Considering this, we selected three representative locations, marked in Fig. 15a as 'A', 'B', and 'C', to examine the different possible dispersions. From location 'A', particles mainly travelled southward initially and then northward, oscillating repeatedly between the two directions. They then gradually moved southeastward, following the deep channel of the bay. Although the tidal currents are fundamentally returning currents, the particles never returned to the inner bay and instead continued to travel far from the oil spill site. From the second location, 'B', located inside the pier, particles travelled to the south and to the north, but mainly dispersed eastward with time, eventually reaching the eastern coast. The third origin of drifting particles, located at the northernmost position 'C', revealed a considerably different pattern from the other two locations. Primarily, the tracer particles moved to the north and gradually occupied both the northwestern and northeastern channels of the bay.

According to simulations of this type, the particle trajectories depend on where the oil was initially spilled. This suggests that oil particles can be scattered over a much wider area in this region, regardless of the dominant shape of the tidal ellipse. In addition, the scattered patterns provide evidence for the substantial role that local wind vectors play on the spatial dispersion of oil.

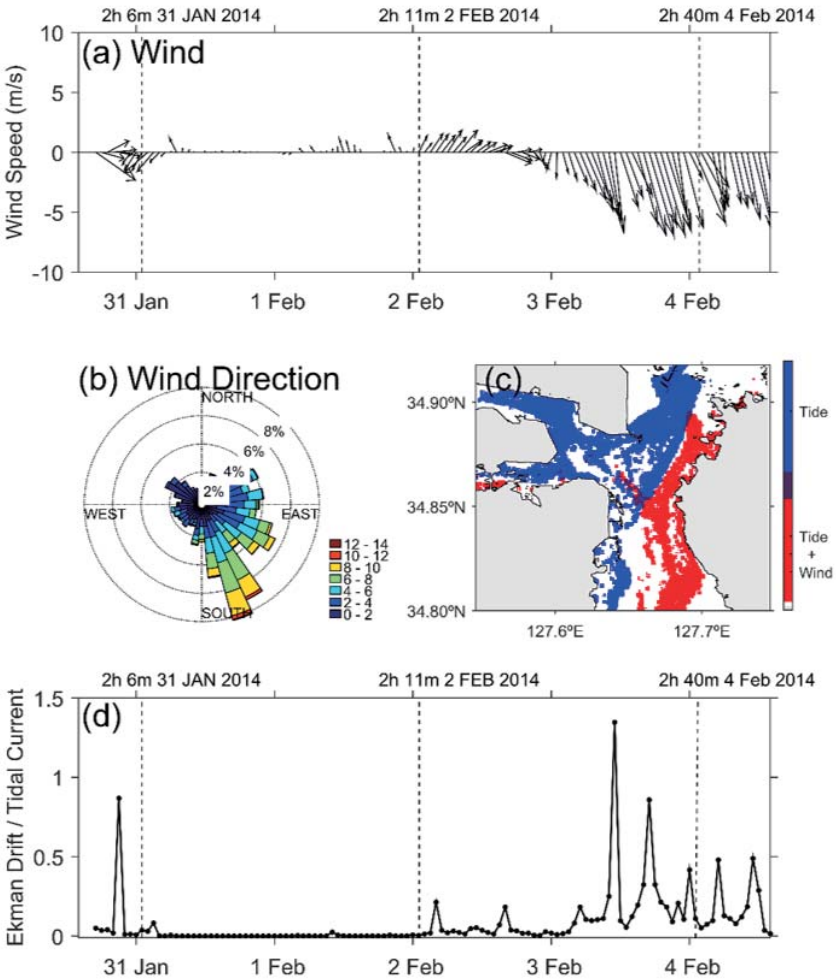

Fig. 13. (a) Time series of wind vectors at a tidal gauge station (127.77 °E, 34.75 °N), where dotted lines indicate the times of three satellite images, (b) histogram of wind directions, (c) spatial distribution of oil tracers from numerical experiments using tide data only (blue) and both tide and wind field data (red), and (d) time series of the ratio of Ekman drift to tidal current speed.

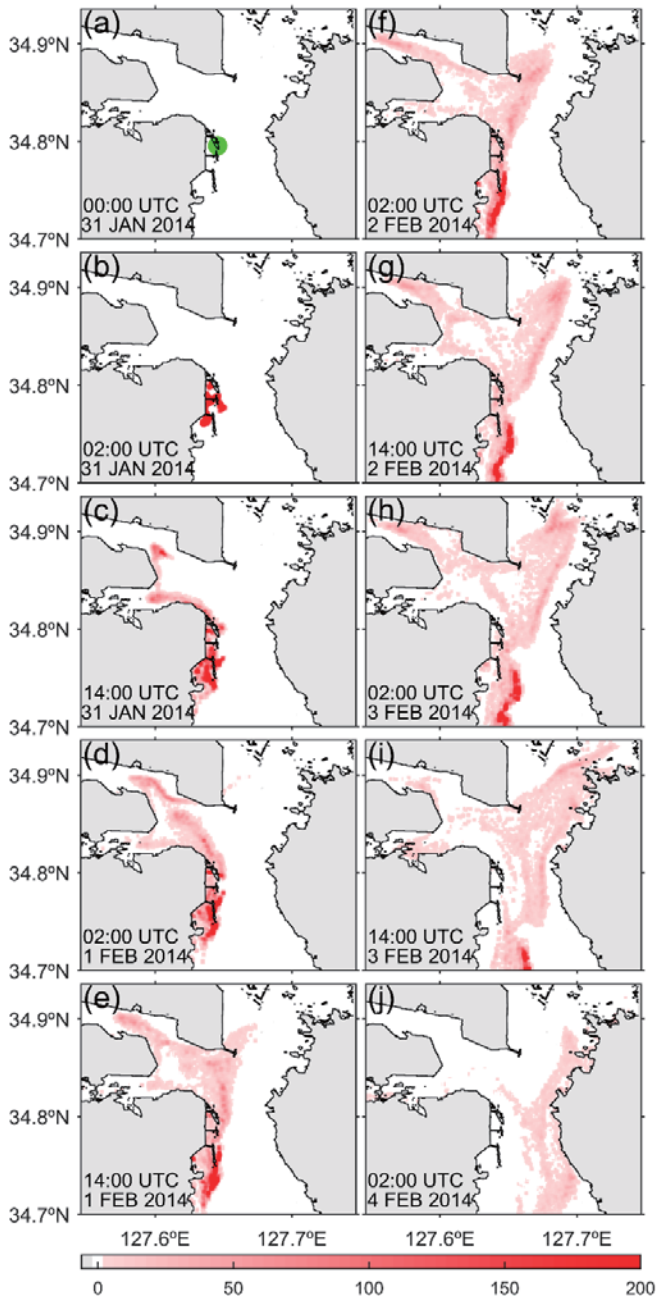

Fig. 14. (a) Location of the oil pipeline (green dot) at 9h 30m on January 31, 2014, (b) detected oil pixels from the first satellite image of Landsat, and the temporal dispersion of the oil spill from a tide model simulations, including wind stress, run every 12 hours, (c) to (j), for the period of January 31 to February 4, 2014. The variation in red color is an estimate of oil-pixel numbers within a 3×3 window.

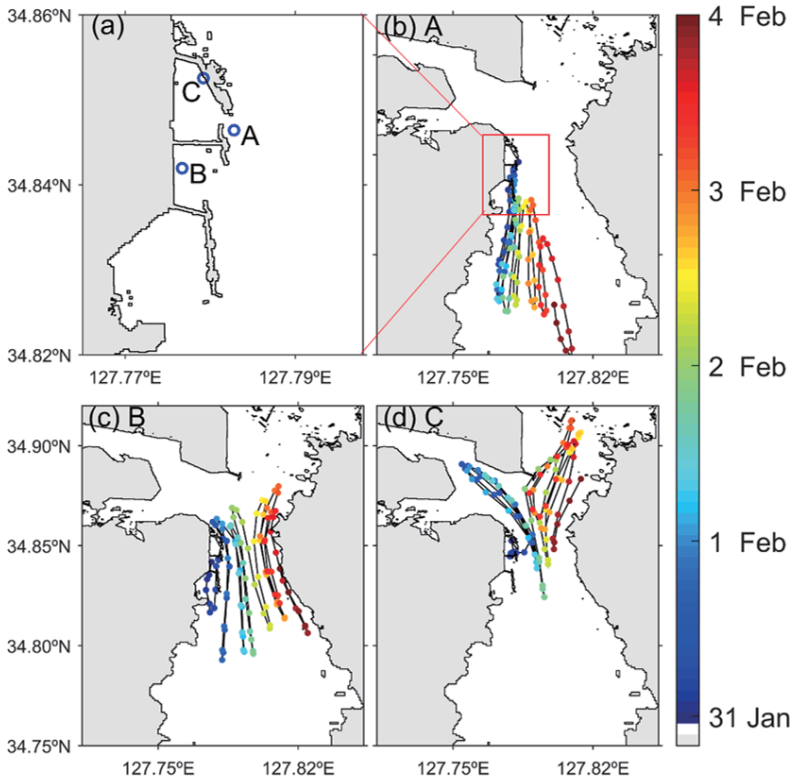

Fig. 15. (a) Initial locations of three oil spill tracers and the temporal evolution of oil spills from (b) point A, (c) point B, and (d) point C, from numerical experiments including the effects of tide and wind field changes. The colors represent time, in hour intervals, from January 31 to February 4, 2014.

Chapter 5. Summary and Conclusion

In this study, we developed a methodology to detect the temporal evolution of oil spills using DubaiSat-2 and Landsat OLI data with high spatial resolution. The oil was classified into relatively thick oil or film-like oil by developing a recursive NN method. This method reveals significant differences in the areal extent of spilled oil in the bay, contrary to the non-recursive method. Film-like oil was dispersed far from the collision site and occupied the majority of the bay, which could not be seen using the traditional NN method.

Satellite-based oil spill features were compared to numerical simulation results for two cases: using only tides and using both tides and wind as forcing data for the model. Distributions of oil pixels detected by the NN method were similar to particle locations controlled by tidal currents when winds were relatively weak. However, when wind speeds were strong enough to spread the oil, it was dispersed over significantly wider regions, regardless of the main flow direction of the tidal currents. In light of this, we suggest that the ratio of expected wind-driven Ekman current to tidal current speed can be a useful indicator of the extent to which oil spills are dispersed by wind vectors. If the ratio is small, it is feasible to only include the role of tidal currents in predictions of oil spill dispersal. Otherwise, the dispersion extent of the oil should only be inferred from a model simulation that incorporates both wind and tidal currents.

Obtaining satellite optical images of oil spills has long been problematic because of cloud-contaminated or cloudy pixels under diverse atmospheric conditions. This limitation has driven many oil detection studies to use all-weather-effective active microwave remote sensing data such as SAR data. However, SAR observations are less frequently obtained from coastal regions, compared with land observations. Thus, the restriction of the limited SAR observation opportunities has prevented the active utilization of SAR images for oil detection studies in this particular coastal region. In view of this, many multi-spectral and multi-satellite images should be used in combination to investigate and monitor the temporal evolution of oil spills.

This study employed optimal imagery, and so would have faced difficulties in detecting meter-scale small oil slicks near the coast, especially when using satellite images with low spatial resolution. Another significant problem facing oil spill detection from optical images is derived from the presence of shadows from obstructions. Such shadows tend to have a spectral reflectance similar to that of dark thick oil, and so the inclusion of pixels containing the reflectance of the shadow of a ship or other artificial construction may represent another source of error when using optical images.

This study developed a detection method that was based on optical images rather than SAR images, and investigated the main causes of the temporal dispersion of both thick oil and thin, film-like oil. The neural network method presented here is expected to be

applicable to most optical image data with RGB channels, enabling the detection of oil spills and their classification into thick oil and film-like oils. This study emphasized that both thick and film-like oil spills could be more effectively detected from optical satellite images if the satellite had an additional sensor at near-IR wavelengths, specifically with a central wavelength of around 865 nm; this was supported by our intensive in-situ measurements during the oil spill event. We provide a methodology for discriminating between non-oil and oil pixels in optical imagery, and for further classifying them into a number of types, from thick to very thin sheen pixels. In light of this, this study is relevant to the detection and analysis of the evolution of different oil types in local seas as well as on a global oceanic scale.

References

Ahn, Y.-H., 1990. Optical properties of biogenous and mineral particles present in the ocean. Application: Inversion of reflectance. Ph.D. dissertation, Paris-VI University.

Alpers, W., 2002. Remote sensing of oil spills. *In Proceedings of Maritime Disaster Management*, 57-68.

Anderson, R.J., 1993. A study of wind stress and heat flux over the open ocean by the inertial-disipation method. *Journal of Physical Oceanography*, 23(10), 2153-2161.

Austin, R., 1974. The remote sensing of spectral radiance from below the ocean surface. *Optical Aspects of Oceanography*, 317-344.

Ball, F., 1954. Sea surface temperatures. *Australian Journal of physics*, 7, 649-652.

Barni, M., Betti, M., and Mecocci, A., 1995. A fuzzy approach to oil spill detection an SAR images. *In Proceedings of International Geoscience Remote Sensing Symposium, Quantitative Remote Sensing for Science and Application,* 157-159. doi: 10.1109/IGARSS.1995.519676.

Barron, M.G., 2012. Ecological impacts of the Deepwater Horizon oil spill: implications for immunotoxicity. *Toxicologic Pathology*, 40(2), 315-320.

Bern, T.-I., Wahl, T., Andersen, T., and Olsen, R., 1993. Oil spill detection using satellite based SAR-experience from a field

experiment. *Photogrammetric Engineering and Remote Sensing,* 59(3).

Bragg, J.R., Prince, R.C., Harner, E.J., and Atlas, R.M., 1994. Effectiveness of bioremediation for the Exxon Valdez oil spill. *Nature*, 368(6470), 413-418.

Brekke, C., and Solberg, A.H.S., 2005. Oil spill detection by satellite remote sensing. *Remote Sensing of Environment*, 95(1), 1-13.

Bulgarelli, B., and Djavidnia, S., 2012. On MODIS retrieval of oil spill spectral properties in the marine environment. *IEEE Geoscience and Remote Sensing Letters,* 9(3), 398-402.

Camilli, R., Reddy, C.M., Yoerger, D.R., Van Mooy, B.A.S., Jakuba, M.V., Kinsey, J.C., McIntyre, C.P., Sylva, S.P., and Maloney, J.V., 2010. Tracking hydrocarbon plume transport and biodegradation at Deepwater Horizon. *Science*, 330(6001), 201-204.

Carpenter, A., 2007. The Bonn Agreement aerial surveillance programme: Trends in North Sea oil pollution 1986-2004. *Marine pollution bulletin*, 54(2), 149-163.

Charalambous, C., 1992. Conjugate gradient algorithm for efficient training of artificial neural networks. *In Proceedings of IEEE Circuits, Devices and Systems*, 139(3), 301-310. doi: 10.1049/ip-g-2.1992.0050.

Cheng, Y., Liu, B., Li, X., Nunziata, F., Xu, Q., Ding, X., Migliaccio, M., and Pichel, W.G., 2014. Monitoring of oil spill trajectories with COSMO-SkyMed X-Band SAR images and model simulation. *IEEE Journal of Selected Topics in Applied Earth Observations*

and Remote Sensing, 7(7), 2895-2901.

Clark, R.N., Swayze, G.A., Leifer, I., Livo, K.E., Kokaly, R., Hoefen, T., Lundeen, S., Eastwood, M., Green, R.O., Pearson, N., Sarture, C., Mccubbin, I., Roberts, D., Bradley, E., Steele, D., Ryan, T., Dominguez, R., and AVIRIS Team, 2010. A method for quantitative mapping of thick oil spills using imaging spectroscopy. U.S. Geological Survey Open-File Report 2010-1167, 1-54.

Corbane, C., Najman, L., Pecoul, E., Demagistri, L., and Petit, M., 2010. A complete processing chain for ship detection using optical satellite imagery. *International Journal of Remote Sensing*, 31(22), 5837-5854.

Espedal, H.A., and Johannessen, O.M., 2000. Cover: Detection of oil spills near offshore installations using synthetic aperture radar (SAR). *International Journal of Remote Sensing*, 21(11), 2141-2144.

Fingas, M., and Brown, C., 2014. Review of oil spill remote sensing. *Marine Pollution Bulletin*, 83(1), 9-23.

Garcia-Pineda, O., Zimmer, B., Howard, M., Pichel, W., Li, X., and MacDonald, I.R., 2009. Using SAR images to delineate ocean oil slicks with a texture classifying neural network algorithm (TCNNA). *Canadian Journal of Remote Sensing*, 35(5), 1-11.

Hamrick, J.M., 1992. Estuarine environmental impact assessment using a three-dimensional circulation and transport model. *In Proceedings of Estuarine and Coastal Modeling, American*

Society of Civil Engineers, 292-303.

Heaton, J., 2008. Introduction to Neural Networks for Java, 2nd Ed. Heaton Research Inc., Chesterfield, MO, USA, 157-158

Hovland, H.A., Johannessen, J.A., and Digranes, G., 1994. Slick detection in SAR images. *In Proceedings of IEEE International Geoscience and Remote Sensing Symposium, Surface and Atmospheric Remote Sensing: Technologies, Data Analysis and Interpretation*, 4, 2038-2040.

Hu, C., Chen, S., Wang, M., Murch, B., and Taylor, J., 2015. Detecting surface oil slicks using VIIRS nighttime imagery under moon glint: A case study in the Gulf of Mexico. *Remote Sensing Letters*, 6(4), 295-301.

Hu, C., Müller-Karger, F.E., Taylor, C., Myhre, D., Murch, B., Odriozola, A.L., and Godoy, G., 2003. MODIS detects oil spills in Lake Maracaibo, Venezuela. *Eos, Transactions, American, Geophysical, Union*, 84(33), 313-319. doi: 10.1029/2003EO330002.

Jha, M.N., Levy, J., and Gao, Y., 2008. Advances in remote sensing for oil spill disaster management: State-of-the-Art sensors technology for oil spill surveillance. *Sensors*, 8(1), 236-255.

Keramitsoglou, I., Cartalis, C., and Kiranoudis, C.T., 2006. Automatic identification of oil spills on satellite images. *Environmental Modelling & Software*, 21(5), 640-652.

Kim, M., Yim, U.H., Hong, S.H., Jung, J.H., Choi, H.W., An, J., Won, J., and Shim, W.J., 2010. Hebei Spirit oil spill monitored on site by

fluorometric detection of residual oil in coastal waters off Taean, Korea. *Marine Pollution Bulletin*, 60(3), 383-389.

Kim, T.-S., Park, K.-A., Lee, M.-S., Park, J.-J., Hong, S., Kim, K.-L., and Chang, E., 2013. Application of bimodal histogram method to oil spill detection from a satellite synthetic aperture radar image. *Korean Journal of Remote Sensing,* 29(6), 645-655.

Kim, T.-S., Park, K.-A., Li, X., Lee, M., Hong, S., Lyu, S.J., and Nam, S., 2015. Detection of the Hebei Spirit oil spill on SAR imagery and its temporal evolution in a coastal region of the Yellow Sea. *Advances in Space Research*, 56(6), 1079-1093.

Kokaly, R.F., King, T.V., and Hoefen, T.M., 2011. Mapping the distribution of materials in hyperspectral data using the USGS Material Identification and Characterization Algorithm (MICA). *In Proceedings of IEEE International Geoscience and Remote Sensing Symposium,* 1569-1572.

Kostianoy, A.G., Litovchenko, K.Ts., Lebedev, S.A., Stanichny, S.V., Soloviev, D.M., and Pichuzhkina, O.E., 2005. Operational satellite monitoring of oil spill pollution in the southeastern Baltic Sea. *Oceans-Europe*, 1(4), 182-183. doi: 10.1109/OCEANSE.2005.1511706.

Kubat, M., Holte, R.C., and Matwin, S., 1998. Machine learning for the detection of oil spills in satellite radar images. *Machine Learning*, 30(2-3), 195-215.

Leifer, I., Lehr, W.J., Simecek-Beatty, D., Bradley, E., Clark, R., Dennison, P., Hu, Y., Matheson, S., Jones, C.E., Holt, B., Reif, M.,

Roberts, D.A., Svejkovsky, J., Swayze, G., and Wozencraft, J., 2012. State of the art satellite and airborne marine oil spill remote sensing: Application to the BP Deepwater Horizon oil spill. *Remote Sensing of Environment*, 124, 185-209.

Liu, W.T., Katsaros, K.B., and Businger, J.A., 1979. Bulk parameterization of air-sea exchanges of heat and water vapor including the molecular constraints at the interface. *Journal of the Atmospheric Sciences*, 36(9), 1722-1735.

Macdonald, I.R., Beet, A., Asl, S.D., Feng, L., and Graettinger, G., 2015. Natural and unnatural oil slicks in the Gulf of Mexico. *Journal of Geophysical Research: Oceans*, 120(12), 8364-8380.

Macdonald, I.R., Guinasso, N.L., Ackleson, S.G., Amos, J.F., Duckworth, R., Sassen, R., and Brooks, J.M., 1993. Natural oil slicks in the Gulf of Mexico visible from space. *Journal of Geophysical Research: Oceans*, 98(C9), 16351. doi: 10.1029/93JC01289.

Mao, Y., and Heron, M.L., 2008. The influence of fetch on the response of surface currents to wind studied by HF ocean surface radar. *Journal of Physical Oceanography*, 38(5), 1107-1121.

Marghany, M., 2014. Utilization of a genetic algorithm for the automatic detection of oil spill from RADARSAT-2 SAR satellite data. *Marine Pollution Bulletin*, 89(1-2), 20-29.

McNutt, M.K., Camilli, R. Crone, T.J., Guthrie, G.D., Hsieh, P.A., Ryerson, T.B., Savas, O., and Shaffer, F., 2012. Review of flow

rate estimates of the Deepwater Horizon oil spill. *In Proceedings of National Academy of Sciences of the United States of America*, 109(50), 20260-20267.

Mera, D., Cotos, J.M., Varela-Pet, J., Rodríguez, P.G., and Caro, A., 2014. Automatic decision support system based on SAR data for oil spill detection. *Computers & Geosciences*, 72, 184-191.

Mobley, C.D., 1999. Estimation of the remote-sensing reflectance from above-surface measurements. *Applied Optics*, 38(36), 7442-7455.

Møller, M.F., 1993. A scaled conjugate gradient algorithm for fast supervised learning supervised learning. *Neural Networks*, 6(4), 525-533.

National Research and Council, 2003. Oil in the Sea III: Inputs, Fates, and Effects. The National Academies Press, Washington, D.C., USA, pp. 280.

National Response Team, 1989. The Exxon Valdez Oil Spill. A Report to the President, pp. 75.

OSPAR, 2010. North Sea manual on maritime oil pollution offences, London, UK. pp. 91.

Park, K.-A., Cornillon, P., and Codiga, D.L., 2006. Modification of surface winds near ocean fronts: Effects of Gulf Stream rings on scatterometer (QuikSCAT, NSCAT) wind observations. *Journal of Geophysical Research*, 111(C3), C03021.

Price, J.M., Reed, M., Howard, M.K., Johnson, W.R., Ji, Z.G., Marshall, C.F., Guinasso Jr., N.L., and Rainey, G.B., 2006. Preliminary

assessment of an oil-spill trajectory model using satellite-tracked, oil-spill-simulating drifters. *Environmental Modelling & Software*, 21(2), 258-270.

Reed, M., Turner, C., and Odulo, A., 1994. The role of wind and emulsification in modelling oil spill and surface drifter trajectories. *Spill Science & Technology Bulletin*, 1(2), 143-157.

Salisbury, J.W., D' Aria, D.M., and Sabins Jr., F.F., 1993. Thermal infrared remote sensing of crude oil slicks. *Remote Sensing of Environment*, 45(2), 225-231.

Solberg, A.H., and Solberg, R., 1996. A large-scale evaluation of features for automatic detection of oil spills in ERS SAR images. *In Proceedings of IEEE International Geoscience and Remote Sensing Symposium, Remote Sensing for a Sustainable Future,* 3, 1484-1486.

Solberg, A.H.S., Dokken, S.T., and Solberg, R., 2003. Automatic detection of oil spills in ENVISAT, Radarsat and ERS SAR images. *In Proceedings of IEEE International Geoscience and Remote Sensing Symposium*, 4(C), 2747-2749.

Solberg, A.H.S., Storvik, G., Solberg, R., and Volden, E., 1999. Automatic detection of oil spills in ERS SAR images, *IEEE Transactions on Geoscience and Remote Sensing,* 37(4), 1916-1924.

Topouzelis, K., Karathanassi, V., Pavlakis, P., and Rokos, D., 2007. Detection and discrimination between oil spills and look-alike phenomena through neural networks. *ISPRS Journal of*

Photogrammetry and Remote Sensing, 62(4), 264-270.

Wettle, M., Daniel, P.J., Logan, G.A., and Thankappan, M., 2009. Assessing the effect of hydrocarbon oil type and thickness on a remote sensing signal: A sensitivity study based on the optical properties of two different oil types and the HYMAP and Quickbird sensors. *Remote Sensing of Environment,* 113(9), 2000-2010.

White, H.K., Hsing, P.-Y., Cho, W., Shank, T.M., Cordes, E.E., Quattrini, A.M., Nelson, R.K., Camilli, R., Demopoulos, A.W.J., German, C.R., Brooks, J.M., Roberts, H.H., Shedd, W., Reddy, C.M., and Fisher, C.R., 2012. Impact of the Deepwater Horizon oil spill on a deep-water coral community in the Gulf of Mexico. *In Proceedings of National Academy of Sciences of the United States of America,* 109(50), 20303-20308. doi: 10.1073/pnas.1118029109.

Wu, G., de Leeuw, J., Skidmore, A.K., Liu, Y., and Prins, H.H.T., 2009. Performance of Landsat TM in ship detection in turbid waters. *Performance of Landsat TM in ship detection in turbid waters*, 11(1), 54-61.

Xu, Q., Cheng, Y., Liu, B., and Wei, Y., 2015. Modeling of oil spill beaching along the coast of the Bohai Sea, China. *Frontiers of Earth Science*, 9(4), 637-641.

Zhang, B., Perrie, W., Li, X., and Pichel, W.G., 2011. Mapping sea surface oil slicks using RADARSAT-2 quad-polarization SAR image. *Geophysical Research Letters*, 38(10), 1-5.

Zhao, J., Temimi, M., Ghedira, H., and Hu, C., 2014. Exploring the potential of optical remote sensing for oil spill detection in shallow coastal waters—a case study in the Arabian Gulf. *Optics Express*, 22(11), 13755–13772.

PART II. Speckle

Chapter 1. Introduction

The suspended particulate matter (SPM) is one of the ocean variables representing the state of the seawater and been an important factor affecting marine biological mechanisms and fisheries (Martin and Meybeck, 1979; Findlay et al., 1991; D' Sa et al., 2007). The SPM originates from various sources such as the resuspension of bottom deposits, river-borne particles, and eroded matter from coastal areas. The SPM contents are very high near the coast due to the resuspension of terrestrial or submarine particulate matter by tides, waves, and currents and the shallow bathymetry (Gordon et al., 1983). Recently, it was suggested as an indicator, providing information on the movement of coastal water, in other words coastal currents (Chen et al., 2010; Ryu et al., 2011).

Highly turbulent SPM has been observed with satellite optical sensors such as Coastal Zone Color Scanner (CZCS), SeaWiFS, or MODIS. The SPM dominantly radiates in the wavelength range of 500-600 nm (Robinson, 2004). The SPM concentration is determined using these wavelengths. There are several studies about SPM concentration estimations using optical satellite data (e.g., Clark et al., 1980; Sturm, 1983; Tassan, 1994; Clark et al., 1997; Doerffer and Schiller, 1997; Binding et al., 2003; Ruddick et al., 2003; Miller and McKee, 2004). Clark (1980) utilized the ratio of the spectral radiance at 440 nm and 550 nm of CZCS for Nimbus pre-launch

research. Ahn et al. (2001) suggested that the usage of the 555-nm single channel is effective to estimate the SPM in coastal areas. The Geostationary Ocean Color Imager (GOCI), launched in 2011, observed the Korean Peninsula with unprecedented high spatial resolution of 500 × 500 m (Fig. 1a) at one-hour intervals to produce SPM images including other oceanic variables such as chlorophyll-a concentration, water quality, and CDOM (Fig. 1b).

The seas around Korea, where GOCI was used, consist of various types of water such as clear dark water in the Northern Pacific area and the East Japan Sea, sandy turbid water near estuaries, temporally fluctuated water in tidal mixing zones, and intermediate water. Clear water contains 0–0.1 g/m^3 SPM. On the contrary, water near estuaries reaches SPM values if 300 g/m^3. The SPM especially varies in the Yellow Sea because most of the river mouths, which are SPM sources, are located there and the tidal current is strong. Due to the characteristics of the visible/NIR channel, the ocean color cannot be observed when clouds cover the water. It is usually cloudy over the seas around Korea, ~240-300 days per year, mostly during winter; it is clear in autumn. The speckles were observed near clouds in the case of the East Japan Sea, particularly in winter (Chae and Park, 2009; Park et al., 2013).

Contrary to the high capability of GOCI, the processed GOCI images contain highly anomalous values called speckles. The SeaWiFS data speckles of the chlorophyll-a concentration were detected and eliminated by a series of speckle removal techniques and composite

methods (Chae and Park, 2009; Park et al., 2012). Similarly, frequent GOCI speckles should be eliminated to enhance the data quality for further scientific analysis of the long-term temporal variation and relation to climate change. Although atmospheric and other corrections have been applied to satellite data, unpredictable errors can appear in level-2 data. Considering that level-2 data has been using by most users, it is crucial to remove the speckles from the ocean color data of the level-2 data (Park et al., 2012).

In this study, we aim (1) to classify the speckles of the level-2 GOCI SPM data into four types according to their appearance, (2) to investigate the characteristics of each speckle type, (3) to develop a method to remove the speckles, (4) to clarify their potential causes, and (5) to analyze the significance of the speckle removal for long-term changes.

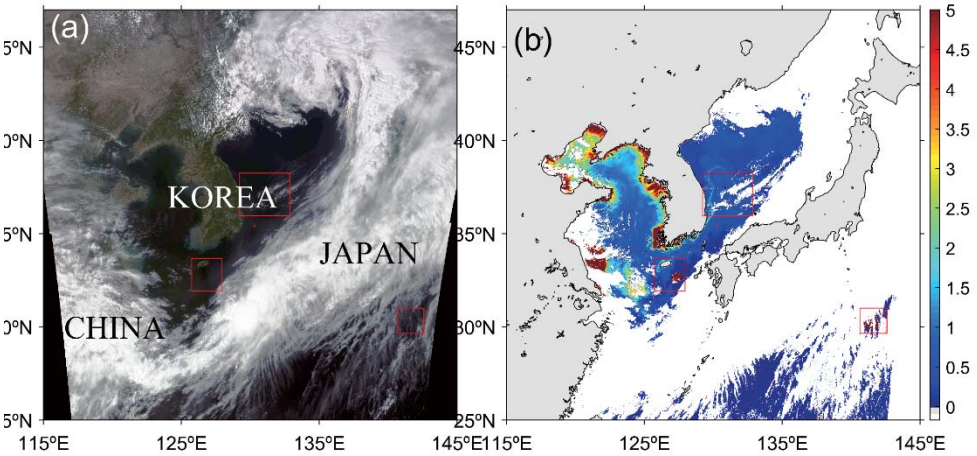

Fig. 1. (a) Geostationary Ocean Color Imager (GOCI) red–green–blue (RGB) image of the research area; (b) Suspended Particulate Matter (SPM) concentration (g/m^3), red boxes indicate examples of speckles.

Chapter 2. Data and Method

GOCI on board the Communication, Ocean and Meteorological Satellite (COMS), launched in June 2010 by the Korea Aerospace Research Institute (KARI), is an ocean color sensor making observations of the seas around the peninsula (24.75°N–47.25°N, 113.4°E–146.6°E) eight times a day from 9 AM to 4 PM with a 500 m × 500 m spatial resolution (Fig. 1). A whole GOCI image is obtained using the 16-slot step-and-stare scanning method. It has six visible (412, 443, 490, 555, 660, and 680 nm) and two near-infrared (NIR) channels (745 and 865 nm) with a 20-nm bandwidth. The GOCI level-2 remote sensing reflectance (R_{rs}) and SPM data for the period from April 2011 and September 2016 were obtained from the Korea Ocean Satellite Center (KOSC).

The KOSC provided radiometrically and geometrically corrected level-1 radiance data completed and level-2 R_{rs} data. An atmospheric correction was applied to level-1 radiance data while converting the data from level 1 to level 2. The land region was masked before the atmospheric correction and the gaseous absorption and whitecap radiance were corrected (Frouin et al., 1996). The radiance was then converted to reflectance. The reflectances observed by the satellite are mixed signals originating

from various sources such as Rayleigh scattering, aerosol scattering, and genuine seawater reflectance. The Rayleigh scattering effect was removed based on the channel wavelength, date, time, solar zenith angle, solar azimuth angle, satellite zenith angle, and satellite azimuth angle of each pixel. If the Rayleigh corrected reflectance of 865 nm was greater than the threshold, the pixel was classified as cloud and masked. Black pixel assumption, which means that there is no radiation from seawater in NIR wavelength range such as 745 nm and 865 nm, was utilized to determine the effect of aerosol scattering (Wang and Gordon, 1994). However, there are various sources of aerosol in the atmosphere between the sea surface and satellite. The GOCI uses three types of aerosol models: the maritime aerosol model with 99% relative humidity (M99), maritime aerosol model with 50% relative humidity (M50), and coastal aerosol model with a relative humidity of 50% (C50; Shettle and Fenn, 1979). In the case of turbid water, another process is needed. The reflectances are iteratively corrected using the relations between 660 nm, 745 nm, and 865 nm (Ruddick et al., 2006). The vicarious calibration uses the correlations between 660 nm and 745 nm and between 745 nm and 865 nm. Subsequently, the ocean reflectance can be determined.

Robinson (2004) reported the spectral characteristics of SPM, which indicate that the SPM concentration is sensitive at ~550 nm and has a positive relation to the wavelength. The GOCI has several visible channels that are suitable to detect SPM and provides a SPM algorithm. The SPM algorithm used in this study is the Yellow Sea

Large Marine Ecosystem Ocean Color Work Group (YOC) algorithm, a default algorithm of the GOCI data processing system (Tassan, 1994; Siswanto et al, 2011).

$$\mathrm{SPM} = 10^{\left(0.649+25.623\left(R_{rs}(555)+R_{rs}(660)\right)-0.646\left(\frac{R_{rs}(490)}{R_{rs}(555)}\right)\right)} \quad (1)$$

The SPM (g/m^3) consists of the ratio of the wavelengths of 490 nm and 555 nm and the sum of the wavelengths of 660 nm and 555 nm.

Chapter 3. Results

3.1. Speckle Types

The level-2 SPM data shows various kinds of speckles. The most common example of a speckle type appears near clouds over the seas with 10^2–10^{38} g/m^3 SPM (Fig. 2). In addition, not only the very large range of speckles but also the values of 3–20 g/m^3 are rarely observed in clear water. The second type includes isolated speckles represented as one or two pixels in the sea area. The sampled isolated speckles have a SPM concentration of 67.9730 g/m^3, which is greater than that of the surrounding area, although it is lower than that of the previous two types of speckles. There is also a case high SPM values of 5.0×10^2–1.16×10^6 g/m^3 over a large patch-shaped area, which often is visible from May to August. Fig. 2d shows an example of a patch-shaped speckle appearing in the southeast of Jeju; the clear border is a distinct feature. Finally, a speckle with a large region and sharp boundary has been observed at the bottom of slots.

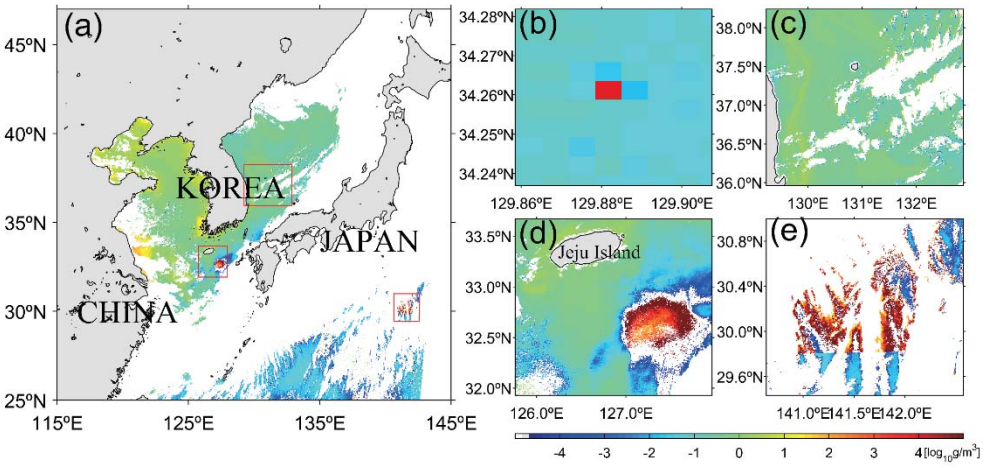

Fig. 2. (a) Geostationary Ocean Color Imager (GOCI) suspended particulate matter (SPM) concentration ($\log_{10}$ g/m^3) image of the research area, examples of (b) isolated, (c) cloud edge, (d) patch-shape, and (e) slot-related speckles at 4 UTC on June 3, 2015.

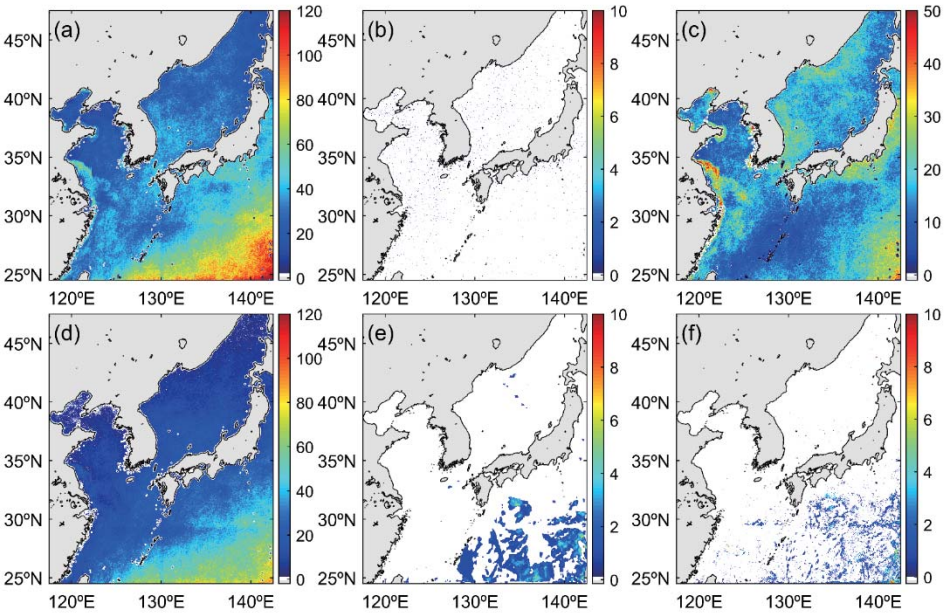

Fig. 3. The frequency of the speckle distribution map based on each speckle type in 2015. (a) total number, (b) isolated, (c) near cloud with high suspended particulate matter (SPM), (d) induced by cloud shadowing, (e) patch type, and (f) not near cloud.

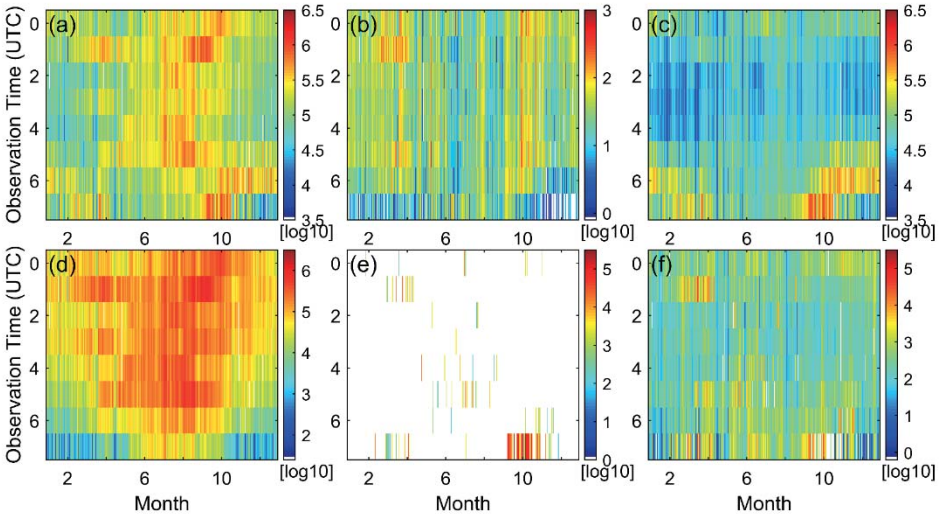

Fig. 4. Month–time plot of the number of speckles based on each speckle type in 2015. (a) total number, (b) isolated, (c) near cloud with high suspended particulate matter (SPM), (d) induced by cloud shadowing, (e) patch type, and (f) not near cloud.

3.1.1. Isolated Speckles

An example for the spatial distribution of an isolated speckle is shown in Fig. 2b. The pixel including the SPM speckle is relatively brighter than the neighboring pixels in the red-green-blue (RGB) image of the near isolated speckle. The isolated speckle in the sea area has a SPM concentration of 67.97 g/m^3. Isolated speckles are randomly distributed all over the oceans (0-10$^{2.5}$ pixels in an image). The largest number of speckles was observed in the Yellow Sea; the smalles amount was detected in the south of Japan (Fig. 3b). Isolated speckles appear rarely in summer and often in spring and autumn (Fig. 4b). The number of isolated speckles is smaller at 7 UT in winter than that during other times.

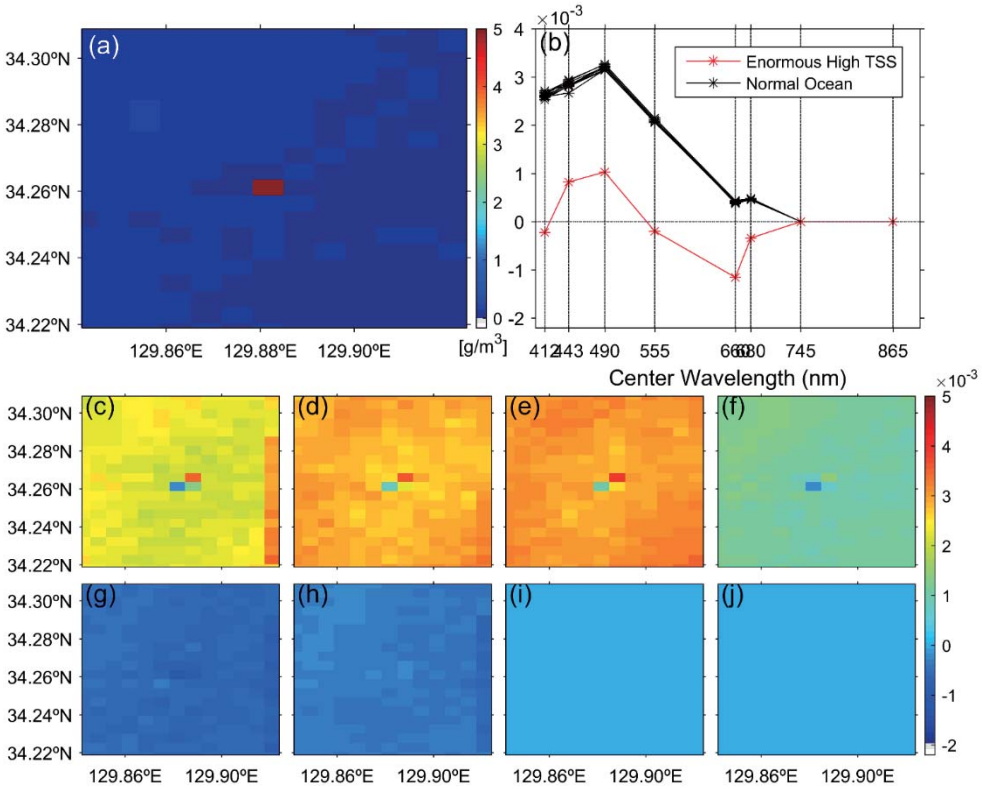

Fig. 5. (a) Suspended Particulate Matter (SPM) with a cloud edge speckle, (b) level-2 spectral remote sensing reflectances of the isolated speckle and non-speckle and spatial remote sensing reflectances of the (c) 412 nm, (d) 443 nm, (e) 490 nm, (f) 555 nm, (g) 660 nm, (h) 680 nm, (i) 745 nm, and (j) 865 nm-centered wavelength channels.

3.1.2. Speckles Near/Along Clouds

There are three types of abnormal values near clouds such as enormously high values > 10^3 and a SPM of 3–100 g/m^3. The much lower values than usual caused by cloud shadowing nearby high values appear like a set. Pixels not completely masked near clouds were substituted in the SPM algorithm, which led to enormously high value. The pixels with large SPM values > 10^5 g/m^3 are shown in Fig. 2c.

The speckles near clouds account for ~90% of all speckles. This type of speckles is distributed widely over the whole study area, particularly concentrated at the East Coast and the southeast corner of the research area (Fig. 3c). The southern center of the research area shows a less amount of speckles due to the low data acquisition rate because clouds cover the area almost all day. The high-value speckles occur more often in autumn and winter. The time-month diagram of the number of high value speckles shows a radial shape (Fig. 4c). At the transition from autumn to winter, the time of appearance of speckles with more than $10^{5.5}$ pixels in an image changed from 7 UT to 5 UT (Fig. 4c). On the contrary, the time of appearance of speckles with pixels > $10^{5.5}$ of pixels changed from 5 to 7 UT at the transition from winter to summer. Speckles with a lower SPM content caused by cloud shadowing occur mostly in the southern part of the research area (Fig. 3d) at 1 and 5 UT in summer (Fig. 4d).

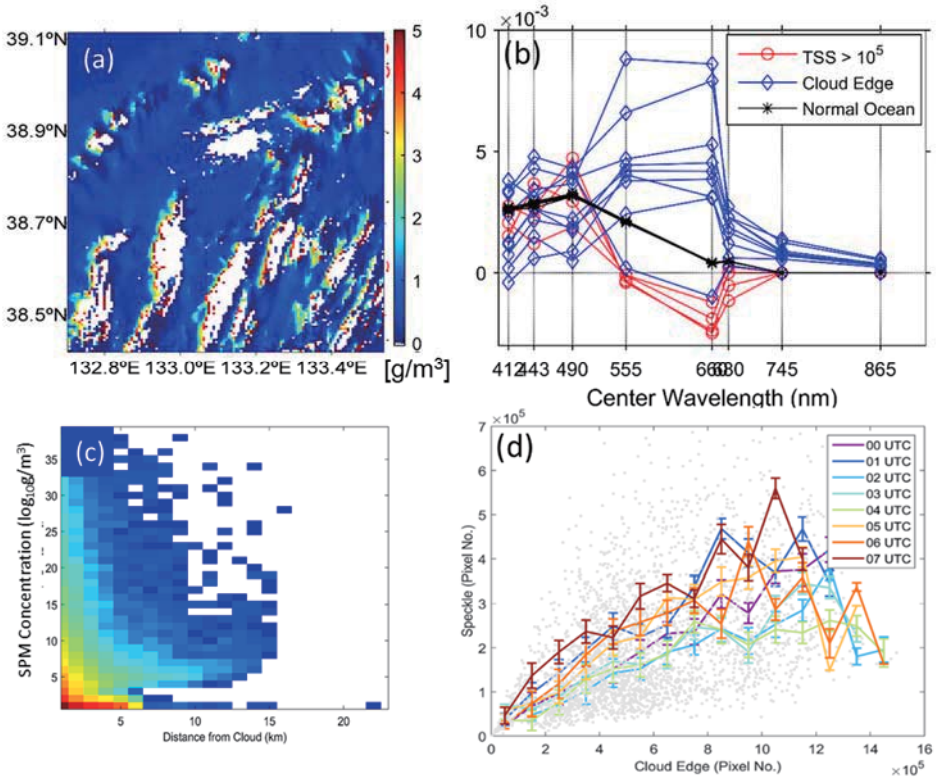

Fig. 6. (a) Suspended Particulate Matter (SPM) with a cloud edge speckle, red circles indicate the pixels > 10^5; (b) spectral remote sensing reflectance > 10^5 g/m^3, cloud edge and non-speckle.

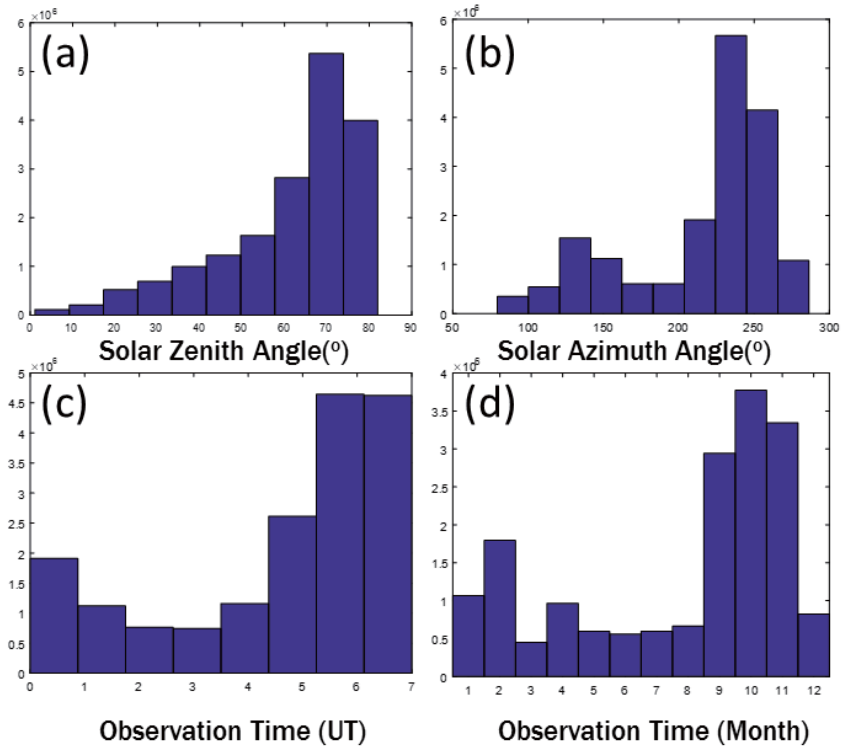

Fig. 7. Histogram of the speckle numbers for each (a) solar zenith angle, (b) solar azimuth angle, (c) observation time, and (d) month.

3.1.3. Patch-type Speckles

Large areas showing patch−shaped speckles have high SPM values ranging from 5.0×10^{2}–1.16×10^{6} g/m^{3}. For example, a patch−shaped speckle with a width of 0.5° × 0.7° was observed in June (Fig. 2d). This type of speckle appears relatively rarely but widely. The extent of it ranges from 60 to 30,000 km^{2} in an SPM image (Fig. 3e). It is concentrated over the Northwest Pacific at 1 and 7 UT from February to March and from September to October (Fig. 4e). During the rest of those months, it usually appears from 2 to 6 UT. The patch−type speckle is rare in winter.

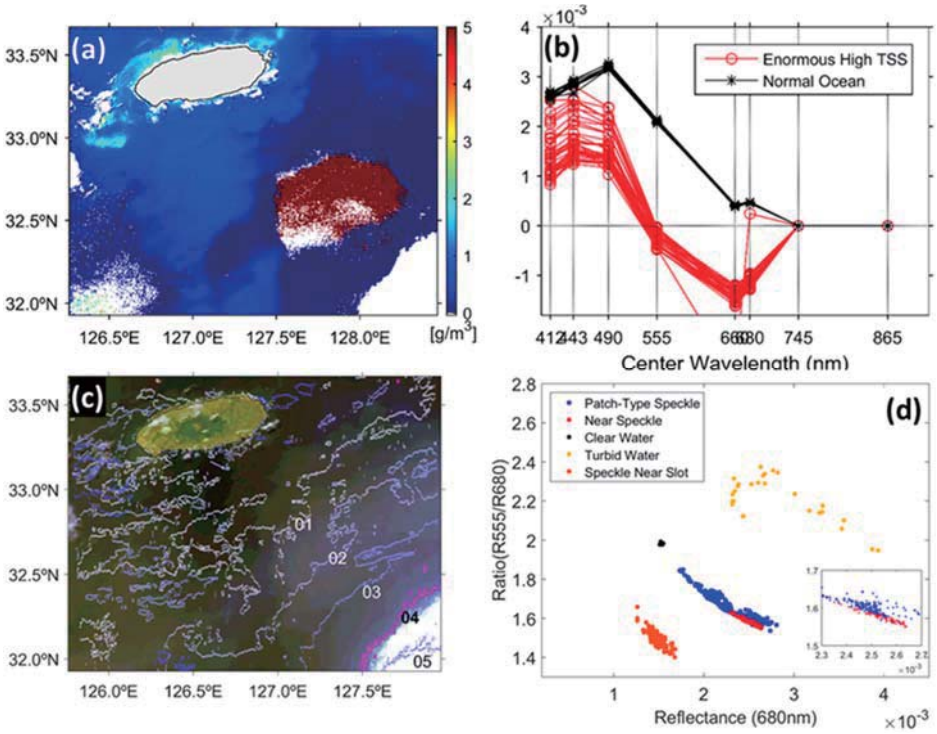

Fig. 8. (a) Suspended Particulate Matter (SPM) concentration with a patch-shape speckle, (b) spectral remote sensing reflectances of the patch-shape speckle and non-speckle, (c) temporal cloud movement, (d) ratio of Rrs(555) to Rrs(680) as a function of $R_{rs}(680)$.

3.1.4. Slot-related Speckles

The southeastern part of Fig. 2a shows an enormously high SPM concentration. Its shape is cropped discontinuously at the transition line of slots (Fig. 2e). The GOCI observes the whole area with 16 slots. The speckle occurs at the bottom of the 12th slot. The RGB image (Fig. 1a) shows that the speckle at the bottom of the slot is redder than the neighboring speckle-free ocean-like saturated film. In addition to the three types of speckles described above, a significant number of unidentified speckles remain (Fig. 3f). This type of speckle was mostly present along the bottom boundary of slots, particularly at slot numbers of 9-15 in the southeastern part of the research area. The speckles along the bottom of slots tend to be present in association with a large number of patch-type speckles (Figs 4e-f) because the speckles near the slot bottom have a wide extent.

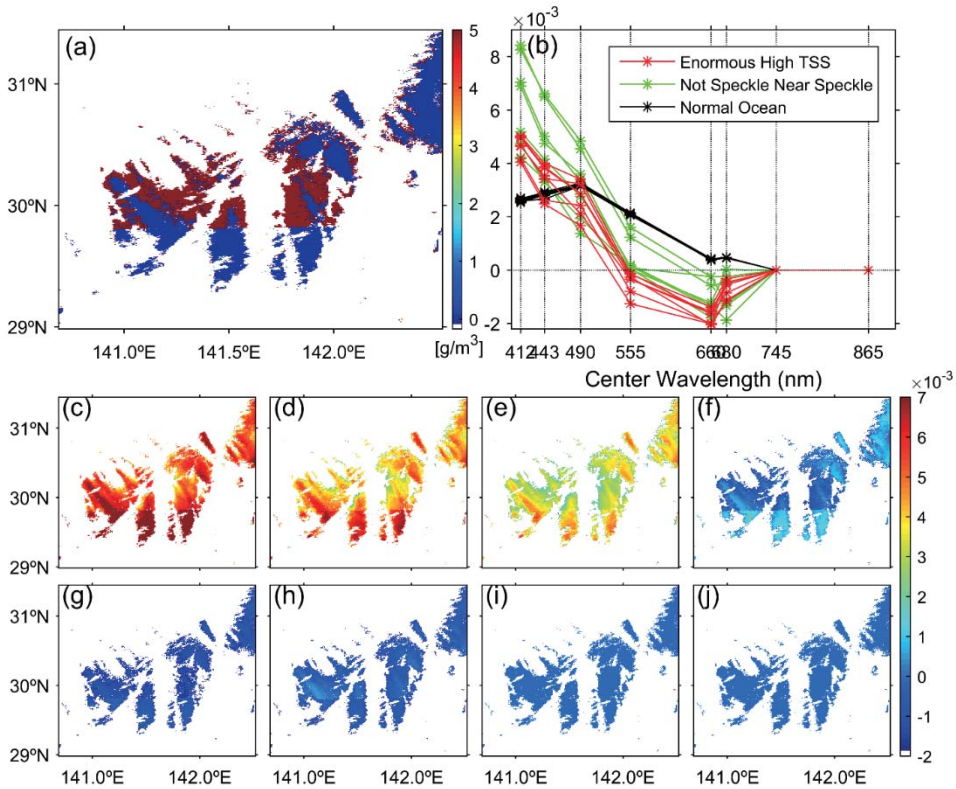

Fig. 9. (a) Suspended particulate matter (SPM) concentration with speckle near the slot edge, (b) spectral remote sensing reflectances of enormously high SPM near the speckle and normal ocean and its spatial remote sensing reflectances of the (c) 412 nm, (d) 443 nm, (e) 490 nm, (f) 555 nm, (g) 660 nm, (h) 680 nm, (i) 745 nm, (j) 865 nm-centered wavelength channels.

3.2. Causes of Speckles

3.2.1. Cloud Movement

As an example of cloud movement, Fig. 5 shows the movement of an unmasked speckle. The cloud has a high R_{rs} in all visible channels (Frey et al., 2008). At the location of the speckle, the R_{rs} of the visible channels is lower than that of the neighbors. However, the abnormally high values move one pixel northeastward in the spatial distribution of each visible channel compared with the SPM speckle location because the seas around Korea are in the westerly wind zone. It is supposed to be induced by the cloud movement during the time gap between the 745 and 865 nm channels used for the atmospheric correction. The GOCI uses an iteration scheme of the ratio between 745 and 865 nm channels for the atmospheric correction. If the cloud moves during the two-channel observation (52 s, wind speed > 9.7 m/s), the ratio of the two channels is disturbed and causes an error in the estimation of the atmospheric condition and correction.

However, the relative spectral R_{rs} shape in the range from 412 to 660 nm is similar to that of other neighboring pixels; each R_{rs} value of the isolated speckle is lower than -2×10^{-3}. The spectral R_{rs} is significantly different compared with that of the speckle-free area (black line in Fig. 5b). The R_{rs} > 680 nm is not different from that of the speckle-free area. The sum of $R_{rs}(555)$ and $R_{rs}(660)$, the component of the SPM algorithm, is negative; however, the $R_{rs}(490)$

is positive (Fig. 5b). The spectral characteristics indicate that the ratio of the small negative $R_{rs}(555)$ and the large positive $R_{rs}(490)$ significantly increases the R_{rs} value [$-0.646 \times R_{rs}(490)/R_{rs}(555)$].

The isolated speckle is supposed to be generated by an unmasked small cloud fraction smaller than one pixel and a fast-moving small cloud. The GOCI observes the ocean in the following order: 660-555-745-443-680-412-865-490-nm channels (Ahn et al., 2012). The duration of a sequence is 103 s. Because the SPM algorithm is substituted by 490, 555, and 660 nm, there is a time gap between each channel ranging from 13-90 s. If the wind speed is higher than 5.6 m/s (500 m/90 s = 5.6 m/s, 500 m/13 s = 38.5 m/s), clouds can move to the next pixel during the scan of the same area. The cloud masking is based on the R_{rs} of the 412- and 865-nm channels; the time gap between the observations of the channel used in cloud masking and each observation time of other channels for SPM concentration ranges from 13-77 s. Thus, there is a possibility that the cloud is incompletely masked when the wind blows faster than 6.5 m/s. It is common that the wind speed is higher than 10 m/s over the ocean; the speckles induced by cloud movement therefore occur frequently. A pixel value with a radiance smaller than the threshold of the cloud masking is processed using an atmospheric correction and substituted in the SPM algorithm and yields an abnormal high SPM value.

3.2.2. Cloud and Cloud Shadowing

There are three ranges of SPM values near clouds: enormously high values > 10^3 g/m^3 and 3–10^2 g/m^3, which can be observed in the turbid coastal water but not in the clear water (Fig. 1b) and values smaller than half of the climatology data of the same month (Fig. 6a). Fig. 6b shows the spectral R_{rs} of the three types and general clear seawater. In the case of enormously high values, the spectral R_{rs} has characteristics similar to the isolated one. The spectral R_{rs} is significantly different compared with that of the speckle-free area (black line in Fig. 6b). Especially the 555 and 660 nm channels of the SPM algorithm show negative values; the 490 nm channel is positive (Fig. 6b). Therefore, the sum of $R_{rs}(555)$ and $R_{rs}(660)$ is negative and lowers the SPM value, while the ratio of the small negative $R_{rs}(555)$ and high positive $R_{rs}(490)$ significantly increases the value of $-0.646\times R_{rs}(490)/R_{rs}(555)$. While turbid water has a single peak at 555 nm (Robinson, 2004), cloud edges (3–10^2 g/m^3) have no single peak but similar $R_{rs}(555)$ and $R_{rs}(660)$ values. This increases the sum of $R_{rs}(555)$ and $R_{rs}(660)$, a term of the SPM algorithm, and results in a higher SPM concentration compared with the real SPM content. This spectral characteristic is due to contamination by the reflectance of thin clouds and cloud movement. The speckles with low values are generated by low reflectances due to cloud shading.

Fig. 6c shows that the SPM concentration of the speckles is higher closer to cloud edge. The speckle amount does not correlate with the

cloud extent but with the cloud edge extent. Fig. 6d shows the number of speckles as function of the cloud edge extent (pixel number) with the mean and standard deviation for each observation time (UT). As mentioned before, number of speckles is lower at 7 UTC in winter than at 6 UT and in autumn because the observed pixel number at that time is limited by the low solar zenith angle and the low power of R_{rs} from the ocean. In addition, the speckle appearance is related to the solar zenith angle. The histogram of the speckle numbers for each range of solar zenith angles confirms this (Fig. 7). The seasonal and temporal variability of the speckles significantly depends on the solar zenith angle change.

3.2.3. Atmospheric Correction for Water Vapor

Fig. 8a shows a patch-type speckle near Jeju Island. The spectral shape is similar to the extremely high value of the speckle near a cloud (Fig. 8b). Fig. 8c shows RGB images from 4 UT on June 6, 2015. The white and purple colored lines in the image represent the boundary of the cloud for each time from 1 to 5 UT. Thick clouds covering the patch-type speckle appeared, moved eastward, and left behind moisture, which caused an error in the atmospheric correction, especially during the removal of the scattering effect induced by aerosol. The pixels in a patch have a consistent spectral R_{rs} and SPM values significantly different from area around the patch (Fig. 8d). Based on the comparison with the spectral characteristics of the isolated speckle and enormously high speckle numbers near the cloud, we infer that these types of speckles have the same cause. In particular, the relative spectral R_{rs} values are similar to those of the normal ocean in the range of 490–680 nm; however, the visible value shifted by approximately -1.5×10^{-3} (red in Fig. 8b). The values of the 555-nm, 660-nm, and 680-nm channels are negative and that of the 490-nm channel is positive. Therefore, the sum of $R_{rs}(555)$ and $R_{rs}(660)$ is negative and lowers the SPM concentration. The ratio of the small negative $R_{rs}(555)$ and the large positive $R_{rs}(490)$ is $-0.646 \times R_{rs}(490)/R_{rs}(555)$.

The reflectances at 0.865 and 0.936 μm are used to detect thin cloud or fog; the reflectances at 6.715 μm, 8.550 μm, and 12.020

μm can be utilized to discriminate high, mid, and low-moisture conditions (Ackerman et al., 1998). The discrimination of pixels with low stratus and moistures using only GOCI data is not fully understood, yet, because most of these channels, except for 0.865 μm, are not included in GOCI.

3.2.4. Sensor Calibration

Fig. 9a shows an extension of a slot-related speckle (see Fig. 1b). The characteristics of the speckle area on the 12th slot and speckle-free area on the 13th slot are shown as red and green lines in Fig. 9b. Although the relative pattern of each channel is similar between the red and green lines, the signs of their reflectance at 555 nm are clearly different. The reflectance of the speckle has a negative value at the 555-nm channel, which causes the amplification of the SPM value in the SPM algorithm. Similar to other types of speckles, it has negative reflectances at 555 nm, 660 nm, and 680 nm. However, it shows relatively high reflectances at 412 nm and 443 nm, similar to that of the clear ocean.

Figs. 9c–j illustrate the decreasing tendency toward the lower part of the slot in most of channels, except for 680 nm, which is due to the fact that the atmospheric correction of aerosol scattering is based on the reflectance at 680 nm. Due to the abnormal high reflectance at 680 nm, reflectances of the visible channels have overcorrected aerosol scattering data in the lower part of the slot. It has been reported that the radiance detected in the lower part of the slot shows a higher value due to the stray light generated by internal circumstances in the sensor (Kim et al., 2015). Therefore, if the reflectances of the 555-nm channel have a negative sign due to overcorrection, the calculated SPM contains an error.

3.3. Removal Process of Speckles

To remove the speckle from the level-2 hourly GOCI SPM image, we set the definition of speckle appearance based on its characteristics and developed the speckle removal procedure. Fig. 10 illustrates the flowchart for the speckle detection; a detailed description of each step is provided in the following section. First of all, the monthly climatology map was calculated for the speckle detection, in advance. To create climatology data, we used the SPM data from 2-4 UT when it was relatively clear to observe the ocean. The SPM values > 10^3 g/m^3 in each image were firstly removed because high SPM concentration values are at most ~300 g/m^3 near the Changjian River Mouth. The median values at the same location in a month were selected as climatology value to avoid the inclusion of high or low values induced by the speckle.

A SPM image was preprocessed by land and cloud masking. Pixels > 10^3 g/m^3 were preferentially detected. The pixels located near the coast within a distance of less than 10 km from land were excluded from the speckle detection. To detect the speckles in the clear water, such as the Northwest Pacific, we identified pixels with a SPM value > 2 g/m^3. However, the monthly climatology indicates values lower than 0.1 g/m^3 for the same location. To automatically find isolated speckles, an adaptive index was utilized. The difference between the ratio of a mean 3 × 3 window standard deviation and the ratio of the

mean standard deviation of the 3 × 3 window excluding the center value is greater than 0.1 when solely isolated speckles exist over the normal ocean. Subsequently, we utilized a monthly climatology map to identify abnormal values due to clouds. The SPM values of cloud-induced speckles are two times greater than the climatology data, > 1.5 g/m^3 or less than half of the climatology data near clouds (distance < 5 km). The correlation between the SPM value of the speckle and the distance from the cloud sharply decreases in the histogram at 5 km (Fig. 6c).

After the speckle detection, the speckles were classified into four types and masked from the SPM concentration data. The isolated speckle is the only speckle in the 3 × 3 window and > 5 km away from clouds. The patch-type speckle accounts for > 80% of the 70 km × 70 km window. The remaining speckles were divided into near-cloud speckles (< 5 km) and speckles not near clouds. The quantities of each speckle type and location were saved and utilized to determine the speckle characteristics.

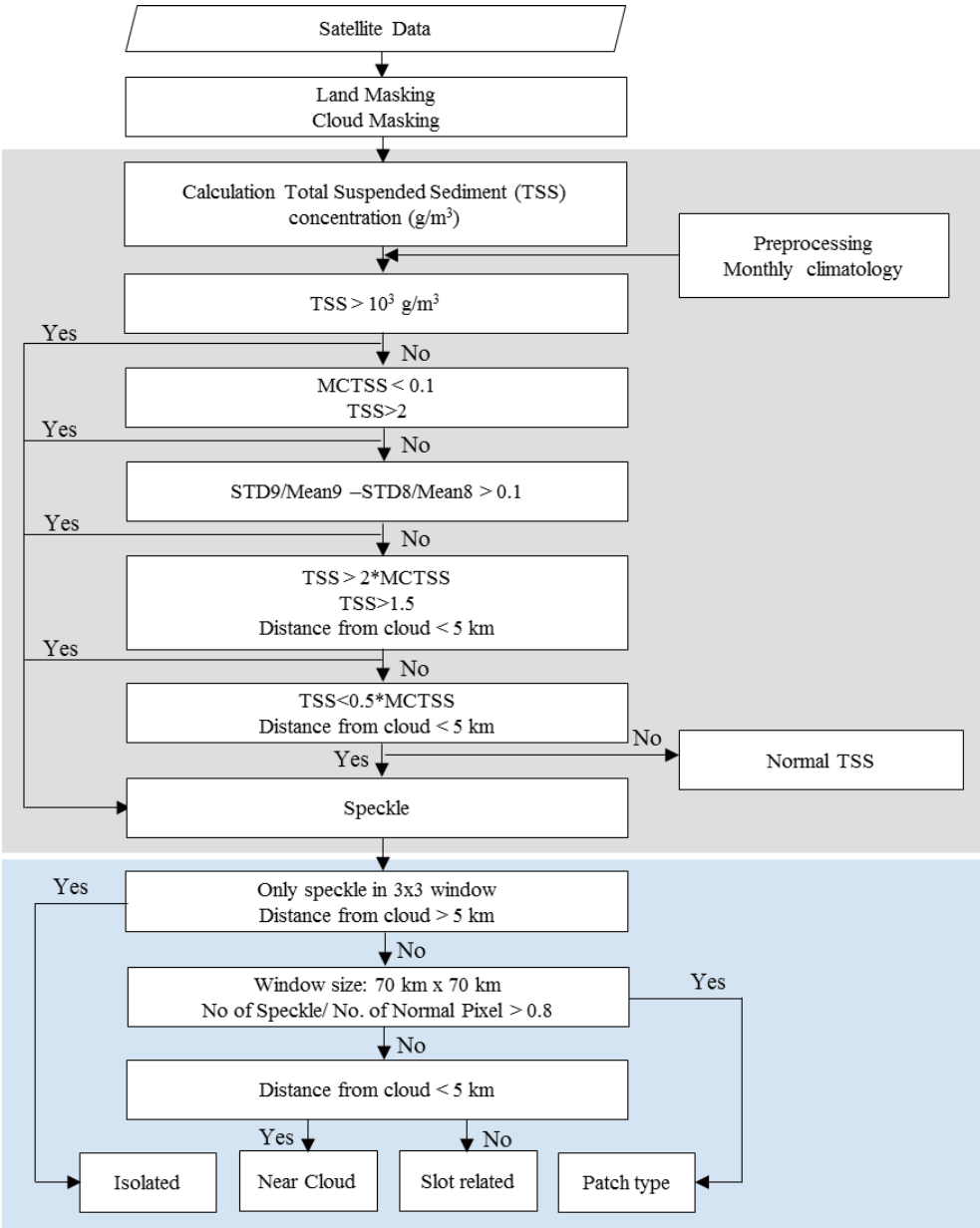

Fig. 10. Flow chart of the speckle removal process for the Geostationary Ocean Color Imager (GOCI) suspended particulate matter (SPM) data.

3.4. Comparison with a Reprocessed SPM Map

The results of the speckle removal procedure applied to each of the sampled regions are shown in Fig. 11. The patch-type and near-cloud speckles have values > 10^2 g/m^3, the pixels with SPM concentrations ranging from 3–10^2 g/m^3 near the cloud edge were also removed with the speckle removal procedure (Fig. 11b). After the speckle removal procedure, high-quality SPM data were obtained. To check the effect of the speckle removal, we counted the speckles that were removed in each subsample region (Fig. 11c). In the case of near-cloud speckles, 6.22% of speckles of the subsampled region were eliminated. As a result, 1.42×10^{33} of the mean value was corrected to 0.59 g/m^3. Patch-type speckles cover 5.85% of the second subsampling area; as a result, 3.18×10^{34} of the mean value changed to 0.35 g/m^3. The mean value of 0.90 g/m^3 of isolated speckles was fixed to 0.39 g/m^3 because only one speckle was removed. Although there were not many speckles in the data, the impact on the mean value of whole area is significant.

Monthly composite data were used to determine the seasonal SPM variation. Based on the raw SPM concentration data, salt and pepper-shaped speckles appeared over the whole area in the monthly composite (Fig. 12). The SPM generally has low SPM concentrations (< 1 g/m^3) in the center of the East Sea. However, there is a significant number of red dots with high values > 3 g/m^3. Especially

in July, there is a cluster along the meridional side at the bottom of the 10th–12th slots. After the speckle removal process, the newly calculated monthly composite images show clear spatial patterns without speckles (Fig. 13). The red discontinuous patterns disappeared and the spatial SPM patterns became more distinctive.

To clarify the impact of the speckle removal, we reprocessed the level-2 SPM data (excluded the infinite value and data > 10^3) from April 2011 to August 2016 and compared the difference of the monthly minimum, maximum, median, and mean between them for 2-4 UT. There are lots of speckles in the whole research area in autumn and winter. The monthly mean mostly changed in summer, less in winter. The changing ratio of the monthly mean varied from 2.9% (January) to 21.2% (July). The maximum monthly value changed with amount of 75.2% (July). The minimum monthly SPM concentration increased, from 2.7% in February to 12.3% in June. The monthly maximum map mostly decreased; the monthly median decreased less. However, the monthly minimum map slightly increased. The ratio of the difference between raw data and reprocessed data of the whole area is relatively high (low) in summer (winter).

The most changes were observed near high-turbid water because a wide range of SPM concentrations could be easily discriminated. After speckle removal, almost all salt and pepper-shaped patterns with abnormally high SPM values disappeared. Therefore, the SPM

spatial patterns became clearer. The Northwest Pacific shows a relatively high SPM value change with respect to the monthly maximum (57.0%–93.8%) and monthly mean (16.5%–78.8%). The monthly minimum increased to 86.1% (19.6%) in August (June). Even small error corrections strongly affect the lower SPM region. While the monthly mean of the Yellow Sea with high SPM concentrations decreased to 1.0% (5.7%) in May (September), the monthly maximum decreased to 9.6% (20.3%) in January (July). The monthly mean of the East Sea with low SPM concentrations decreased to 0.2% (11.6%) of the raw data in March (June); the monthly maximum decreased to 58.1% (5.7%) in July (December). The monthly minimum increased to 31.4% (3.5%) in July (February). Fig. 14 shows the year to month variation of the ratio between the data before and after the speckle removal to GOCI level-2 SPM data.

Although speckles appear more frequently in winter than in summer, the corrected SPM value of the monthly mean is higher in summer than in winter. Therefore, the enormously high value induced by water vapor or thin clouds (patch-type and slot-related) usually appears in summer and is removed in reprocessed data. While the extraordinary high SPM value was corrected and its effect seems significant, the erroneous low value due to cloud shadowing was only slightly modified; patterns, such as the low-value patch in the monthly mean map, were removed and the SPM spatial pattern became clearer and more consecutive.

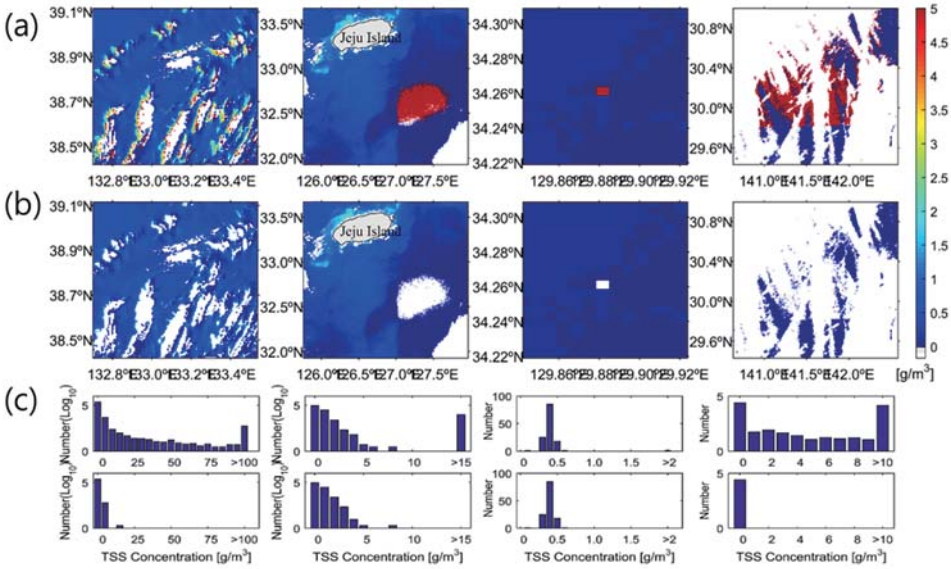

Fig. 11. (a) Examples of four types of speckles, (b) the result of the speckle removal, (c) suspended particulate matter (SPM) concentration histograms before and after the speckle removal.

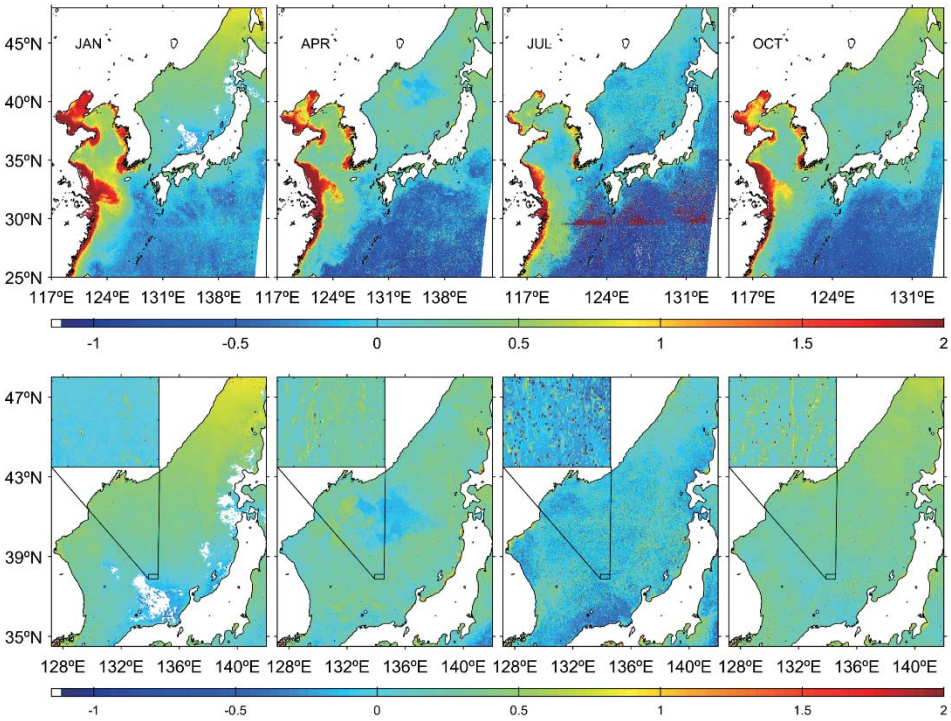

Fig. 12. Monthly composite images of raw suspended particulate matter (SPM) data and their extensions.

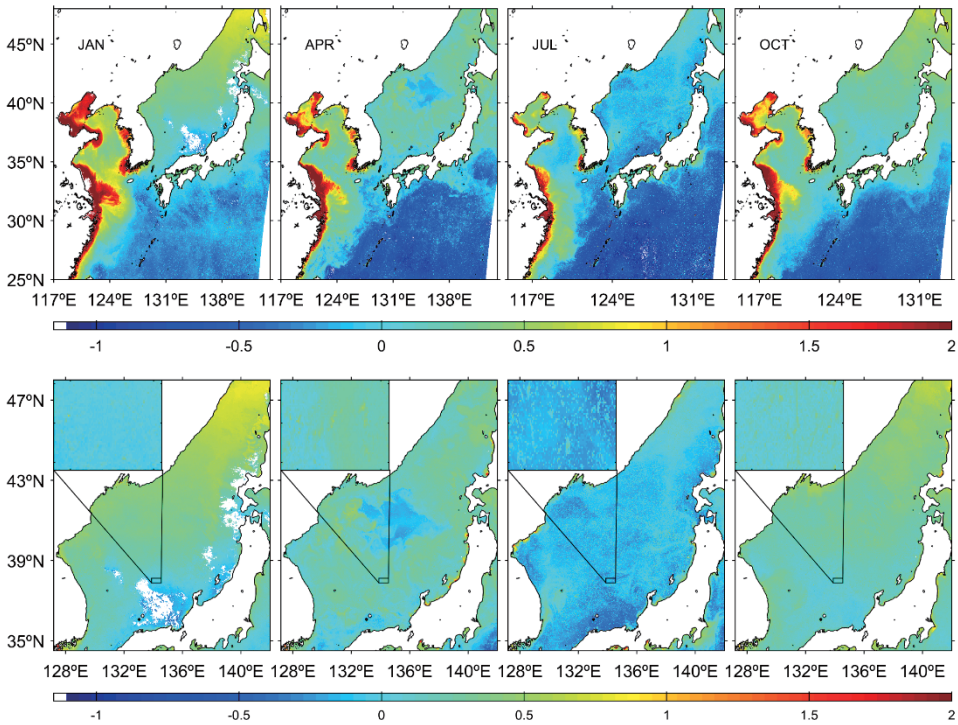

Fig. 13. Monthly composite images of reprocessed suspended particulate matter (SPM) data and their extensions.

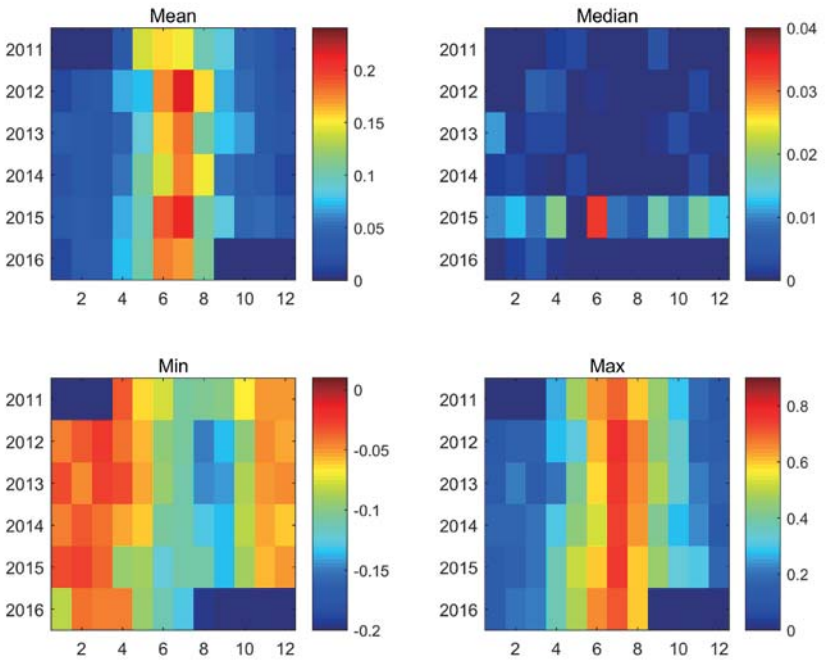

Fig. 14. Month to year ratio between the data before and after the speckle removal process.

Chapter 4. Summary and Conclusion

We classified speckles into four types based on their appearance, which have spectral reflectances different from that of the non-speckles. A speckle removal procedure was developed. The most common speckles have been observed near cloud edges, which have three ranges of speckle values such as enormously high values > 10^3 g/m^3 and 3–10^2 g/m^3 and less than half the value of the climatology data. The values ranging from 3–10^2 g/m^3 were difficult to discriminate because of similar SPM values in the turbid sea. For this reason, we utilized monthly climatology data and the distance from clouds in the speckle removal procedure.

Speckles appear more widely in autumn and winter than in summer and before or after noon. The number of speckles increases with the increase of the solar zenith angle or cloud edge extent. Therefore, not the most cloudy areas but moderately cloudy areas show lots of speckles induced by the clouds, particularly over the northern part of the East Sea in winter.

The speckles can be classified based on their appearance but can be defined based on their potential causes such as cloud movement during sensor scanning, imperfection of cloud masking induced by thin clouds, undetectable water vapor due to the absence of an IR channel, and location in a slot, which can be corrected by sensor

calibration. Some of these problems can be solved by improving the atmospheric correction and sensor calibration. However, others cannot be corrected due to the fundamental sensor characteristics and natural phenomena such as scanning time, scanning schedule by channel, and cloud movement. For these reasons, we have to use reprocessed data to investigate the temporal variation and climate change as a level-2 data user.

Considering that clouds often cover the East Japan Sea and the Yellow Sea and the days with clouds or fog are increasing due to the growth of microdust, unless the abnormal SPM values are completely masked, clouds are the critical error source in composite and climatology data. The isolated speckle, which was inferred to be due to the movement of small cloud fractions, is abundant. Its movement during scanning might cause an error in the exact cloud detection. The patch-type speckle and speckles at the bottom of the slot are an annual phenomenon and must be removed from the SPM data. We expect this study to enhance the accuracy and quality of the GOCI SPM data, results of the composited data, and long-term trends.

References

Ahn, J.H., Park, Y.J., Ryu, J.H., and Lee, B., 2012. Development of atmospheric correction algorithm for Geostationary Ocean Color Imager (GOCI). *Ocean Science Journal*, 47(3), 247-259.

Ackerman, S.A., Strabala, K.I., Menzel, W.P., Frey, R.A., Moeller, C.C., and Gumley, L.E., 1998. Discriminating clear sky from clouds with MODIS. *Journal of Geophysical Research*, 103(D24), 32-141.

Binding, C.E., Bowers, D.G., and Mitchelson-Jacob, E.G., 2003. An algorithm for the retrieval of suspended sediment concentrations in the Irish Sea from SeaWiFS ocean colour satellite imagery. *International Journal of Remote Sensing*, 24(19), 3791-3806. doi: 10.1080/0143116021000024131.

Chae, H.J., and Park, K.-A., 2009. Characteristics of speckle errors of SeaWiFS chlorophyll-a concentration in the East Sea. *The Korean Earth Science Society*, 30, 234-246.

Chen, Z., Hu, C., Muller-Karger, F.E., and Luther, M.E., 2010. Short-term variability of suspended sediment and phytoplankton in Tampa Bay, Florida: observations from a coastal oceanographic tower and ocean color satellites. *Estuarine, Coastal and Shelf Science*, 89, 62-72.

Clark, D.K., Baker, E.T., and Strong, A.E., 1980. Upwelled spectral radiance distribution in relation to the particulate matter in sea water. *Boundary Layer Meteorology*, 18, 286-298.

Clark, D.K., Gordon, H.R., Voss, K.J., Ge, Y., Broenkow, W., and Trees, C., 1997. Validation of atmospheric correction over the oceans. *Journal of Geophysical Research*, 102, 17209-17.

D' Sa, E.J., Miller, R.L., and McKee, B.A., 2007. Suspended particulate matter dynamics in coastal waters from ocean color: application to the northern Gulf of Mexico. *Geophysical Research Letter*, 34, L23611. doi:10.1029/2007GL031192.

Doerffer, R., and Schiller, H., 1997. Pigment index, sediment and

gelbstoff retrieval from directional water leaving radiance reflectance using inverse modelling technique. PO-TN-MEL-GS-0005, GKSS Research Centre, Geesthacht, Germany.

Findlay, S., Pace, M.L., Lints, D., Cole, J.J., Caraco, N.F., and Peierls, B., 1991. Weak coupling of bacterial and algal production in a heterotrophic ecosystem: the Hudson River estuary. *Limnology and Oceanography*, 36, 268-278.

Frey, R.A., Ackerman, S.A., Liu, Y., Strabala, K.I., Zhang, H., Key, J.R., and Wang, X., 2008. Cloud detection with MODIS. Part I: improvements in the MODIS cloud mask for collection 5. *Journal of Atmospheric and Oceanic Technology*, 25(7), 1057-1072.

Frouin, R., Schwindling, M., and Deschamps, P.-Y., 1996. Spectral reflectance of sea foam in the visible and near infrared: In-situ measurements and remote sensing implications. *Journal of Geophysical Research*, 101, 14361-14371.

Gordon, H.R., Clark, D.K., Brown, J.W., Brown, O.B., Evans, R.H., and Broenkow, W.W., 1983. Phytoplankton pigment concentrations in the Middle Atlantic Bright: comparison of ship determinations and CZCS estimates. Applied Optics, 22, 20-36.

Martin, J.M., and Maybeck, M., 1979. Elemental mass-balance of material carried by major world rivers. *Marine Chemistry*, 7, 173-206.

Miller, R.L., and McKee, B.A., 2004. Using MODIS Terra 250 m imagery to map concentrations of suspended matter in coastal waters, *Remote Sensing of Environment*, 93, 259-266.

Park, K.-A., Park, J.-E., Lee, M.-S., and Kang, C.-K., 2012. Comparison of composite methods of satellite chlorophyll-a concentration data in the East Sea. *Korean Journal of Remote Sensing*, 28(6), 635-651. doi.org/10.7780/kjrs.2012.28.6.4.

Park, K.-A., Chae, H.-J., and Park, J.-E., 2013. Characteristics of satellite chlorophyll-a concentration speckles and a removal method in a composite process in the East/Japan Sea. *International Journal of Remote Sensing*, 34(13), 4610-4635.

Robinson, I.S., 2004. Measuring the oceans from space: the principles and methods of satellite oceanography, Springer-Praxis, Chichester, UK, 670 pp.

Ruddick, K., Lacroix, G., Park, Y., Rousseau, V., De Cauwer, V., Debruyn, W., and Sterckx, S., 2003. Overview of ocean colour: theoretical background, sensors and applicability for the detection and monitoring of harmful algae blooms (capabilities and limitations). *In Proceedings of the UNESCO monographs on oceanographic methodology series, manual on harmful marine. Microalgae*.

Ruddick, K., De Cauwer, V., Park, Y., and Moore, G., 2006. Seaborne measurements of near infrared water-leaving reflectance: the similarity spectrum for turbid waters. *Limnology and Oceanography*, 51(2), 1167-1179.

Ryu, J.H., Choi, J.K., Eom, J., and Ahn, J.H., 2011. Temporal and daily variation in the Korean coastal waters by using Geostationary Ocean Color Imager. *Journal of Coastal Research*, 64, 1731-1735.

Shettle, E.P., and Fenn, R.W., 1979. Models for the aerosols of the lower atmosphere and the effects of humidity variations on their optical properties. *Environmental Research Papers*, 676, 1-100.

Siswanto, E., Tang, J., Yamaguchi, H., Yuhwan, A., Ishizaka, J., Yoo, S., Sangwoo, K., Kiyomoto, Y., Yamada, K., Chiang, and C., Kawamura, H., Empirical ocean-color algorithms to retrieve chlorophyll-a, total suspended matter, and colored dissolved organic matter absorption coefficient in the Yellow and East China Seas. Journal of Oceanography. 2011, 67, 627–650.

Sturm, B., 1983. Selected topics of Coastal Zone Colour Scanner (CZCS) data evaluation. In A.P. Cracknell (Ed.), Remote sensing applications in marine in marine science and technology (pp. 137-176). Springer Netherlands.

Tassan, S., 1994. Local algorithms using SeaWiFS data for the retrieval of phytoplankton pigments, suspended sediments and

yellow substance in coastal waters. *Applied Optics*, 33, 2369-2378.

Wang, M., and Gordon, H.R., 1994. A simple, moderately accurate, atmospheric correction algorithm for SeaWiFS. *Remote Sensing of Environment*, 50(3), 231-239.

Kim, W., Ahn, J.H., and Park, Y.J., 2015. Correction of stray light driven inter Slot Radiometric Discrepancy (ISRD) present in radiometric products of Geostationary Ocean Color Imager(GOCI). *IEEE Transactions on Geoscience and Remote Sensing*, 53(10), 5458-5472.

PART III. Red Tide

Chapter 1. Introduction

1.1. Previous Research

A "red tide" is one of the most severe disasters that can occur in a marine ecosystem. It is caused by the extreme bloom of certain microalgae, like dinoflagellates, diatoms, and blue-green algae, under particular circumstances including warm sea water temperatures, changes in salinity and nutrient condition, and a stable sea column. Red tide blooms affect fish in two main ways: chemically and physically. Toxic species contaminate water with chemical toxins, but non-toxic species attach themselves to the gills of fish, or exhaust the oxygen supply in water, resulting in suffocation of fish. In the sea surrounding Korea, *Cochlodinium polykrikoides*, a species of dinoflagellate, has bloomed. *C. polykrikoides* is a non-toxic species found in the oceans surrounding East Asia and North America. It was assumed that red tides had not occurred since 2008 due to the absence of red tide blooms from 2008 to 2011. However, an unprecedented extreme red tide bloom occurred in 2013, resulting in damage to the fishery industry worth 23 million US dollars (Fig. 1). After 2013, red tides occurred in the subsequent two years, but in 2016 no red tide was observed. The red tide bloom needs to be monitored continuously, which can be undertaken by satellite data that can observe a wide area of the ocean continuously.

Many researchers have investigated the biochemical and physical sources of red tide blooms. In the period before a red tide, diatoms occupy the seas, and they bloom when there is a high density of nutrients. Diatoms prefer silicates and nitrogen, which are lacking in offshore habitats and are supplied from surface runoff or from the bottom of oceans. Generally, in surface runoff silicate is present in higher concentrations than nitrogen. Although the diatoms are photosynthetic in appropriate conditions, a ratio of Si:N:P = 16:16:1 promotes dinoflagellates, especially *C. polykrikoides*, to be mixotrophic, combining photosynthesis with ingestion of prey. *C. polykrikoides* grows faster when the ratio of nitrogen to phosphate is 10:1 or 5:1 than when it is 15:1 (Tomas and Smayda, 2008). This species is stronger than other diatoms in low nutrient conditions. *Cochlodinium* spp. have active mobility; prey is stabbed by diatoms that have a needle-like shape, and cells are exploded. The seas surrounding Korea are affected by low salinity levels due to an influx of water from Changjiang River during summer. Water at the river mouth has a high density of nutrients in June. As the water flows eastward, to the South Sea of Korea, diatoms bloom and ingest nutrients with the ratio of Si:N:P = 16:16:1. This results in depletion of N in the water, eventually leading to a low N:P ratio when the water arrives in the South Sea. These conditions are advantageous to *Cochlodinium* spp., which will bloom.

Physically, the most potent factor affecting red tide blooms is high sea water temperatures (21-31 ℃). The simultaneous appearance of

cold water induces water column stability and the red tide can grow well. Sufficient nutrients and the ratio of nutrient ingredients are also important factors affecting species dominance. The source of nutrient supply was revealed to be upwelling induced by wind. Park et al. (2001) measured the in-situ temporal variability of red tide density by depth in Gwangyang Bay in September 1996. Kim et al. (2006) and Lee et al. (2010) researched the relationship between submarine groundwater and red tide as a nutrient supply in the southern sea of Korea. Kim et al. (2004) studied the effects of temperature, salinity, and irradiance on the growth of the harmful red tide dinoflagellate *C. polykrikoides* Margalef (Dinophyceae). Gobler et al. (2008) elucidated the characterization, dynamics, and ecological impacts of harmful *C. polykrikoides* blooms on eastern Long Island, NY, USA during 2002-2006. Blooms appeared when the temperature ranged between 20℃ and 25℃ and salinity was 22-30 ppt. The rDNA of the *C. polykrikoides* bloom showed 88-90% similarity to *C. polykrikoides* from Southeast Asia. There have been various attempts to detect red tide features using satellite data.

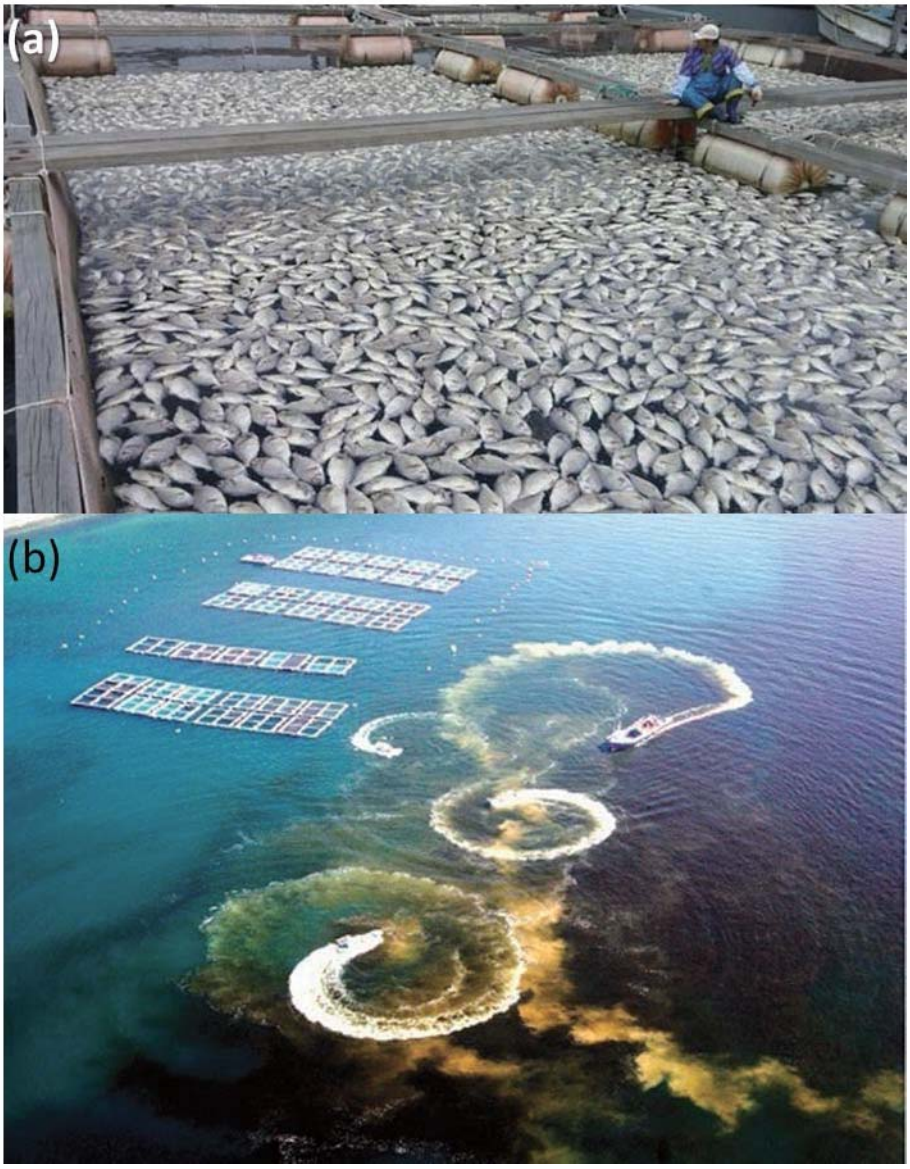

Fig. 1. Images of red tide disasters, (a) fishery industry damaged by red tide, (b) disaster recovery work spreading yellow soils on red tide bloom seawater (provided by NIFS).

1.2. Satellite Application to Red Tide Detection

Various kinds of red tide indices have been developed for optical satellite data for various oceans and certain species (Table 1). Gower (1994) suggested an algorithm for detection of coccolithophores on the west coast of Canada using 640 nm and 860 nm from AVHRR HRPT. Many researchers have used SeaWiFS chlorophyll-a (Chl-a) concentration data to support descriptions of red tide distribution (Tang et al., 2006; Ishizaka et al., 2006; Wei et al., 2008). The red tide index for SeaWiFS utilizes 443 nm, 510 nm, and 555 nm channels for multiple red tide species in the Northwest Pacific (Ahn et al., 2006; Shanmugam et al, 2008). MODIS has also been utilized to detect *C. polykrikoides* around Korea using 488 nm and 551 nm channels (Kim et al., 2009). Fluorescence line height (FLH) between 660 nm and 880 nm channels has been used to discriminate *Karenia brevis* in west Florida using MODIS (Amin et al., 2009) and in the North Sea, Southern Africa, and Lake Erie using MERIS (Gower et al., 1999; Matthews et al., 2012; Binding et al., 2012). The ratio of difference among three visible channels of the geostationary ocean color imager (GOCI) was applied to detect *Prorocentrum donghaiense* in the East China Sea (Lou and Hu, 2014).

Table 1. Summary of the equations for red tide detection from satellite observations in previous studies.

Satellite	Wavelength (nm)	Algorithm	Location	Species	Author
SeaWiFS	443 510 555	$RI=\frac{\frac{Lw510}{Lw555}-Lw443}{\frac{Lw510}{Lw555}+Lw443}$ $RI=10^{-0.1069X^3+0.6259X^2-1.3936X+0.919}$	North West Pacific	various kinds	Shanmugam et al. (2008)
MODIS	488 551	SST >25°C $MRI=\frac{nLw551-nLw488}{nLw551+nLw488}>0$	Korean Shelf	Cochlodinium polykrikoides	Kim et al. (2009)
	667 678 748	$FLH=L_{678}-L_{667}-(L_{748}-L_{667})\frac{(678-667)}{(748-667)}$	West Florida Shelf	Karenia brevis	Cannizzaro et al. (2008)
MERIS	665 682 705	$FLH=L_{682}-L_{665}-(L_{705}-L_{665})\frac{(682-665)}{(705-665)}$	North Sea	-	Gower et al. (1999)
	665 681 709 753 885	$MPH=L_{max}-L_{665}-(L_{885}-L_{665})\frac{(\lambda_{max}-665)}{(885-665)}$	Southern Africa	Microcystis aeruginosa	Matthews et al. (2012)
	681 709 753	$MCI=L_{709}-L_{681}-(L_{753}-L_{681})\frac{(709-681)}{(753-681)}$	Lake Erie	Diatom Aulacoseira	Binding et al. (2012)
GOCI	443 490 555	$RI=\frac{R_{rs}555-R_{rs}443}{R_{rs}490-R_{rs}443}>4.0$	East China Sea	Prorocentrum donghaiense	Lou and Hu (2014)

1.3. Study Objectives

Previous studies have elucidated how red tides bloom and have developed algorithms for certain satellite images or for specific events. It is difficult to apply previous algorithms to other case studies. As circumstances vary annually, a mechanism that explains a bloom in the past cannot explain all events. In particular, an abnormally extreme red tide bloom appeared in 2013 around Korea. Many scientists tried to find its cause using Chl-a concentration and sea surface temperature data (Choi et al., 2014; Kim et al., 2016). Thus far, there has been no research clarifying the long-term spatiotemporal variability of red tide blooms. We collected in-situ red tide density data and environmental data over 11 years from 2006 and made a relational database to reveal the relationship between red tide blooms and oceanic factors.

The objectives of this study are 1) to confirm the applicability of previous red tide detection methods to new circumstances, 2) to develop a red tide detection method based on in-situ spectral measurements, 3) to elucidate the spatiotemporal variability of red tides around Korea, and 4) to suggest a relationship between red tide blooms and oceanic factors.

Chapter 2. Data

2.1. Satellite Data

GOCI, on board the Communication, Ocean, and Meteorological Satellite (COMS), was launched in June 2010 by the KARI. It is an ocean color sensor that observes the seas around the Korean peninsula (24.75–47.25°N, 113.4–146.6°E) eight times a day from 0000 UT to 0700 UT (KST 9AM to 4PM) with a 500 m × 500 m spatial resolution. A whole GOCI image is obtained by a 16-slot step and stare scanning method. It has six visible (412, 443, 490, 555, 660, and 680 nm) and two near-infrared (NIR; 745 and 865 nm) channels with a 20 nm bandwidth. GOCI level-2 remote sensing reflectance (R_{rs}) data were obtained from the KOSC for the period of 2011–2016. As GOCI level-2 data requires atmospheric correction, reprocessed R_{rs} data were utilized to detect red tide blooms. The procedure is outlined in Part III.

2.2. In-Situ Optical Measurement

We conducted fieldwork near the coastal region around Korea from 2009 to 2016. The density of red tides and their R_{rs} values were collected through field observations when extreme red tides occurred in the South Sea on August 8 in 2013 and August 13 in 2015. We measured surface reflectances for red tide blooms using a wide spectrum spectroradiometer from 350 nm to 1050 nm, and sampled a bottle of sea water at each station. Major red tide species were identified, and the density of each species and Chl-a concentrations were measured in a laboratory (Fig. 2). The observation dates from 2009 to 2016 are summarized in Table 2. In seawater where red tides occurred, there are two distinct reflectance peaks at 555 nm and 680 nm (Fig. 3).

Table 2. Cruise dates for *in situ* measurements presented in this study

	1	2	3	4	5	6	7	8	9	10	11	12
2009									9/22		11/25	
2010							7/7					
2011												
2012							7/23- 7/26			10/9- 10/10		12/3
2013	1/8	2/21	3/9 3/25	4/10 4/26	5/12 5/30- 5/31			8/8		10/27	11/12	
2014	1/15	2/4 2/16						8/11				
2015		2/25			5/8			8/13				
2016						6/30					11/18	

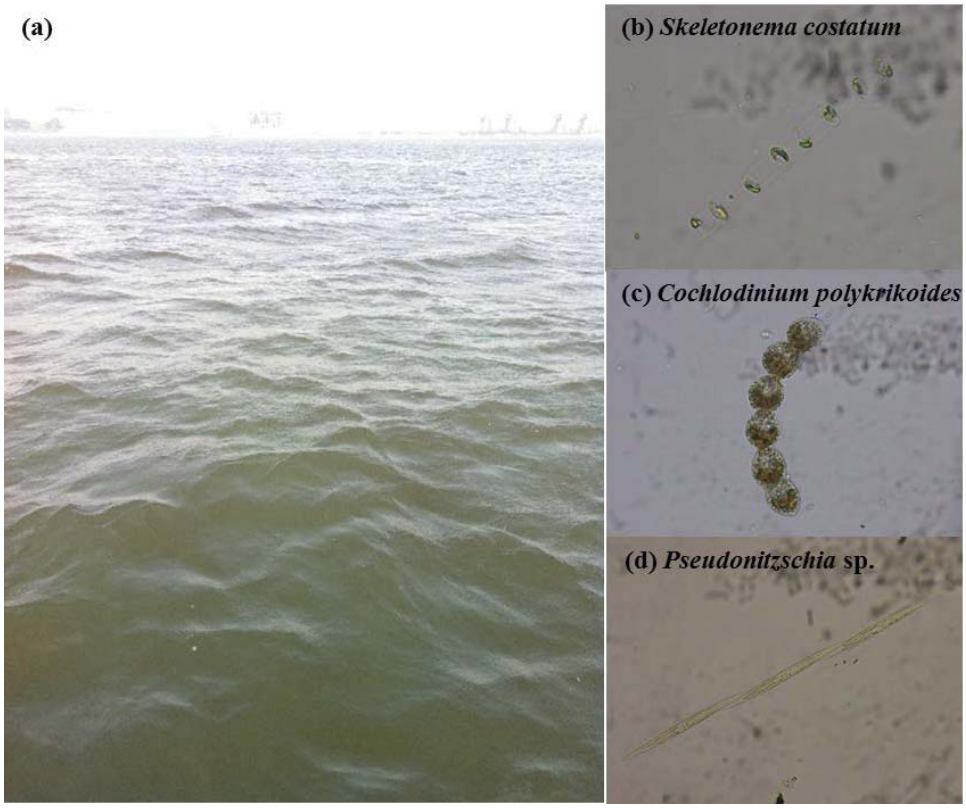

Fig. 2. Images of red tide, (a) seawater with high-density red tide and observed red tide species: (b) *Skeletonema costatum*, (c) *Cochlodinium polykrikoides*, (d) *Pseudonitzschia* species in Gwangyang Bay on August 8, 2013.

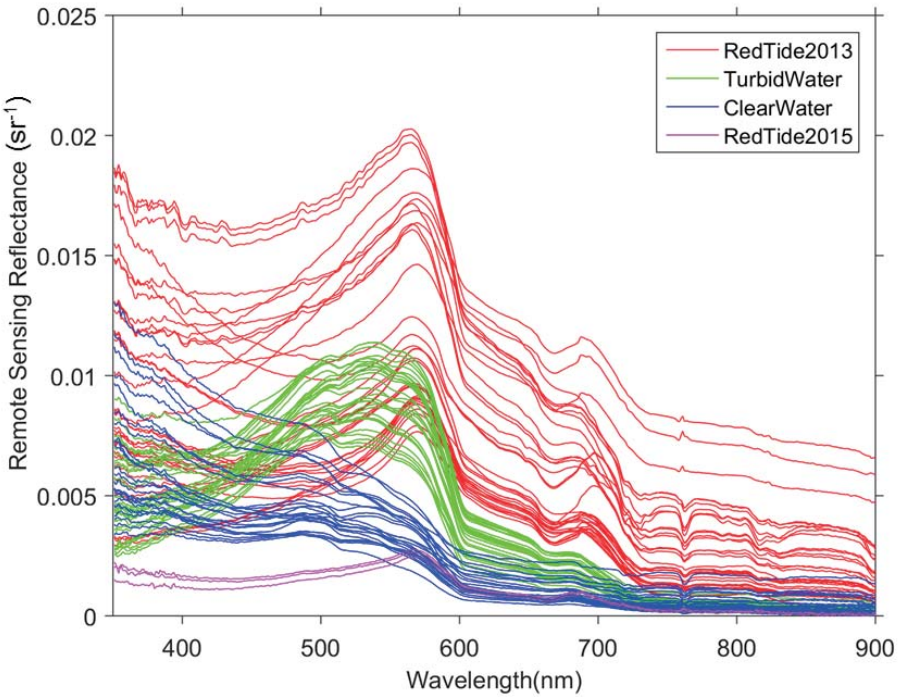

Fig. 3. Variable *in situ* spectral R_{rs} with and without red tide. Red and magenta colored lines indicate R_{rs} when red tide bloomed in Gwangyang Bay in 2013 and 2015, respectively. Blue and green lines indicate clear water in the East Sea and turbid water in Gwangyang Bay without the red tide bloom.

2.3. In-Situ Red Tide Observation

Since 2006, the National Institute of Fisheries Science (NIFS) has provided daily red tide distribution maps, location names, in-situ red tide density (minimum/maximum, cells/mL), sea water temperature (high/low, ℃), and major red tide species on their website when red tides occur. Although NIFS give the specific location where data have been sampled as an oval shape on a map, only a few in-situ red tide densities are reported on their website as representative values over the adjacent area.

The frequency of red tide occurrence from 2006 to 2016 is shown in Fig. 4. Red tides were mainly observed on the southern and eastern coasts, and the frequency of occurrence was higher on the former. Red tides occurred for more than 100 days on the southern coast between 34.5–35° N and 127.5–129.0° E. On Namhae, Tongyoung, and Geoje coasts, in the last 11 years red tides occurred on a total of 199, 233, and 180 days, respectively.

The maximum red tide concentration distribution from 2006 to 2016 shows that it is common to have a high concentration of red tides occurring on the southern coast near 128.5° E, but that the density and time of the red tide changes every year (Fig. 5).

Based on these NIFS red tide observations, the red tide density of the entire Korean Peninsula over 11 years varied annually as shown in Fig. 6a. The red tide, which appeared mainly from late July to early August, disappeared in autumn. However, in 2009 a red tide occurred

from late October to early November. In addition, in 2013, a red tide bloom started in early June, earlier than in other years. Red tides occurred every year from 2006 to 2010 but did not appear in 2011. After 2011, red tide blooms became severe and showed an increasing tendency compared to the previous five years (Fig. 6b).

The duration of red tides also increased with time (Fig. 6c). Red tides started in August and showed durations of under 30 days between 2006 and 2010. However, the average duration between 2012 and 2016 was around 55 days. In 2014 the duration was 86 days (Fig. 6c).

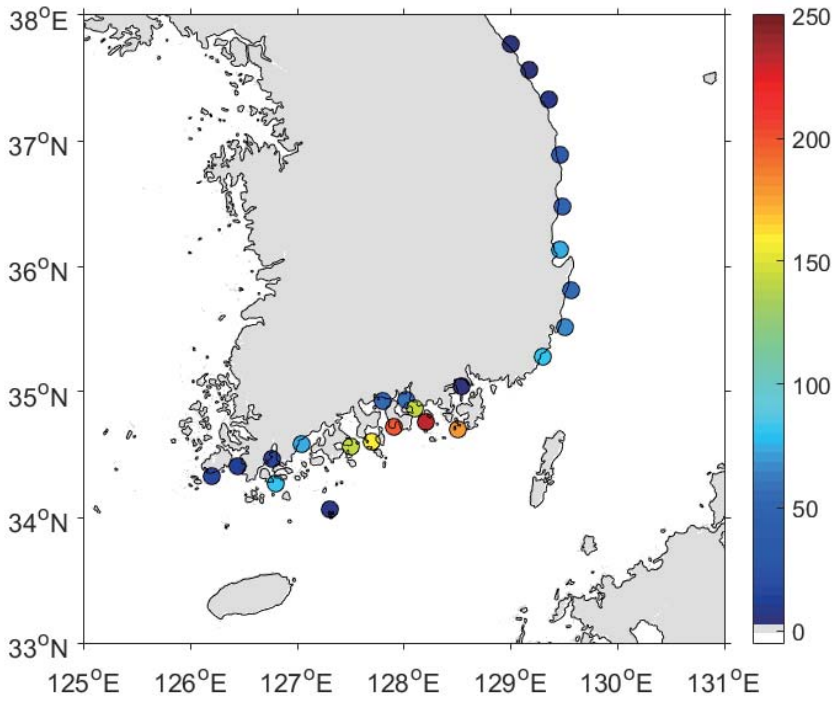

Fig. 4. Frequency of red tide bloom in the period 2006-2016. Colors represent number of days red tide was observed.

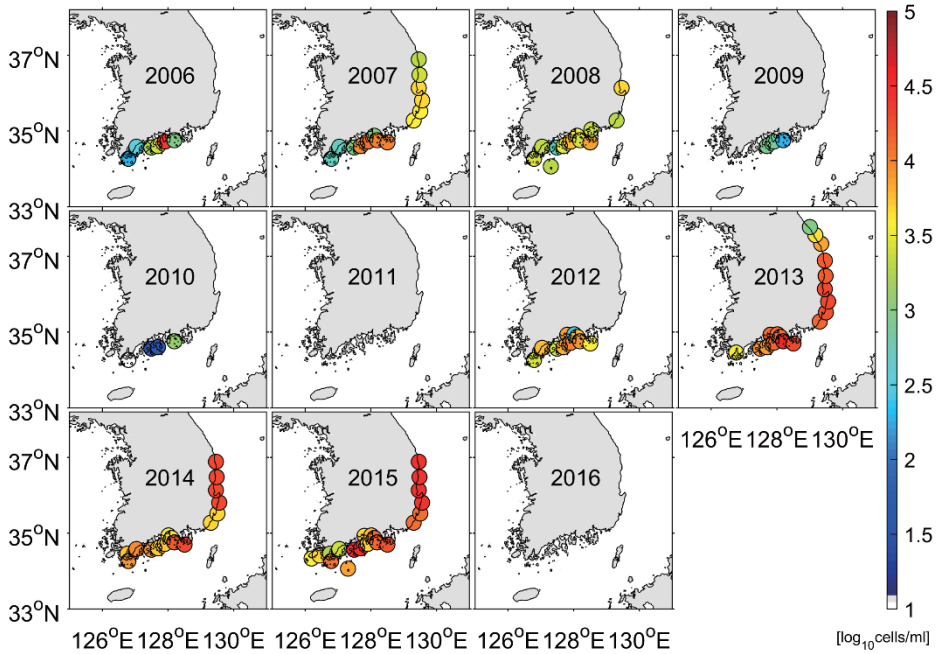

Fig. 5. Year-to-year variations in maximum *in situ* red tide density from 2006 to 2016. Colors represent red tide density (cells/ml).

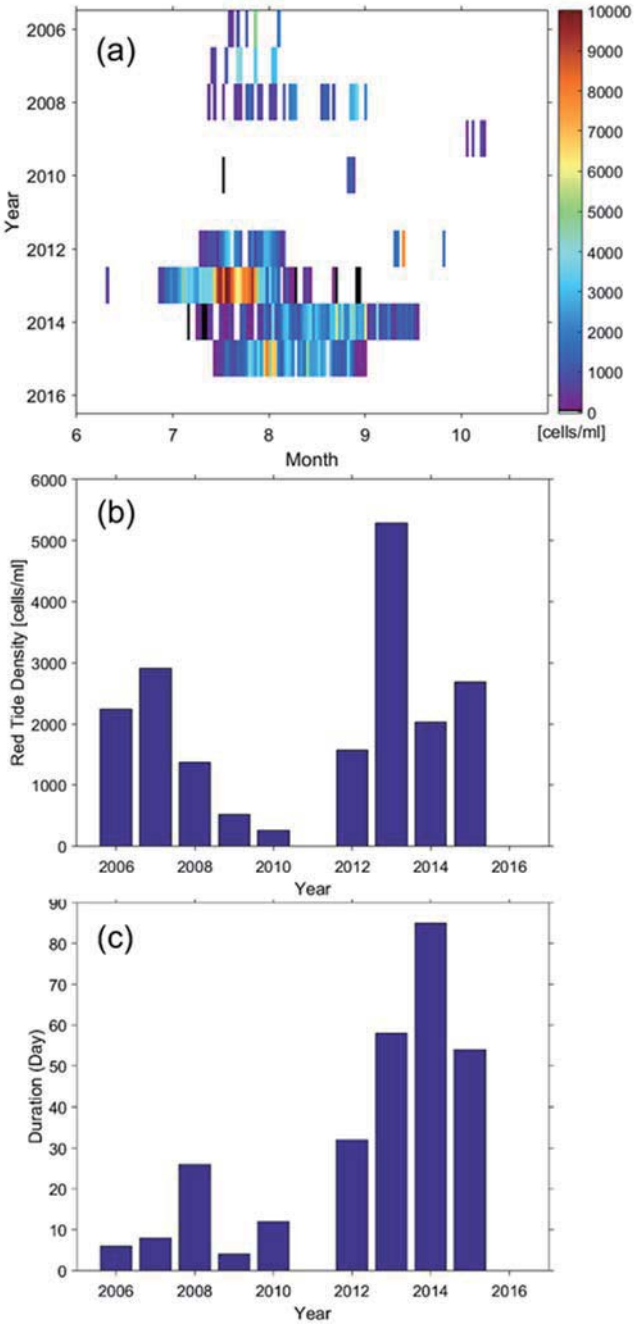

Fig. 6. (a) Year to month red tide density (log_{10}cells/ml), (b) yearly mean of red tide density, (c) duration (day) of red tide bloom during each year from 2006 to 2016.

2.4. Wind Data

Wind is thought to be one of the most important factors that triggers red tide blooms. Wind-induced vertical mixing and wind-driven current can suppress or propagate red tide blooms. The European Centre for Medium-Range Weather Forecasts (ECMWF) provides a 6-hour term wind field with a spatial resolution of 0.125 degrees. We utilized wind field data to find the effect of wind on red tide blooms.

Chapter 3. Methods

3.1. Algorithm Development

Based on the spectrum of collected in-situ spectral measurements, the difference between areas where red tides did and did not occur was very clear. In seawater where red tides occurred, there are two distinct reflectance peaks at 555 nm and 680 nm (Fig. 3). Based on these differences, a red tide index algorithm using two peaks was devised. As an FLH method, the height of each peak was calculated and a normalization process was added with $R_{rs}(490)$ and $R_{rs}(660)$ (Fig. 7).

$$\mathrm{P555} = R_{rs}555 - \left(R_{rs}660 + \frac{660-555}{660-490} \times (R_{rs}490 - R_{rs}660)\right) \quad (1)$$

$$\mathrm{P680} = R_{rs}680 - \left(R_{rs}745 + \frac{745-680}{745-660} \times (R_{rs}660 - R_{rs}745)\right) \quad (2)$$

The red tide index (RTI) algorithm must be applied to GOCI data with care. Suspended particulate matter (SPM), Chl-a, and colored dissolved organic carbon (CDOM) were measured prior to calculating RTI, and their relationship with RTI was revealed. Pixels with negative peak height can be discriminated as red tide-free areas. In very clear water with low SPM concentration, $R_{rs}(660)$ shows under 0.001 sr^{-1}, which can result in a second peak at 680nm amplifying

after normalization. If there are two peaks in a spectrum, whose values are over the threshold, a pixel can be designated as a red tide pixel. A newly designed red tide detection process was applied to the GOCI image.

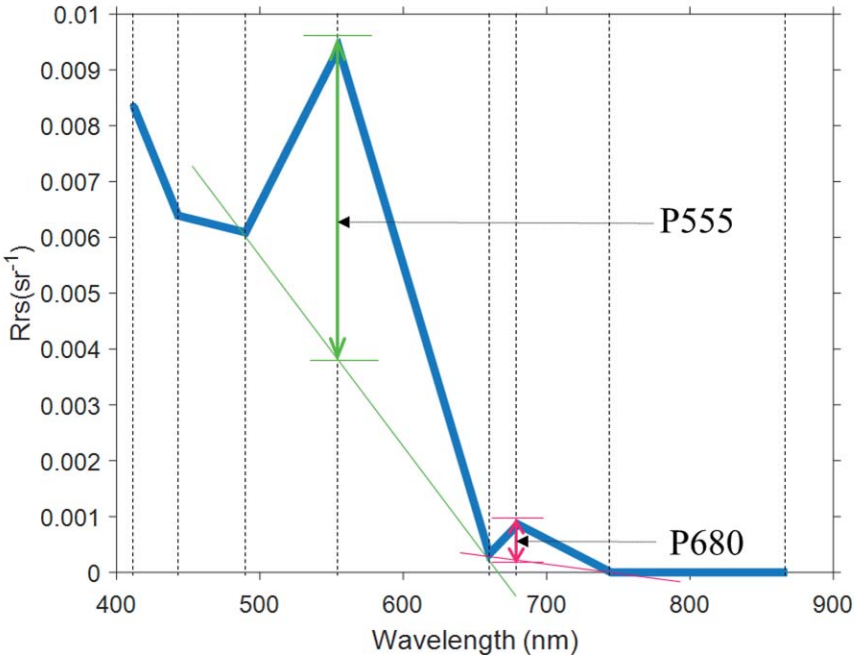

Fig. 7. Typical distribution of R_{rs} as a function of wavelength with two spectral peaks during a red tide bloom.

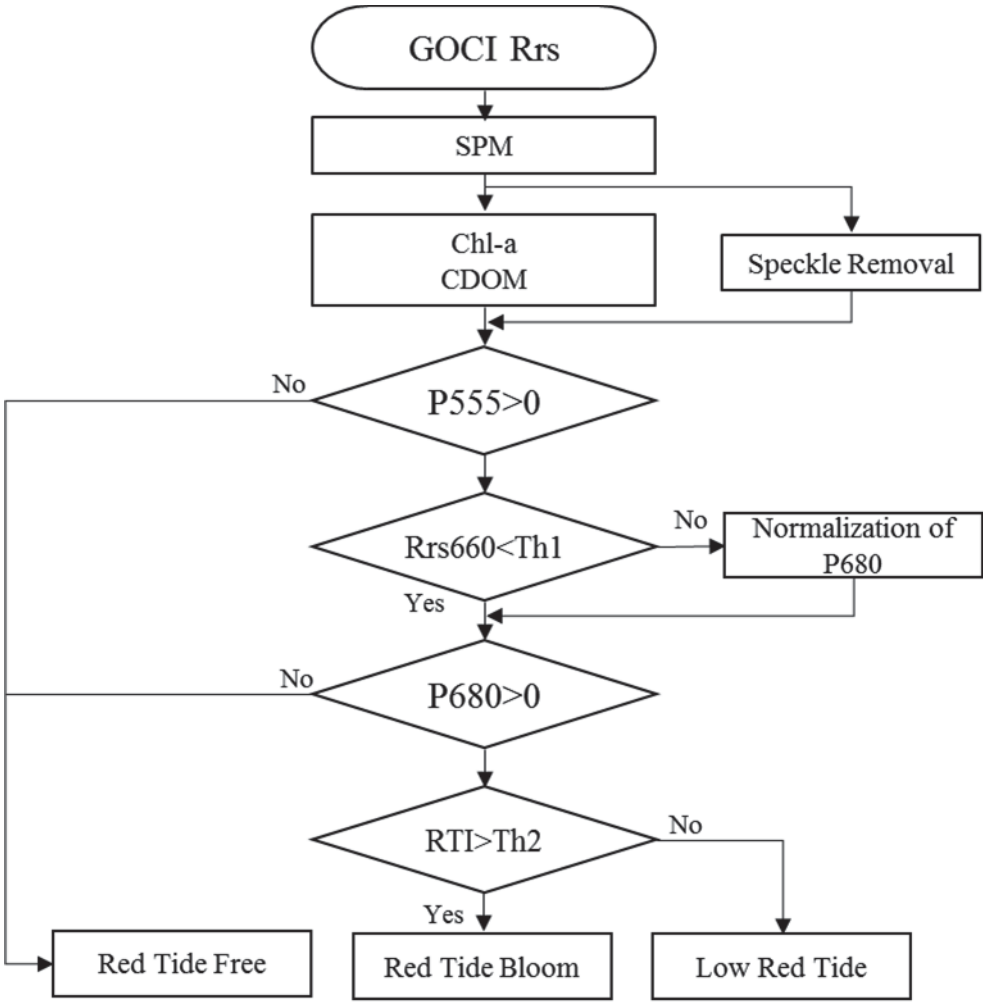

Fig. 8. Flow chart of red tide detection processing used in this study.

3.2. Digitization of Red Tide Report

Fig. 9a shows an example of the red tide density map for August 13, 2013. NIFS provides a red tide occurrence location map and representative in-situ red tide density separately. We geocoded their location map and labelled the regionally representative red tide density value for each region. The density of red tides in the South Sea and the eastern coast ranged from 0-14,000 cells/mL in Fig. 9b. While the southeast sea had a relatively low density of 4000 cells/mL of red tide, a relatively high density close to 14,000 cells/mL appeared on the south coast at 128.5° E. A digitized in-situ red tide map was utilized to validate the result of the newly created RTI.

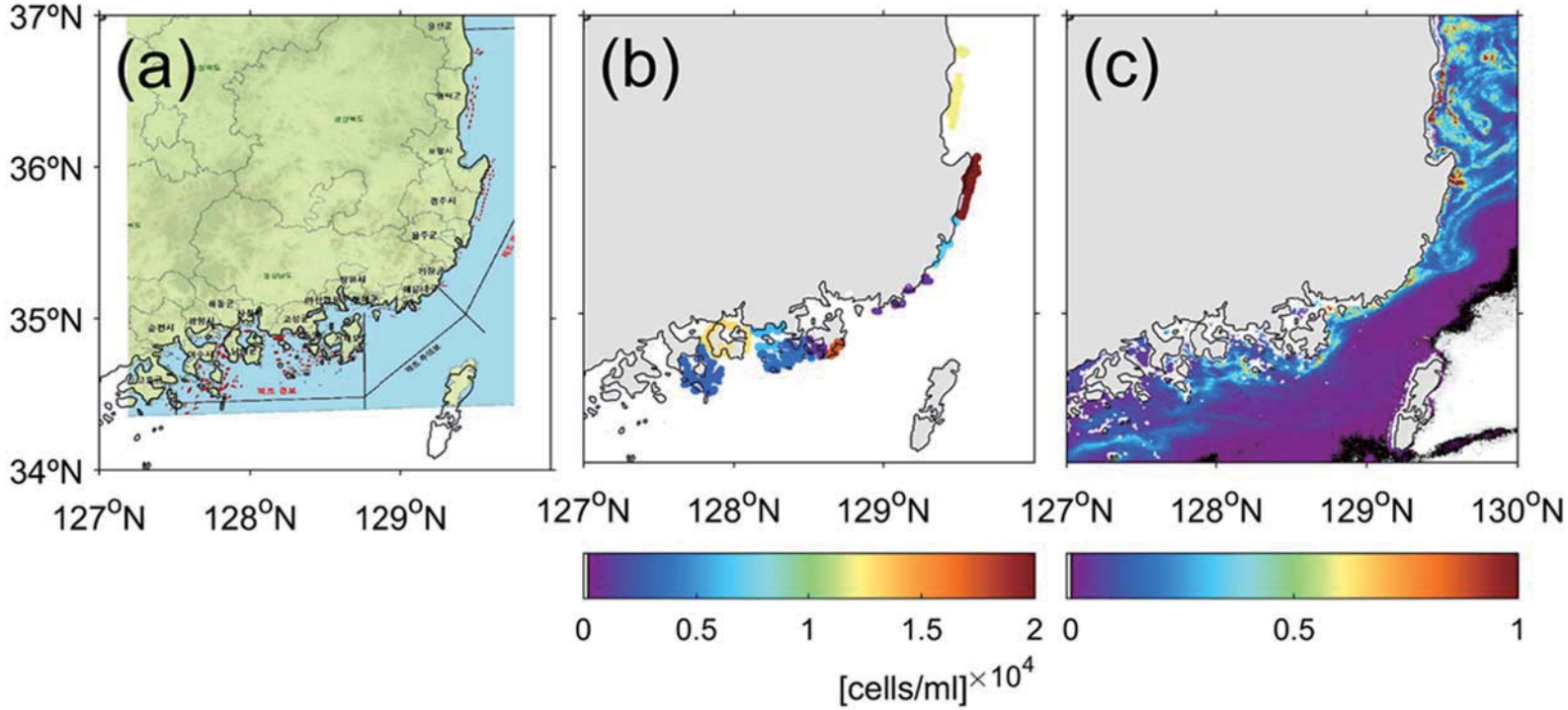

Fig. 9. (a) NFRDI red tide report map, (b) digitized red tide density map, (c) RTI map at the same day (August 13, 2013).

3.3. Relation with Red Tide Index and Red Tide Density

In order to set the threshold of the RTI to determine whether conditions constitute a red tide or not, we compared the results of the newly created RTI applied to a GOCI image to the in-situ red tide density map provided by NIFS for the same day (Fig. 9). Positive RTI represents areas where the spectrum has a peak above the norm. The frequency of RTI values in red tide bloom areas shows a maximum at 0.2 (Fig. 10a).

The relationship between the RTI and in-situ red tide density is shown in Fig. 10b, which can be expressed by (1).

$$RTdensity = 1.005 \times 10^6 \times e^{0.004714 \times RTI} - 1.0 \times 10^6 \quad (3)$$

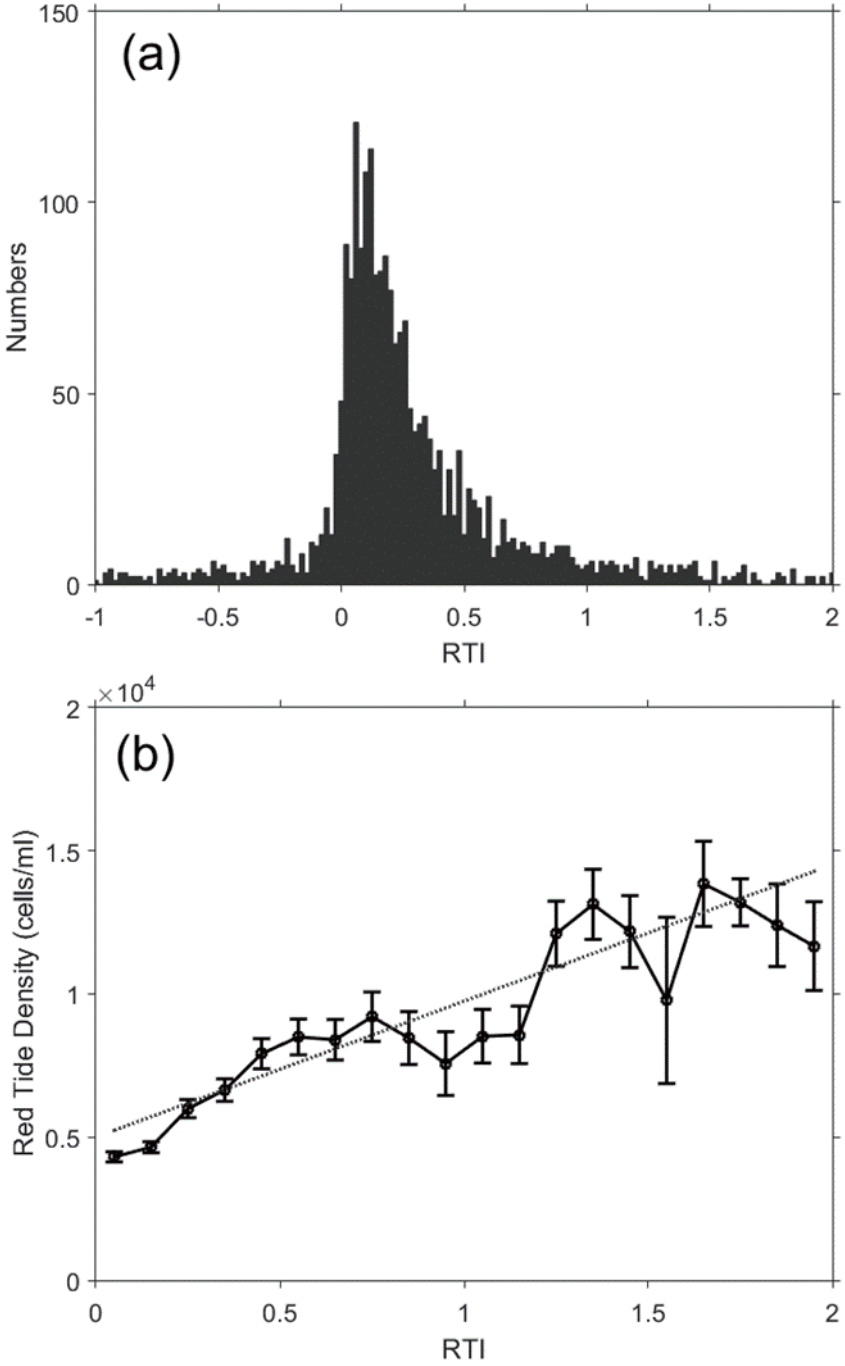

Fig. 10. (a) RTI histogram, (b) variations of in situ red tide density as a function of RTI in the in situ red tide bloom region.

3.4. Algorithms of Ocean Color Parameters

To elucidate the relationships between RTI and SPM, CDOM, and Chl-a, these parameters were also estimated by following algorithms simultaneously using GOCI. Yellow Sea Large Marine Ecosystem Ocean Color Work Group (YOC) has collected the *in-situ* measurements of ocean color parameter in the area where GOCI has observed. They developed and suggested SPM, CDOM and Chl-a concentration algorithm proper to turbid water like seas around Korea (Siswanto et al., 2011). The algorithms are as follows:

SPM

$$SPM = 10^{0.649+25.623*(Rrs555+Rrs660)-0.646*\left(\frac{Rrs490}{Rrs555}\right)} \quad (4)$$

CDOM

$$CDOM_{YOC} = 10^{(-0.99-1.781*log_{10}\mathrm{R}-2.18*log_{10}^{2}\mathrm{R})}$$

$$R = \frac{Rrs490}{Rrs555} * Rrs443^{0.059} \quad (5)$$

Chl-a

$$Chla = 10^{-0.166-2.158*R+9.345*R^2}$$

$$R = log_{10}\frac{Rrs443}{Rrs555}\left(\frac{Rrs412}{Rrs490}\right)^{-0.463} \quad (6)$$

3.5. Cloudiness

As a parameter affecting red tide growth rate, cloudiness is calculated using reprocessed GOCI data with speckle removal. Photosynthetically active radiation (PAR) is a crucial factor for red tide growth. Previous PAR data provided by research centers are coarse in comparison to GOCI RTI data. PAR represents radiation within the range of visible channels, from 400 nm to 700 nm. Visible channels can be obscured by cloud. Therefore, cloudiness can replace PAR, as its reciprocal. GOCI observes the seas around Korea eight times a day, during daylight hours. Using speckle removal processed GOCI level-2 data, the number of times that data cannot be collected due to cloud cover during one day can be calculated. This number ranges from zero to eight; zero means that it was clear throughout the day, and a value of eight represents cloudiness throughout the day.

Chapter 4. Results

4.1. Comparison with Previous RTIs

Various attempts to detect red tides through satellite data are ongoing. Table 1 shows the red tide detection algorithm developed for each sea area for each satellite. For seas around Korea, Ahn and Shanmugam (2006) suggested an exponential red tide index and band ratio RI, Chu and Kuo (2010) used band RI, and Lou and Hu (2014) developed Lou RI. Using each algorithm, the red tide index around the Korean peninsula was calculated using the GOCI image from Aug. 13, 2013 (Fig. 11). The results of the previous RTIs were not suitable; it was difficult to obtain accurate red tide information from these three red tide algorithms. This means that it is necessary to develop a new red tide algorithm for the seas around Korea.

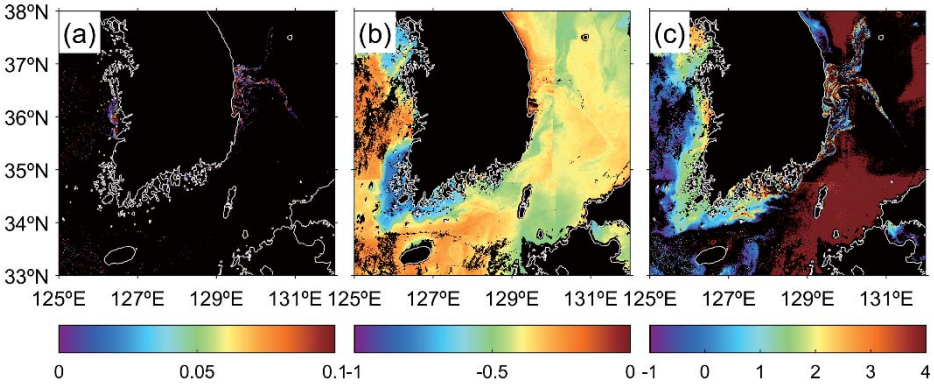

Fig. 11. Spatial distribution of red tide index as a result of applying previous methods to a GOCI image at 03 UT on August 13, 2013: (a) Ahn and Shanmugam (2006), (b) Chu and Kuo (2010), and (c) Lou and Hu (2014).

4.2. Validation of RTI

4.2.1. Relationship with SPM, CDOM, and Chl-a

The frequency of SPM concentration, CDOM absorption rate, and Chl-a concentration show maxima at 2 g/m^3, 0.24, and $10^{0.5}$ mg/m^3, respectively (Figs. 12a-c). RTI decreases as SPM concentration increases. As CDOM and Chl-a increase, RTI increases (Figs. 12d-f). CDOM and Chl-a have a strong positive relationship.

The negative relationship between SPM and RTI is probably because red tides usually occur in coastal regions, which have relatively low SPM concentration. In highly turbid coastal regions, there is strong tidal mixing, which causes cool sea water temperatures and thus inhibits red tide blooms.

The spectral absorption characteristics of CDOM and Chl-a contribute to increasing the RTI (Fig. 13). Absorption of blue-green wavelengths increases the height of the peaks. Absorption and emission of Chl-a at 662 nm and 669 nm causes increases in the second peak. This is a natural phenomenon. CDOM is generated by biological metabolism.

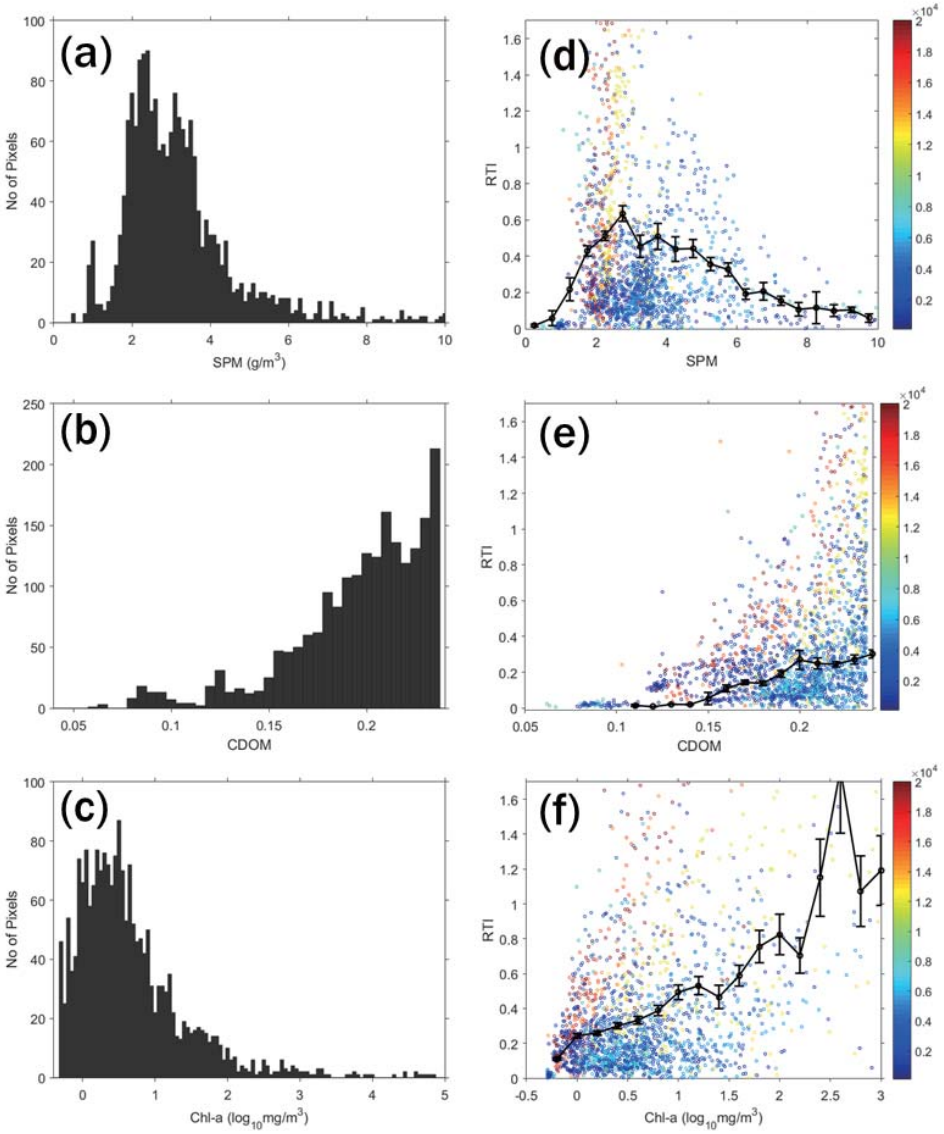

Fig. 12. Histogram of (a) SPM, (b) CDOM (c) Chl-a concentration. RTI variation as a function of (d) SPM, (e) CDOM (f) Chl-a concentration.

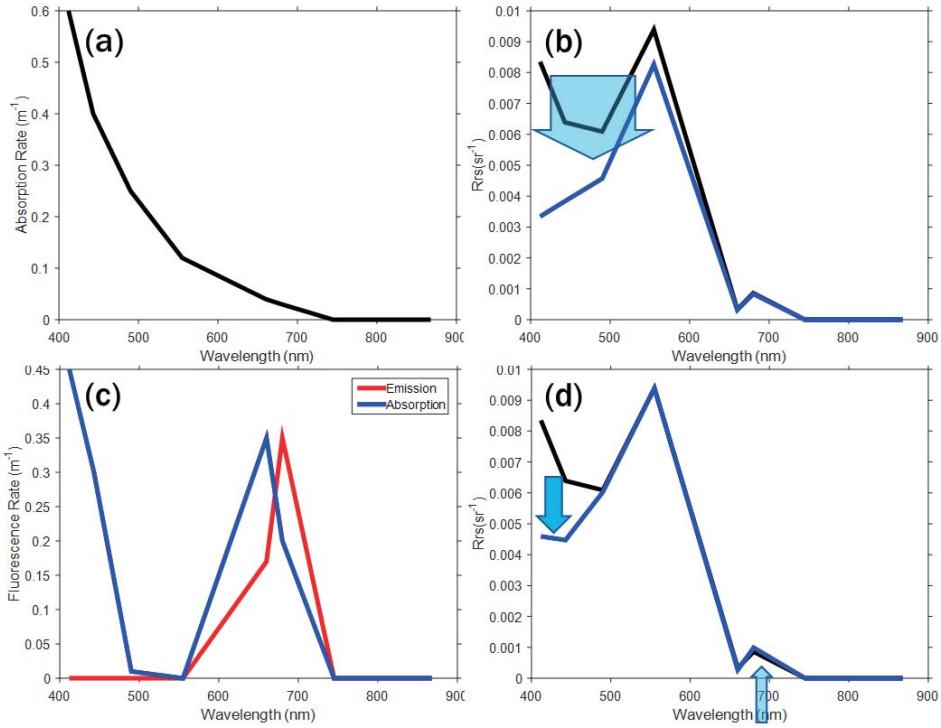

Fig. 13. (a) Absorption rate as a function of wavelength with respect to CDOM, (b) spectral distribution of typical R_{rs} with red tide (black) and CDOM absorption rate applied R_{rs} (blue). (c) Absorption (blue) and emission (red) as functions of wavelength

4.2.2. Diurnal Variation of Red Tide

To assess the diurnal variation of red tides, we selected hourly GOCI satellite images on a clear day without clouds from 9 AM to 4 PM on August 13–15, 2013, and analyzed the temporal–spatial diurnal variation in red tides. Fig. 14 shows the hourly variation of red tides in the study area. Although the distribution of red tides does not vary spatially over time, the value of RTI fluctuated significantly.

The results of spatial averaging of the RTI at red tide bloom locations (RTI > 0.2) at each hour can be seen in Fig. 15; the maximum RTI appeared at 10 AM and 2 PM. The same results appeared on August 14 and 15. To confirm the bimodality of the time of maximum RTI, the red tide bloom region shows constant spatial distribution of maximum RTI during 9 AM–12 PM and 12 PM–4 PM (Fig. 16). Similarly to Fig. 15, Fig. 16 also shows maximum RTI at 10 AM and 2 PM.

Earlier studies have revealed the diurnal variation of red tides using in–situ data. We can identify the bimodal maximum value of the RTI from 11 AM to 2 PM in Fig. 17. These results verify the accuracy of the RTI and its applicability for studying the diurnal variation of red tides from GOCI satellite data.

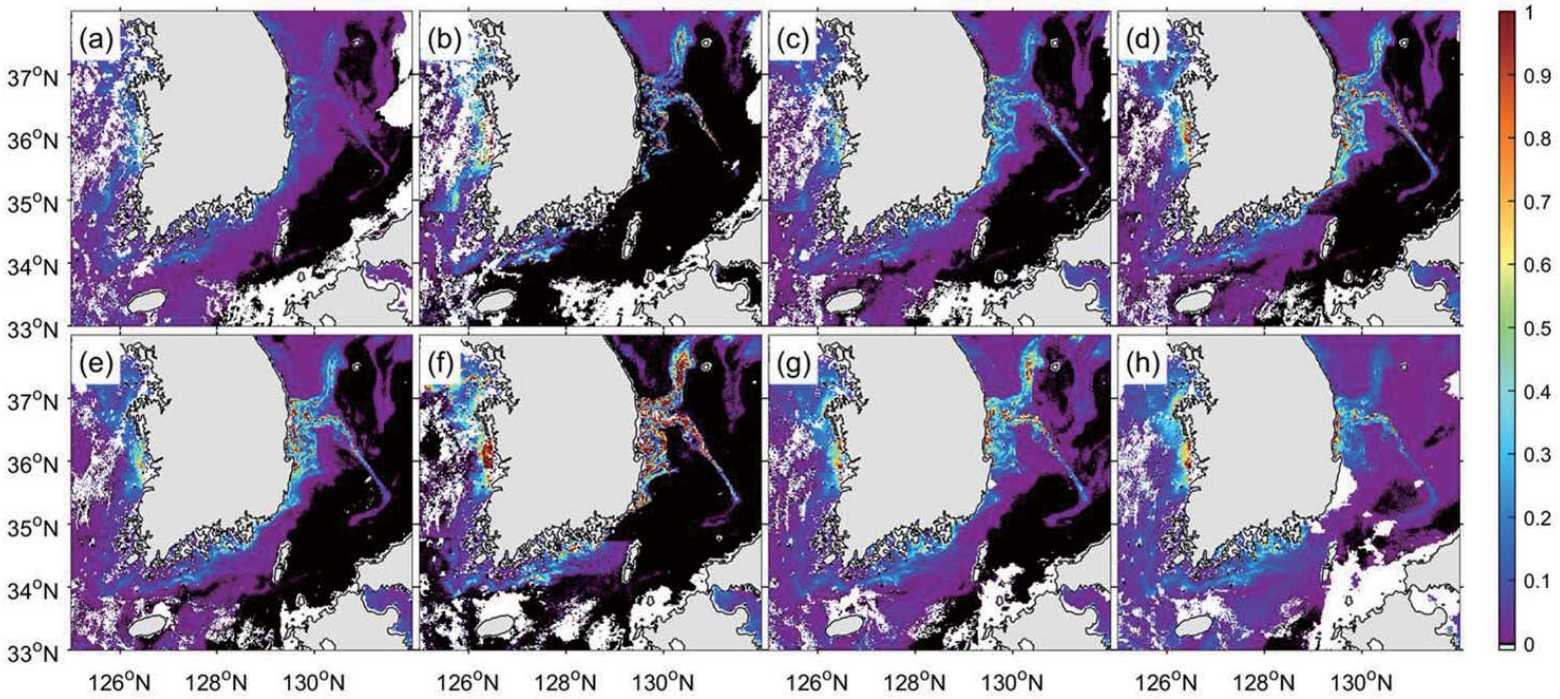

Fig. 14. Hourly spatial distribution of red tide index from 00 UT to 07 UT from GOCI data.

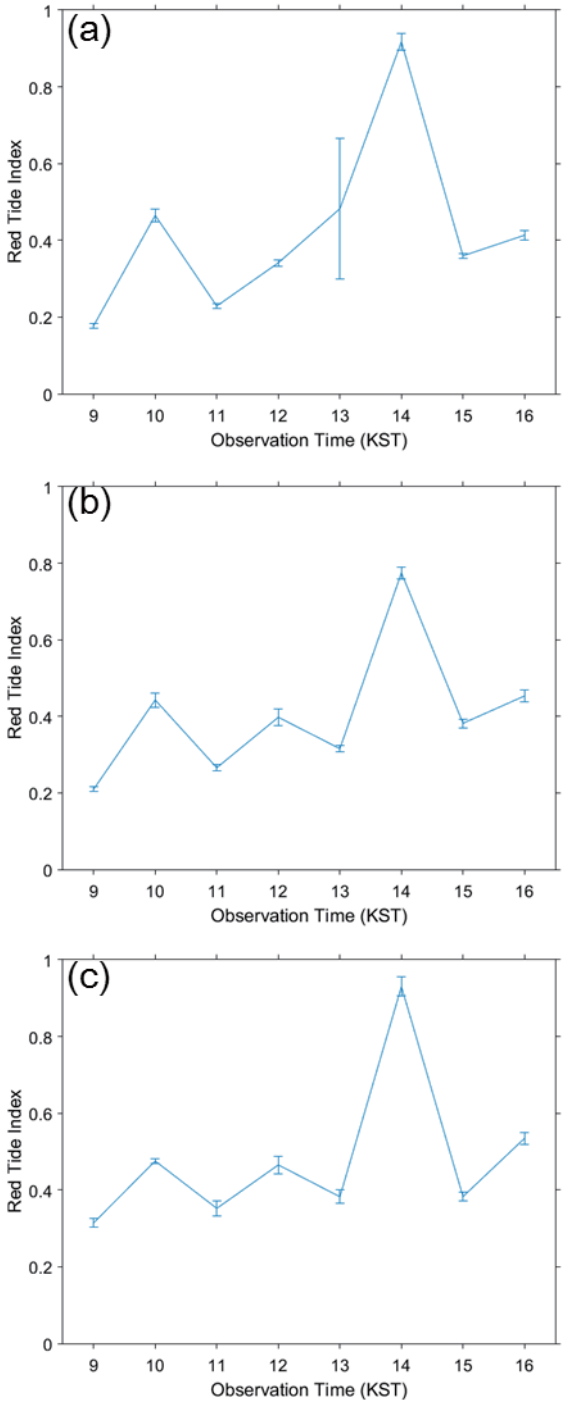

Fig. 15. Hourly variation of satellite RTI on (a) 13, (b) 14, (c) 15 of August, 2013.

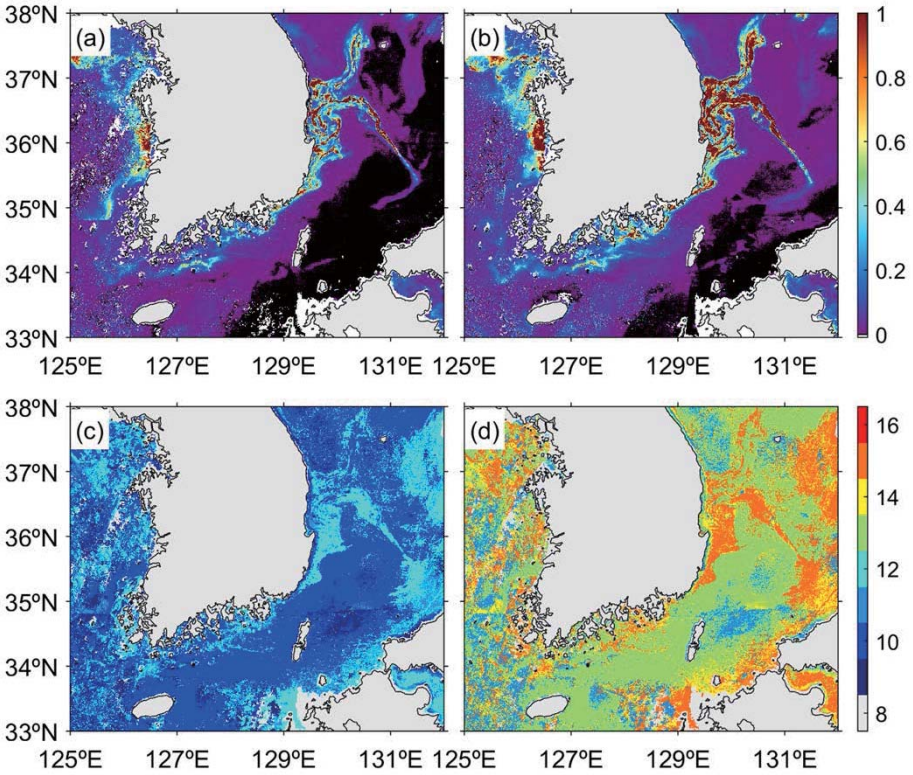

Fig. 16. Maximum RTI (a) from 9 AM to 12 PM, (b) from 12 PM to 4 PM, maximum RTI occurrence times (c) from 9 AM to 12 PM, (d) from 12 PM to 4 PM on August 13, 2013.

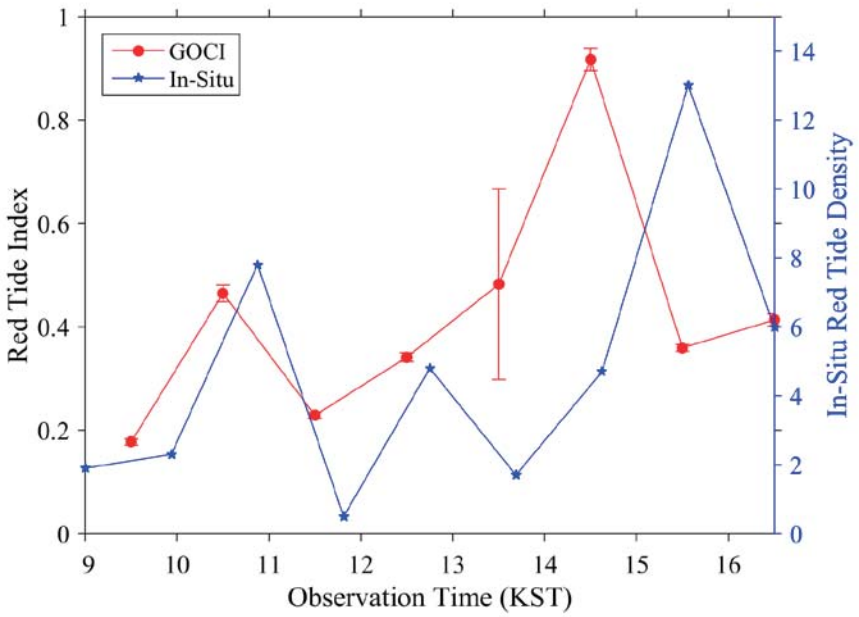

Fig. 17. Temporal variation of In-in situ red tide density measurement (Park et al., 2001)(blue) and satellite RTI (red) by time.

4.3. Fundamental Variability of Red Tides

The mean RTI calculated annually from 2011 to 2016 is shown in Fig. 18. In the Yellow Sea, there is a high mean RTI every year both onshore and offshore. In the South Sea, there is a high mean RTI onshore every year. In the East Sea, there is a high mean RTI onshore every year, and offshore in 2013. In the sea surrounding Jeju Island, there is a much higher mean RTI in 2016 than in other years.

The maximum RTI calculated annually is shown in Fig. 19. In the Yellow Sea, there is a high maximum RTI from 2011 to 2016 both onshore and offshore. In the South Sea, there is a high maximum RTI onshore every year. In the East Sea, there is a high maximum RTI onshore every year and offshore in 2013. In the sea surrounding Jeju Island, there is a high maximum RTI every year, particularly in 2013 and 2016.

Fig. 20 shows the mean temporal variation in RTI in four different areas: the East Sea, the South Sea, the Yellow Sea, and the sea surrounding Jeju Island, from June to October each year. In the East Sea, there is higher mean RTI and a wider range of red tide occurrence in 2013 than in other years. In the South Sea, on average, there is high RTI unlike in other regions, and it has the widest region of red tide bloom in 2015. In the Yellow Sea, there is a high RTI after June. In the sea surrounding Jeju Island, RTI is usually lower than in

other regions, although there are high RTI values in October 2013 and August 2016.

The spatial characteristics of red tide probability were analyzed using weekly RTI data from 2011 to 2016 (Fig. 21). In general, high red tide probability appears in coastal areas, especially along the southern coastal region of the Korean Peninsula. Based on the standard of red tide warning, RTI > 0.2 can indicate red tide appearance stage with red tide density over 1000 cells/ml. Fig. 21a shows the probability of red tide species appearance stage (RTI>0.2). At the severe red tide bloom level, generally red tide density become greater than 10000 cells/ml. This case is explained by RTI>1.0 according to the relationships between RTI and in-situ red tide density. Fig. 21b represents the probability of severe red tide bloom which is RTI was greater than 1.0. In the case of Jeju showing relatively high probability in Fig. 21a does not show high probability in severe red tide bloom.

Fig. 22 shows year-to-month RTI variation in the four regions. The left column represents the spatial mean RTI and the right column shows the pixels that have an RTI greater than 0.2. In the East Sea, the occurrence of high RTI has moved from June to August over time, and shows a remarkably high extent in August 2013. In the South Sea, high mean RTI appears increasingly early from 2011 to 2013. In particular, in 2013 the red tide occurred and bloomed earlier than in any other period. The red tide extent was broadest in 2015. The West Sea shows different variations from the East and South Seas,

suggesting that it is affected by a different mechanism and system in terms of red tide development. In the sea surrounding Jeju Island, while a high RTI in June and July usually occurs across a small region, August 2011 and 2016 and September 2013 show high RTI with broad extensions. The case of 2016 is discussed in section 4.3.5.

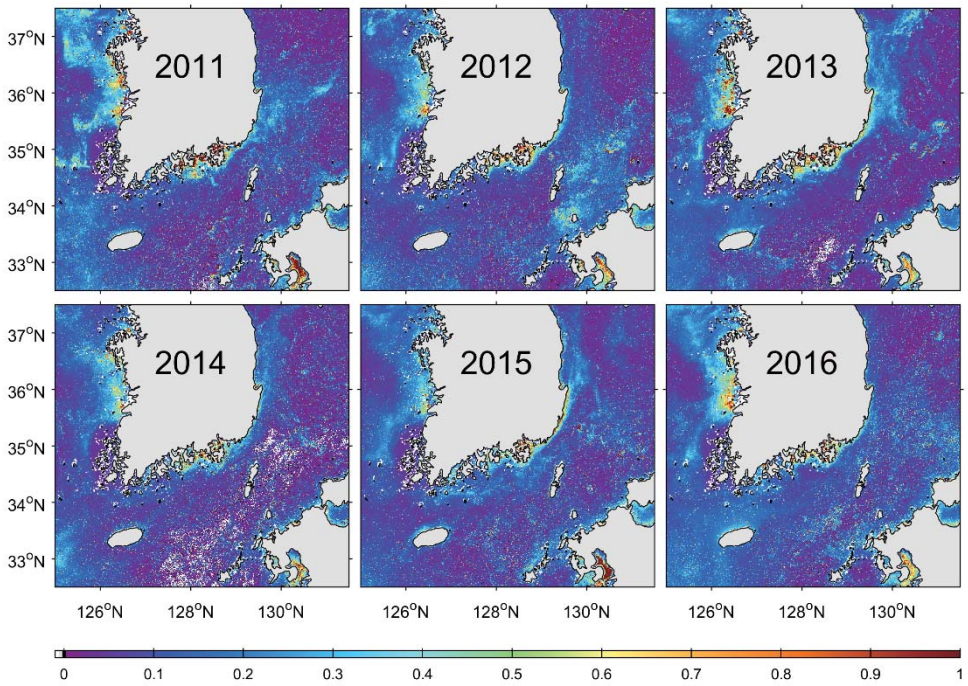

Fig. 18. Year-to-year variation in mean RTI from 2011 to 2016 (June-October).

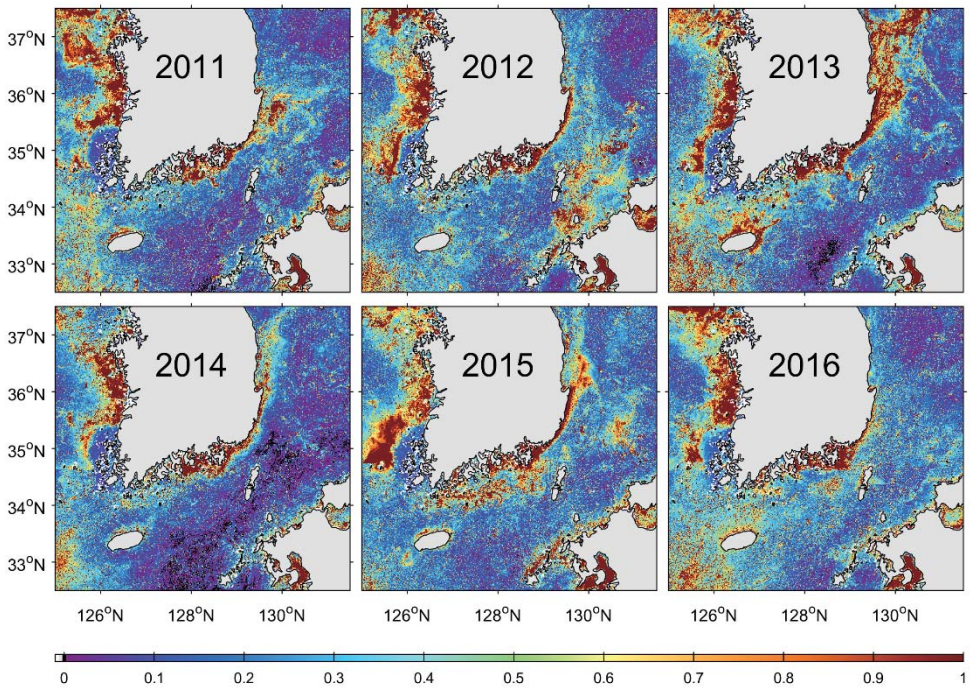

Fig. 19. Year-to-year variation in maximum RTI from 2011 to 2016.

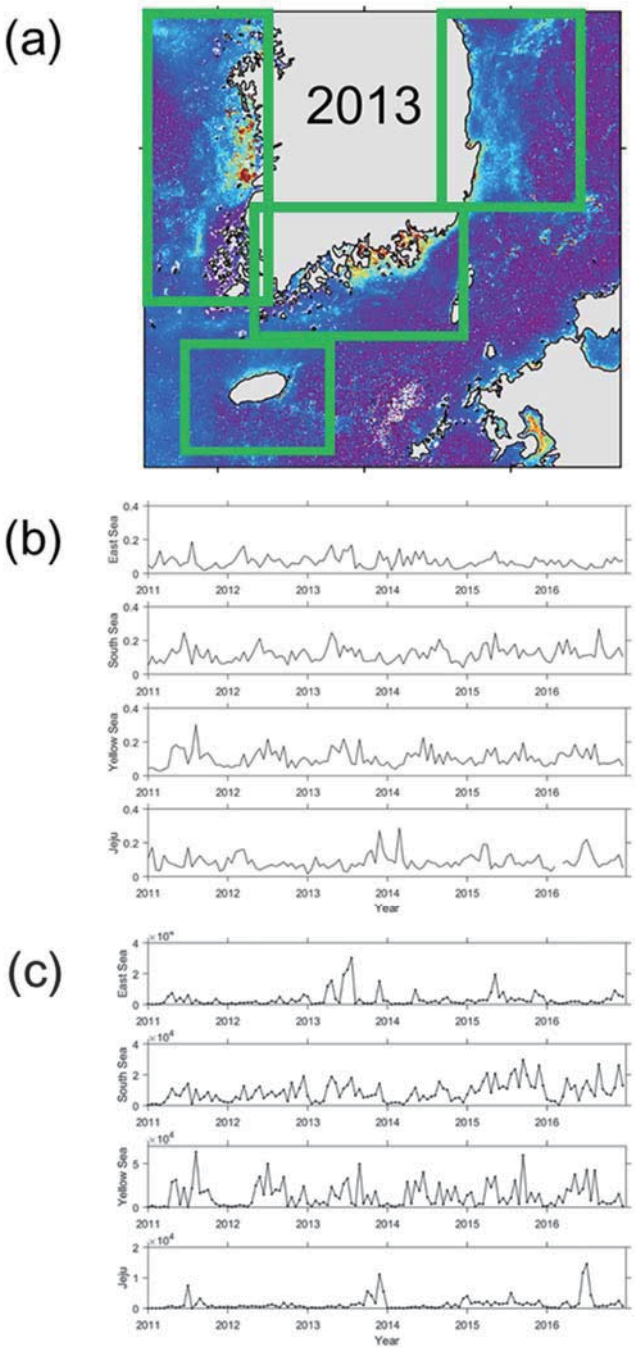

Fig. 20. (a) Map of subsampled region, boxes represent the East Sea, South Sea, Yellow Sea, and Jeju regions. (b) Time-series of mean RTI variation, (c) RTI numbers greater than 0.2 from June to October in the period from 2011 to 2016.

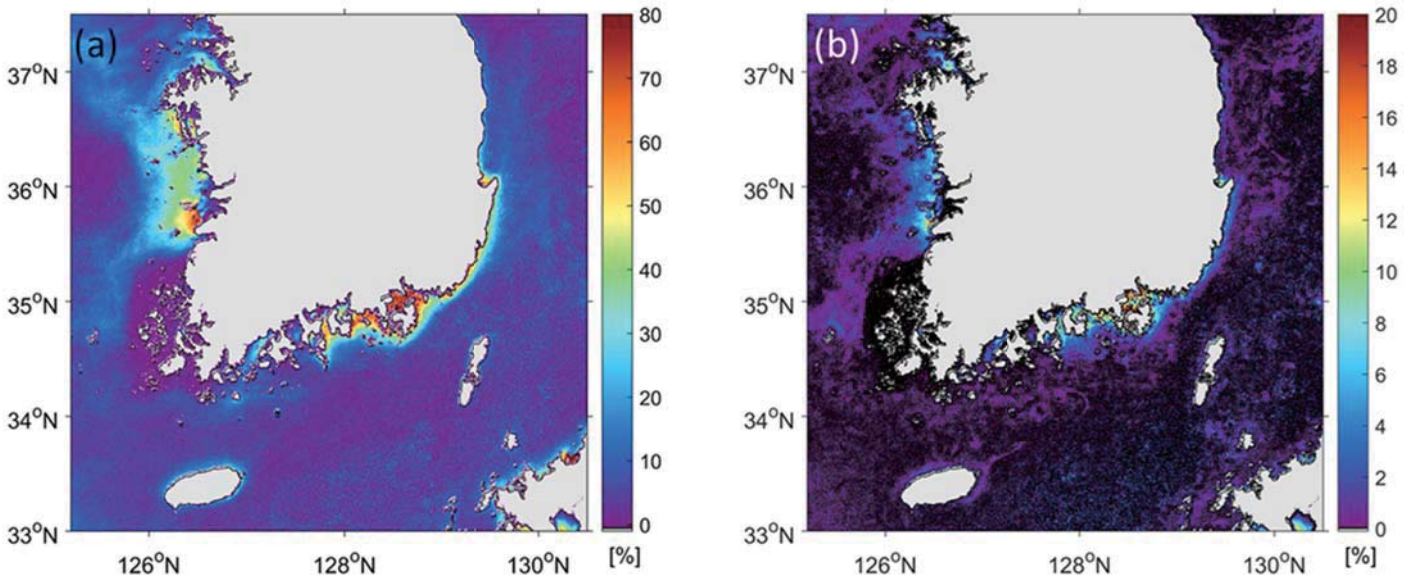

Fig. 21. Probability (%) of red tide (a) RTI > 0.2, (b) RTI > 1.0 in the period from 2011 to 2016 (June-October).

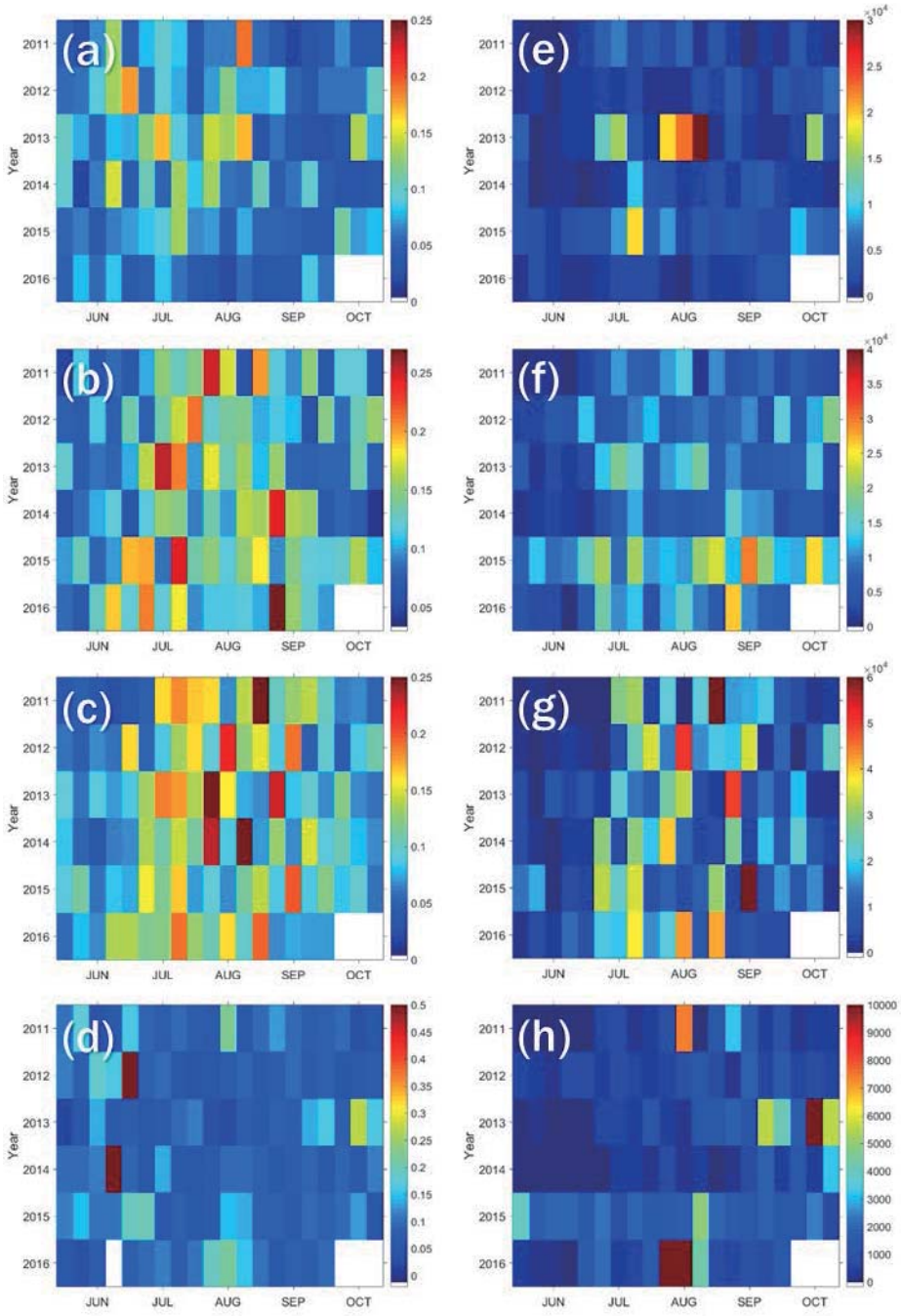

Fig. 22. Year-to-month variation in mean RTI near (a) the eastern, (b) the southern, (c) the western coasts of Korea, and (d) Jeju Island and extent of RTI greater than 0.2 near the (e) the eastern, (f) the southern, (g) the western coasts of Korea, and (h) Jeju Island.

4.3.1. Along-Shore Variability of Red Tides

To analyze the temporal and spatial variation of the occurrence of red tides in the coastal region of the Korean Peninsula where the probability of red tides is high, the area was divided into two sections according to distance from the coastline (Fig. 23). Areas within 10 km of the coastline were defined as onshore, and areas 10–30 km from the coast were defined as offshore. In the case of Jeju Island, onshore and offshore were split around the distance of 5 km from the coastline.

Fig. 24 shows the temporal and spatial variations in RTI in the onshore region. The frequency of red tide occurrence, intensity, and duration have different characteristics according to the area. The time-averaged value in each sub-section is different. Based on these characteristics, the study area was divided into five areas from R1 to R5. From 2011 to 2016, red tides occurred with high intensity along the west coastal region (R1) and coastal areas from Namhae to Busan (R4). Red tides frequently occur in the coastal region of the East Sea (R5), but the frequency of occurrence is lower and the maintenance period shorter than in R1 and R4. On the other hand, there are few red tides in the coastal area of Mokpo (R2).

Offshore, the frequency of red tides is low, and they have a short duration (Fig. 25). The difference in RTI between onshore and offshore is shown in Fig. 26. The frequency of occurrence of red

tides in R4 and R5 is significantly reduced compared to that onshore, while red tide concentration and frequency in R2 and R3 regions slightly increases. The R2 region, where red tides are rarely observed onshore, has strong red tide blooms in 2012, 2013, and 2015 offshore. This may be due to the introduction of cold water by tidal mixing.

In early June 2013, a red tide began in the western seas of R4, and gradually spread eastward over time. To reveal the red tide movement, Radon transform was applied to quantify the propagation velocity; the red tide was moving at a speed of 0.1290 m/s. This speed was compared with the geostrophic velocity calculated from satellite altimetry data, which was about 0.1 m/s, similar to the radon transform calculation result.

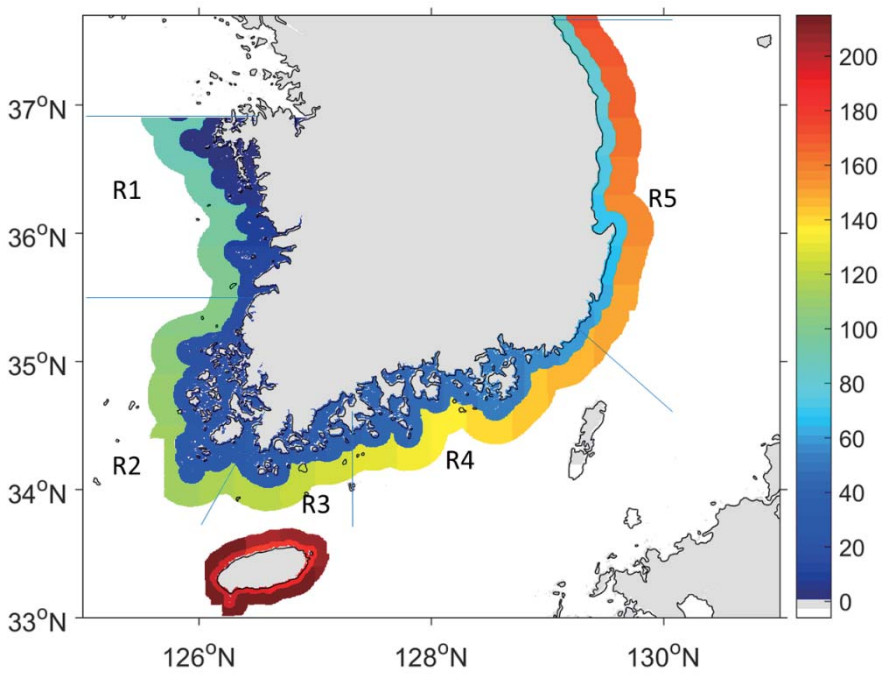

Fig. 23. Map of along-coast regions (Onshore/Offshore). Colors represent the order of subsampled region.

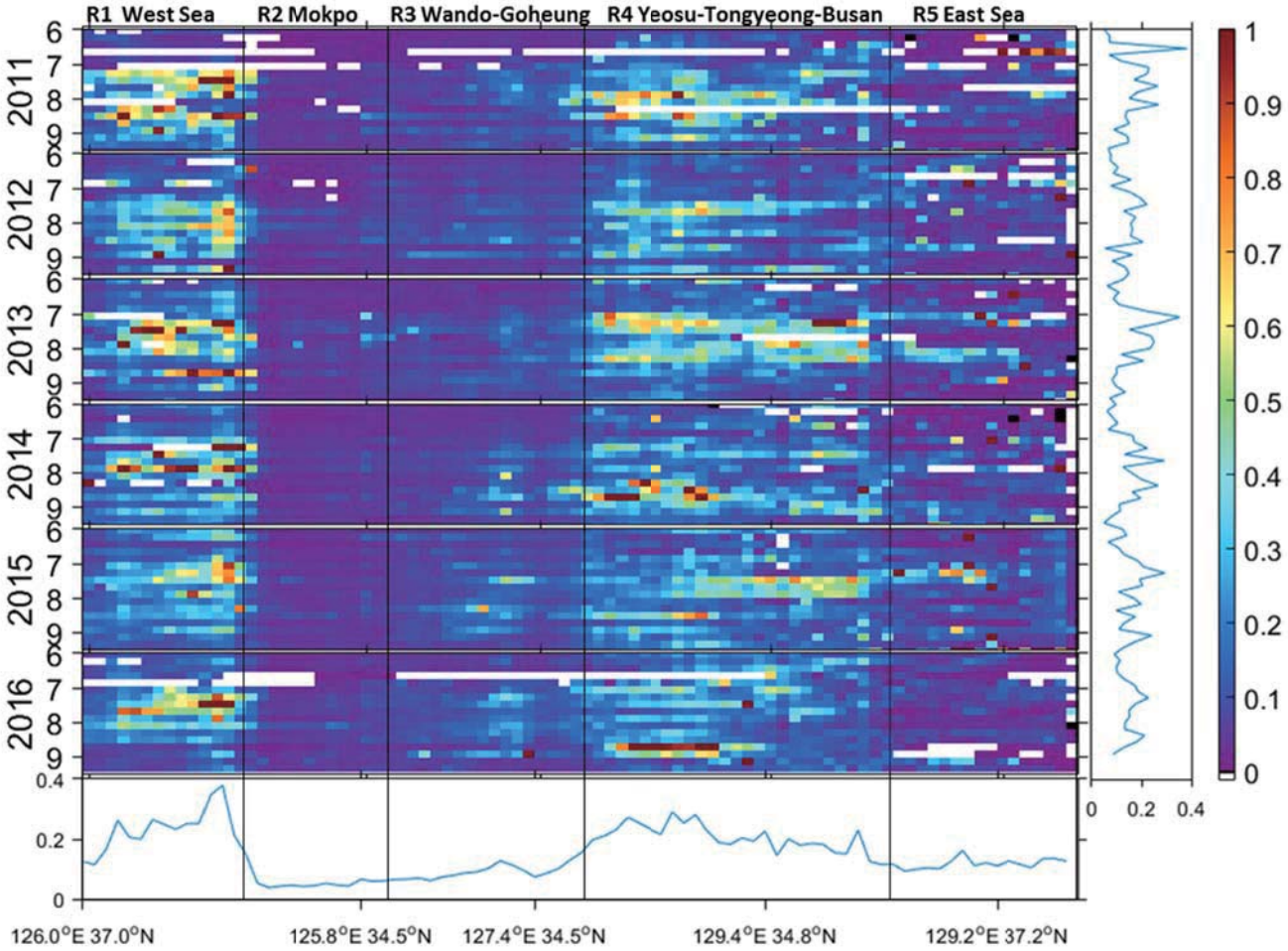

Fig. 24. RTI time series along the onshore coast from 2011 to 2016, and time series of the along-coast RTI averages (right), and RTI spatial mean during the period 2011 to 2016 (bottom).

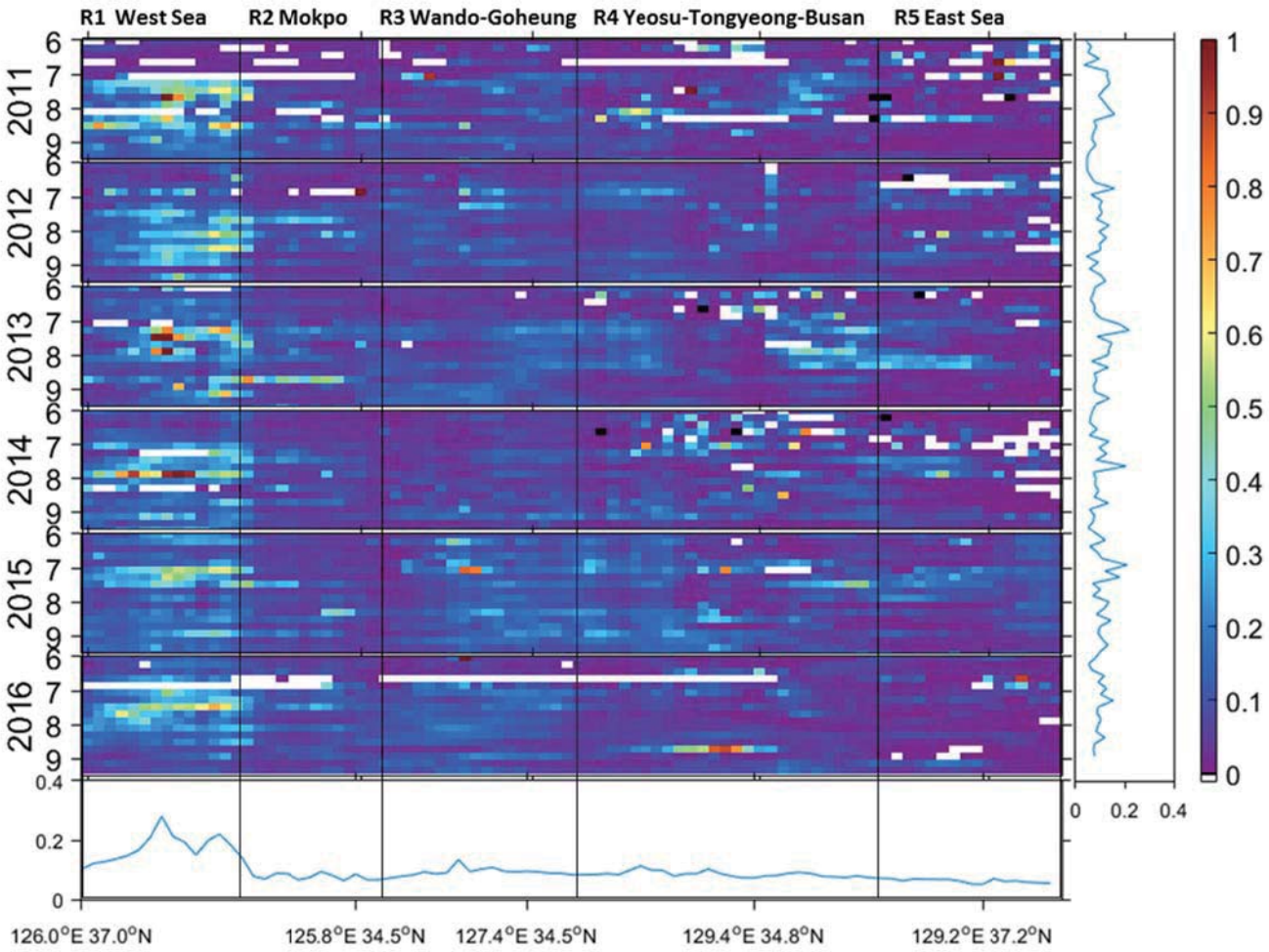

Fig. 25. RTI time series along the offshore coast from 2011 to 2016, and time series of the along-coast RTI averages (right), and RTI spatial mean during the period from 2011 to 2016 (bottom).

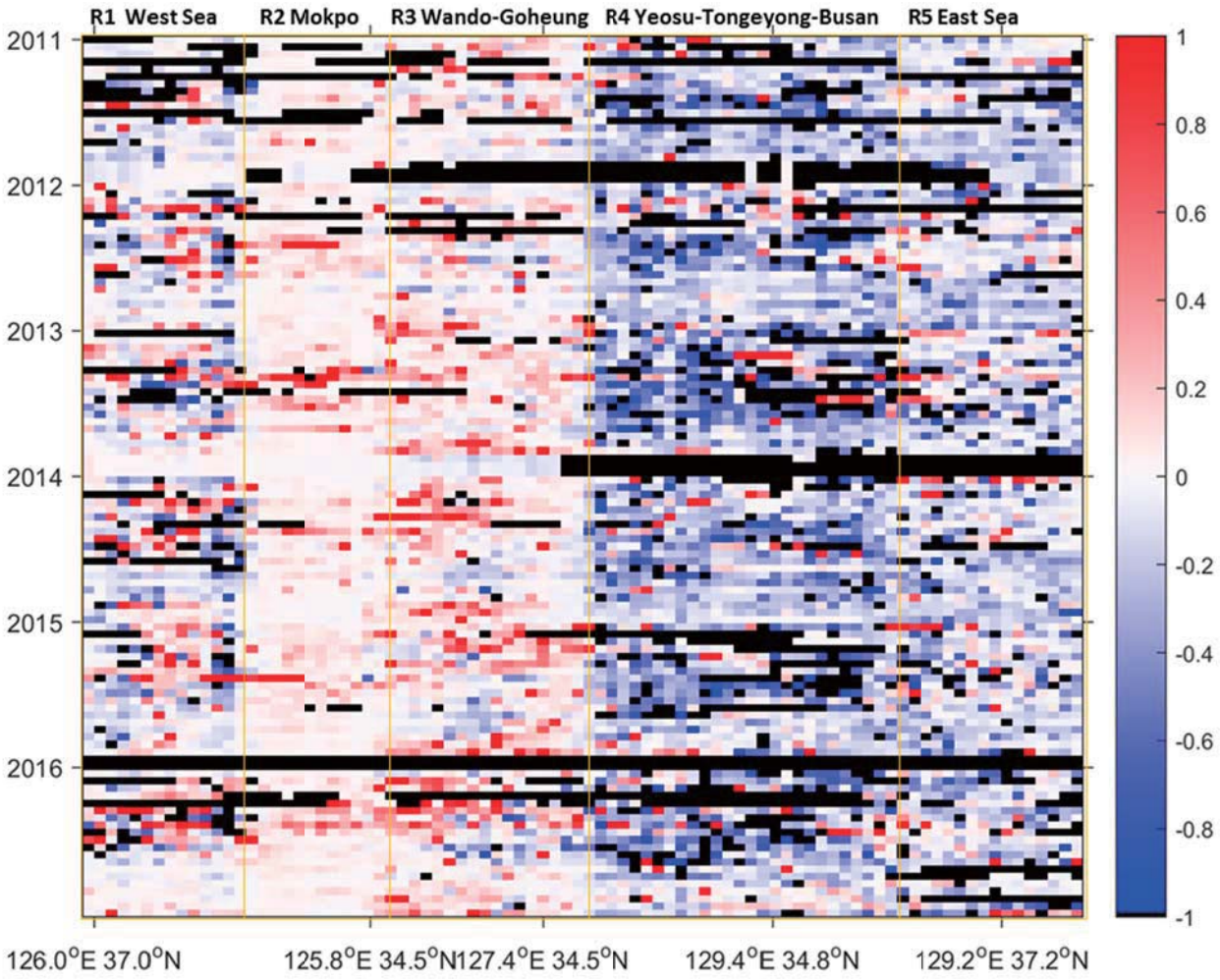

Fig. 26. Time series of RTI difference along the coast between onshore and offshore from 2011 to 2016; positive values indicate that RTI is greater offshore than onshore.

4.3.2. Across-Shore Variability of Red Tides

The variation in across-shore direction was analyzed for each area, in order to investigate the time-dependent characteristics of onshore and offshore red tide blooms (Fig. 27). As shown in section 4.3.1, red tides occur with more intensity onshore than offshore. Also, red tides near the coast tend to be transmitted from offshore. In R4 in 2013, a red tide occurred at around 34.7° N at the initial stage of the red tide bloom, but it gradually moved towards the north (onshore) over time. This tendency was observed not only in R4 but in all regions in 2013 (except R1), and this characteristic is repeated in most years of the study period. In addition, Fig. 27 shows the time-averaged RTI for each region. Two sharp peaks appear in R5 during 2013 (Fig. 27). Generally, the location of a red tide can shift incrementally, but it rarely reappears in areas through which it has passed. However, the red tide in R5 in 2013 disappeared for about two weeks in the middle of July, and was then regenerated from the beginning of August. This phenomenon can be observed when two red tides are caused by different mechanisms, but further study is necessary to fully understand this.

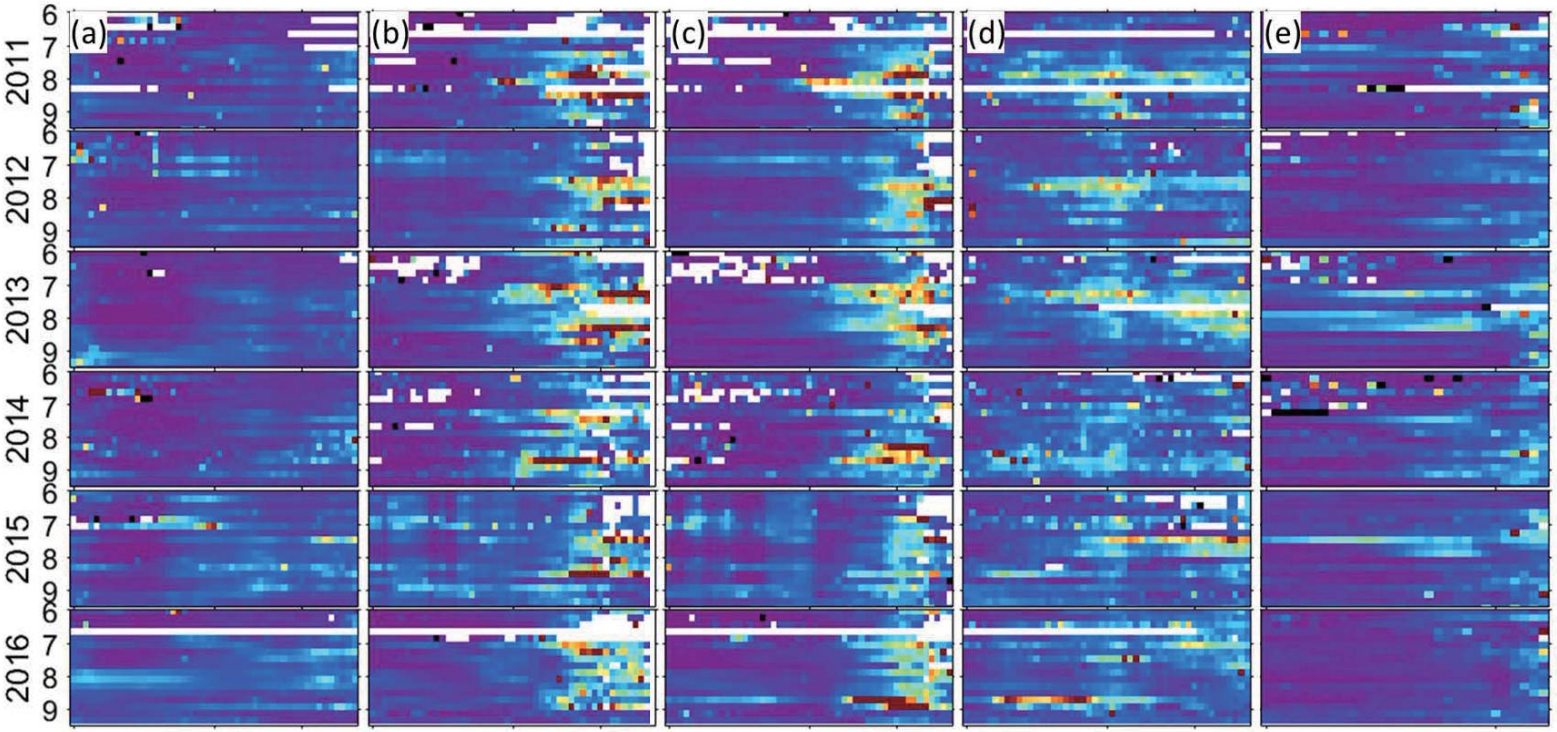

Fig. 27. RTI time series across the coast near (a) Wando, (b) Yeosu, (c) Tongyong, (d) Busan, and (e) Uljin from 2011 to 2016, and time series of along-coast RTI averages (right), and RTI spatial mean during the period from 2011 to 2016 (bottom).

4.3.3. Occurrence Time of Maximum Red Tide Bloom

To show the spatial distribution of the time at which a red tide blooms, RTI values and their corresponding dates are indicated in Fig. 28. The left-hand plot of each pair in Fig. 28 shows the RTI value when it reaches a maximum at each position. At this time, a red tide was distributed widely in the coastal area of the Korean Peninsula. The maximum values are generally high in the R1 area of the Yellow Sea and the R3 area of the South Sea of Korea. In R2, the southwestern coast of Korea, the offshore region has higher RTI than onshore, while R3 and R4 show larger RTI values onshore. This suggests that the mechanism creating the red tide is different depending on the area of the sea involved. Fig. 28 shows the Julian day of the maximum RTI. The date varies according to sea area. At the end of June 2013, a red tide began to flourish in the vicinity of Yeosu, which is located in R3, then the bloom moved eastward over time; it propagated at Geoje Island in July and at Pohang in August. This trend shows that red tide advection occurs along the coast. On the west coast, the red tide bloom appeared in July, while in the southern part of the country, between Wando and Jeju Island, the red tide flourished in late September. The time of year during which the red tide prospers varies according to the sea area, and in some sections the red tide bloom was observed to move along the coast.

The right-hand plot of each pair in Fig. 28 shows the date of the annual RTI maximum for the six years from 2011 to 2016. The place

where the red tide bloom begins to appear varies annually. In 2013, the red tide propagates first near Geoje Island, and gradually moves to the East Sea. In contrast, in 2016 the red tide first appeared in the East Sea and then advected to the southern coast of Korea. Furthermore, the times at which the red tide is greatest also differ. In 2013, the red tide flourished from the middle of July to early August, while in 2016 it flourished rather earlier, from mid-June to mid-July.

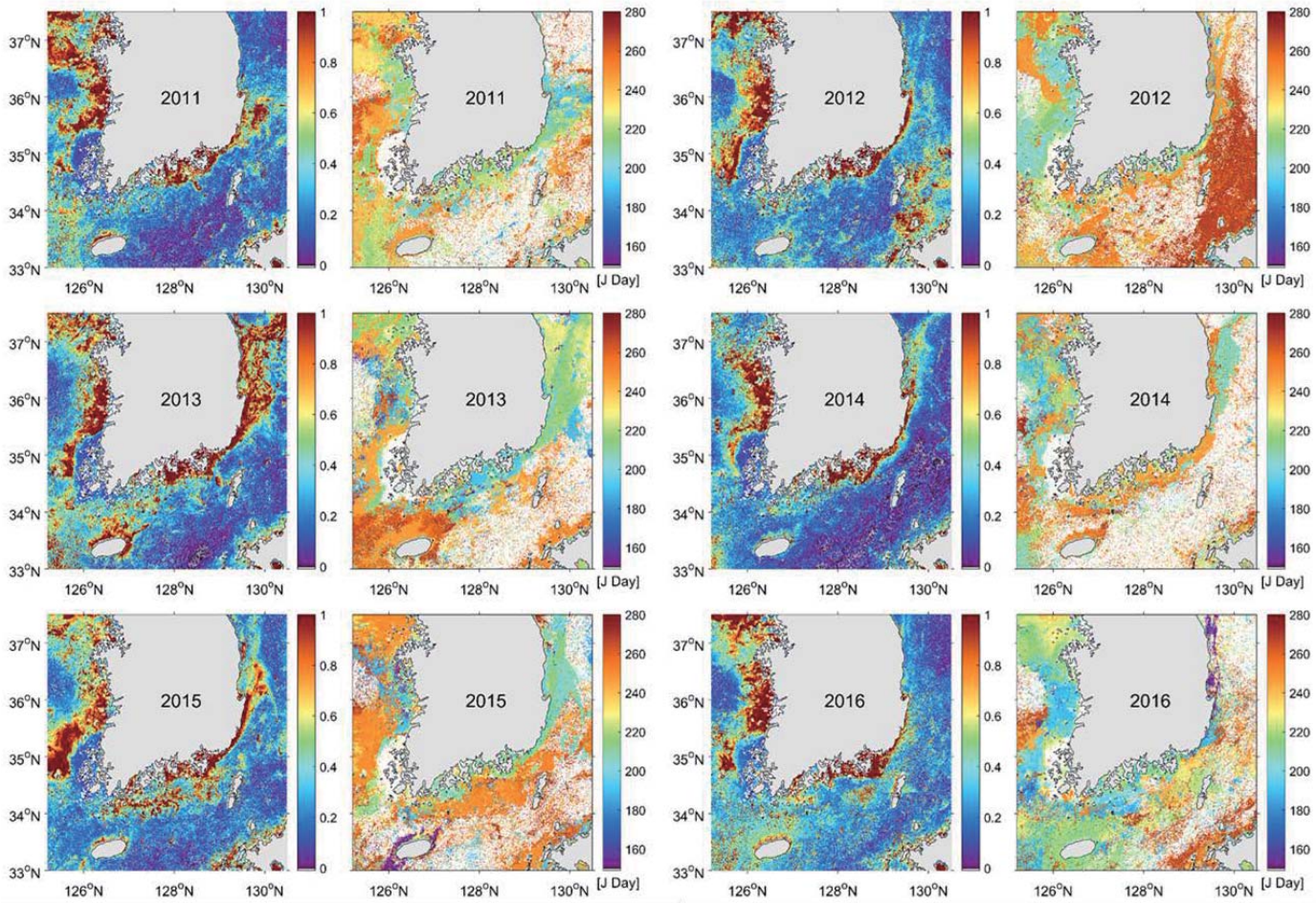

Fig. 28. Maximum annual RTI and the day the maximum was RTI observed (2011-2016).

4.3.4. Life Span of Red Tide Bloom

In order to analyze the life span of red tide blooms, the date of first and last appearance of RTI >0.2 was investigated for each area. The period between the first and last date was defined as the duration of the red tide. The duration defined in this way enables an understanding of how long a red tide lasts in each area and how this changes annually. The characteristics of red tide bloom in each area can thus be recognized.

To examine the duration of the red tide bloom for each area, subsampling was used to classify onshore and offshore as defined in section 4.3.1 and the duration for each area was analyzed from 2011 to 2016 (Fig. 29). Regarding annual variations in red tide duration onshore, a red tide bloom appeared continuously in the Yellow Sea of R1, with some locations showing a duration of more than 60 days. Red tide blooms rarely appear in R2 and R3, and show no persistence when they do appear. The longest duration is found in R4, which is the region with the highest RTI. There are many locations with a long duration exceeding 80 days in 2013 and 2015 when strong red tides occurred.

For the offshore region, the red tide bloom always appears in the Yellow Sea of R1, similar to the onshore region. However, in R2 and R3, there are red tides with a duration of more than 20 days offshore, unlike in the onshore region. It can be inferred that the red tide has continued to the outer sea in R2 and R3. Compared with the variation

in the onshore region, offshore R4 shows relatively small variability. Red tides in the East Sea in R5 have a longer duration offshore than onshore. In 2013, a long-lasting red tide was clearly visible even in sea distant from the coast.

The spatial distribution of red tide duration is indicated in Fig. 30. For each year, a duration of about 50 days is observed near the coastline in R1, R4, and R5. In particular, the overall duration was relatively long in 2013 and 2015.

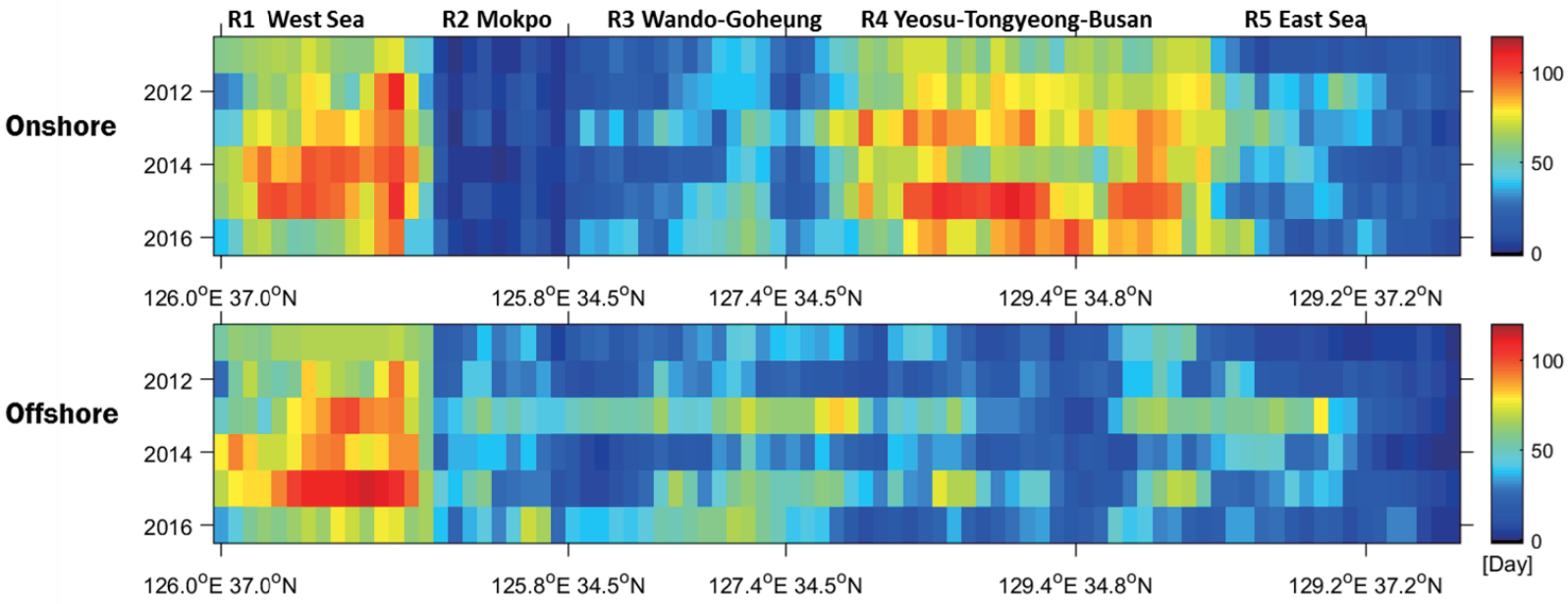

Fig. 29. Time series of red tide bloom duration (RTI > 0.2) along the coast onshore (upper) and offshore (bottom) from 2011 to 2016. Color represents duration days.

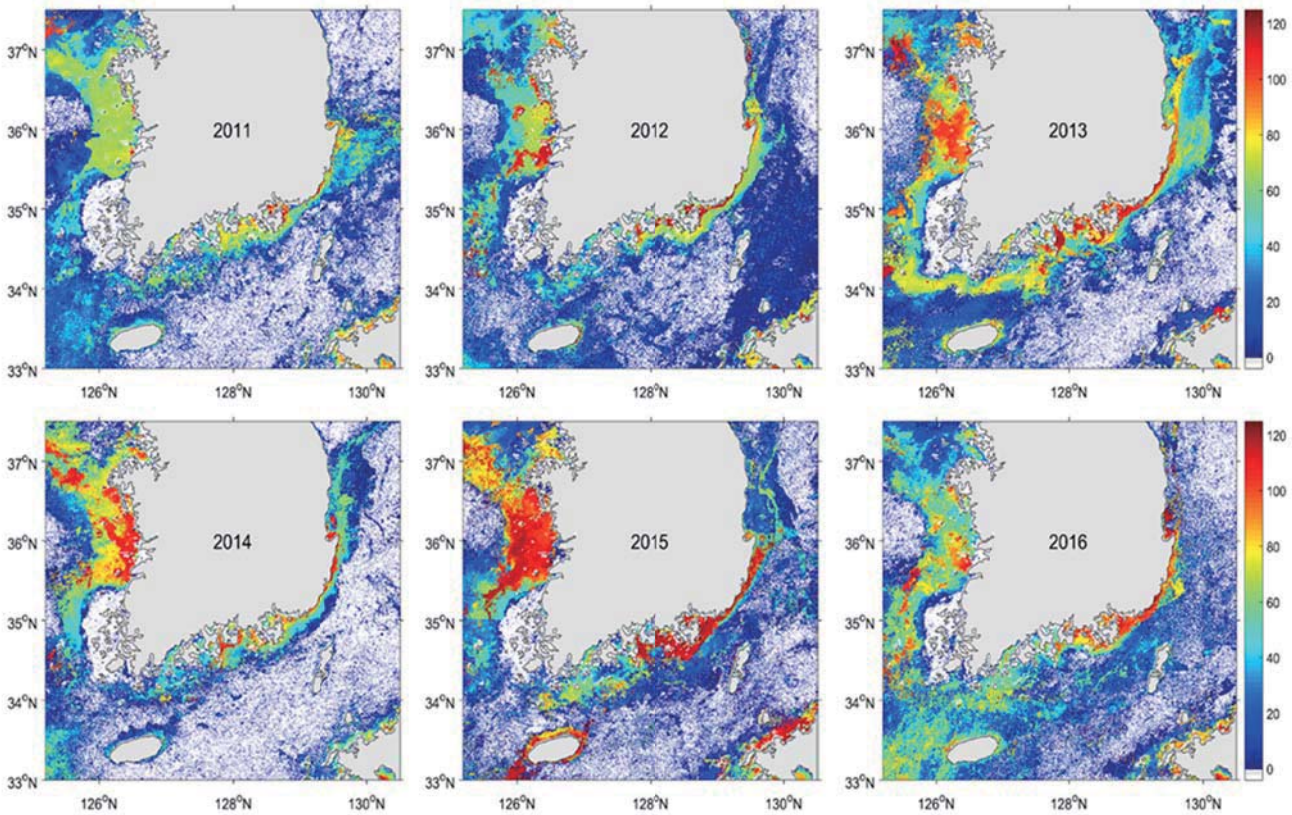

Fig. 30. Year-to-year variations in red tide bloom duration from 2011 to 2016. Colors indicate duration days.

4.3.5. Red Tide Bloom near Jeju Island

4.3.5.1. Peculiar spatial distribution of red tides in 2016

The spatial distribution of the weekly RTI from June to October, the season in which red tides can appear, shows a relatively low RTI in the coastal area of the Korean Peninsula in 2016 (Fig. 31). However, a relatively high RTI of 0.2 or more appears along the northern coastal region of Jeju Island in August, with a broad extent (Figs. 22d (right) and 31). High RTI begins on August 9 and is maintained until August 16. After August 23, the red tide declines, resulting in a low RTI value. The spatial distribution of RTI in the East China Sea can be used to investigate whether the high RTI in the coastal region of Jeju Island was caused by movement of currents. On July 5, a high RTI appears on the coast of the Yangtze River (Fig. 32). As time passes, the red tide moves to the east and reaches the coastal region of Jeju Island on July 26, 2016.

Fig. 33 shows the spatial distribution of the weekly RTI in 2013; there are extreme red tides on the coast of the Korean Peninsula. In July, the RTI exhibits high values along the southern coastal region of the Korean Peninsula. In August, high values are present in not only the southern but also the eastern coastal regions. However, in the coastal area of Jeju Island, high RTI is found after

September 20, when the red tide bloom around the Korean Peninsula has declined.

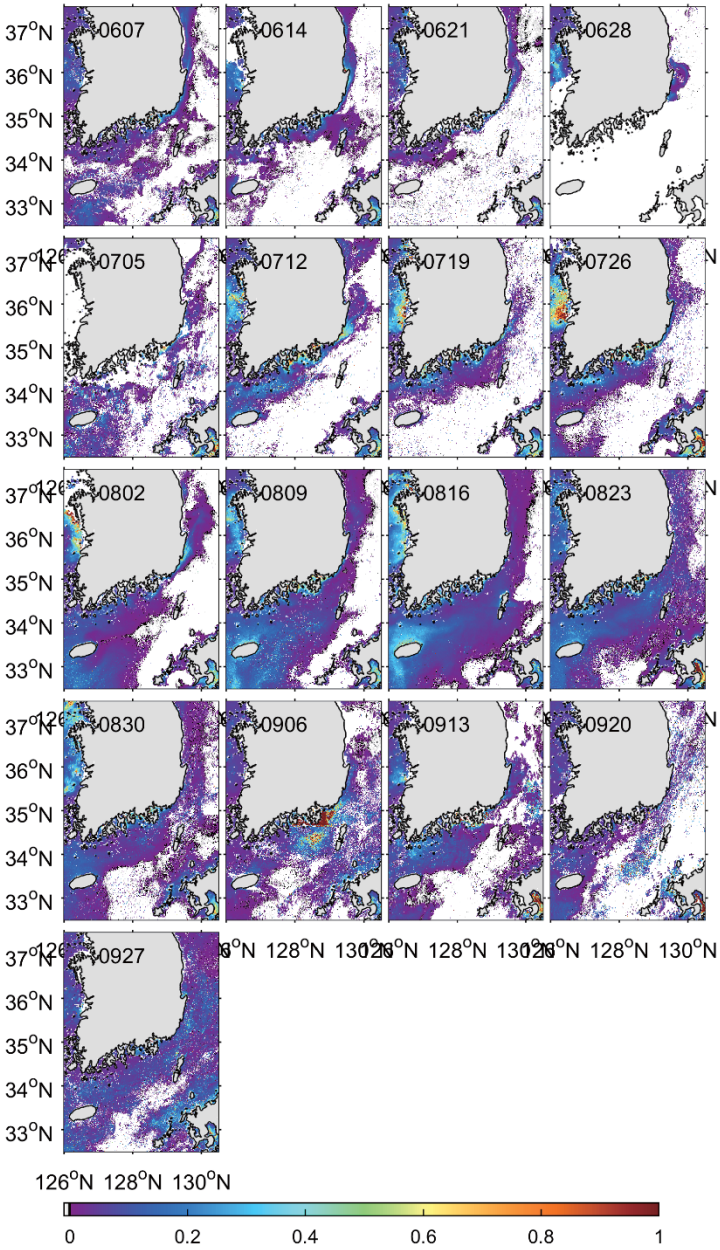

Fig. 31. Spatial distribution of weekly RTI composite data from June to September in 2016.

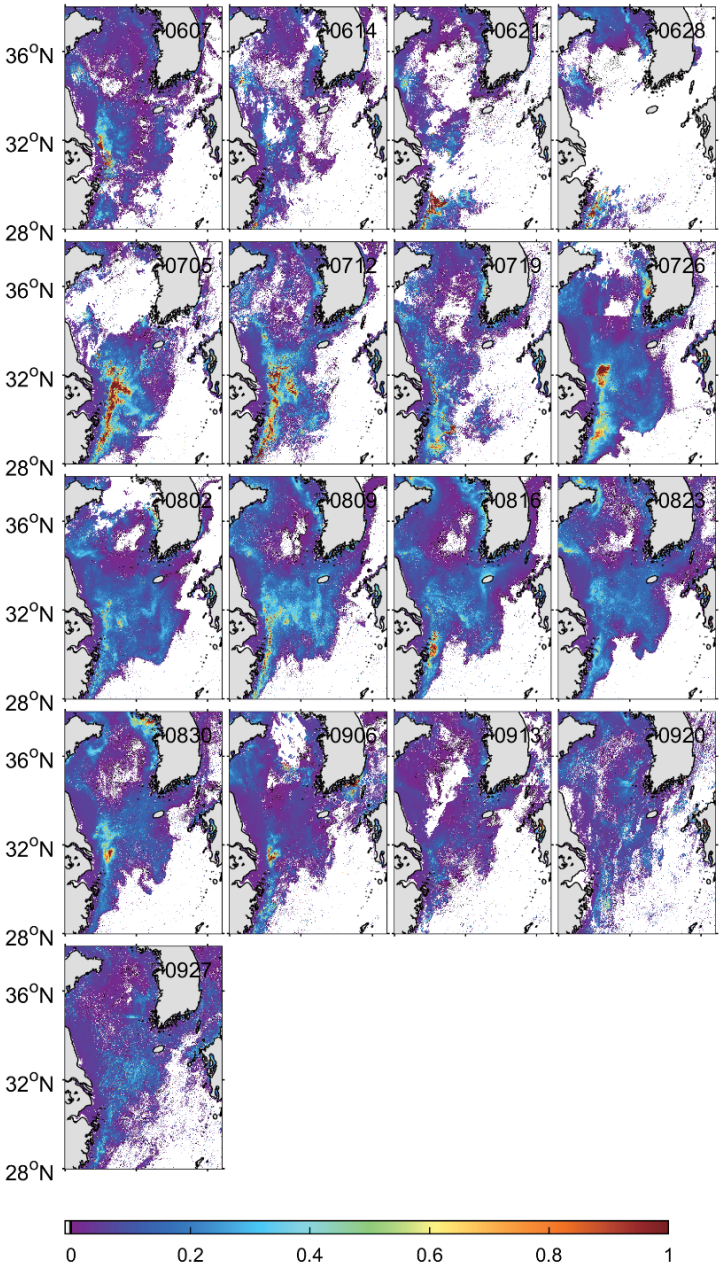

Fig. 32. Weekly RTI spatial variation map in 2016

.

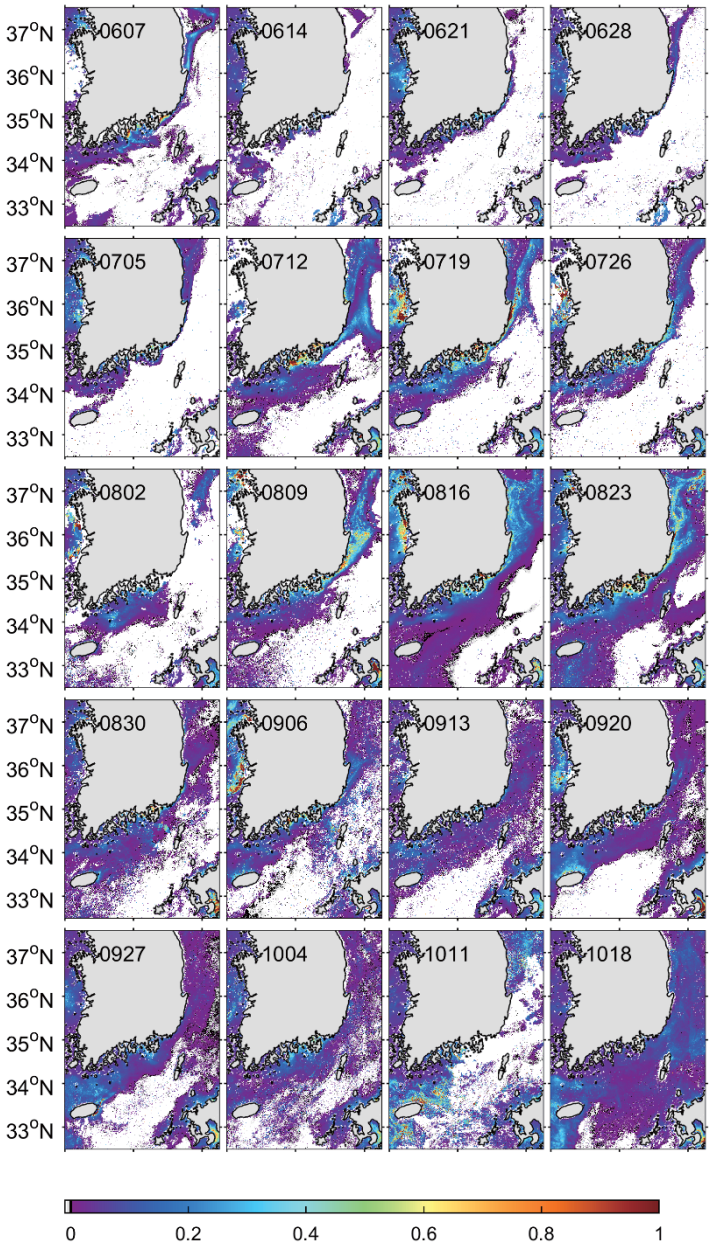

Fig. 33. Weekly RTI spatial variation map in 2013.

4.3.5.2. Tracking red tides in the Yangtze River region

In 2016, low salinity surface water from the Yangtze River was reported to have flowed to the coast of Jeju. The influence of Yangtze River runoff could be one of the factors contributing to an exceptionally high RTI in the coastal region of Jeju Island in 2016. Fig. 34 represents the monthly variation in Yangtze River discharge from 1995 to 2016. Since GOCI began observations in 2011, the largest amount of runoff occurred in July 2016.

To investigate whether the Yangtze River runoff reached Jeju Island, we traced some seeds after spraying in the area where the RTI was more than 1 (red points) and the area around the Yangtze River (blue points) on July 5, 2016 (Fig. 35). The geostrophic current by satellite altimeter data, with wind-driven current by ECMWF wind data, was used to track red tide seed movement from Yangtze River mouth in July. The seeds spread widely in the East China Sea, but moved eastward along the currents. Seeds with rapid migration arrived in the southern part of Jeju Island on August 9. It took about 40 days for the current to travel from the Yangtze River to the coastal region of Jeju Island.

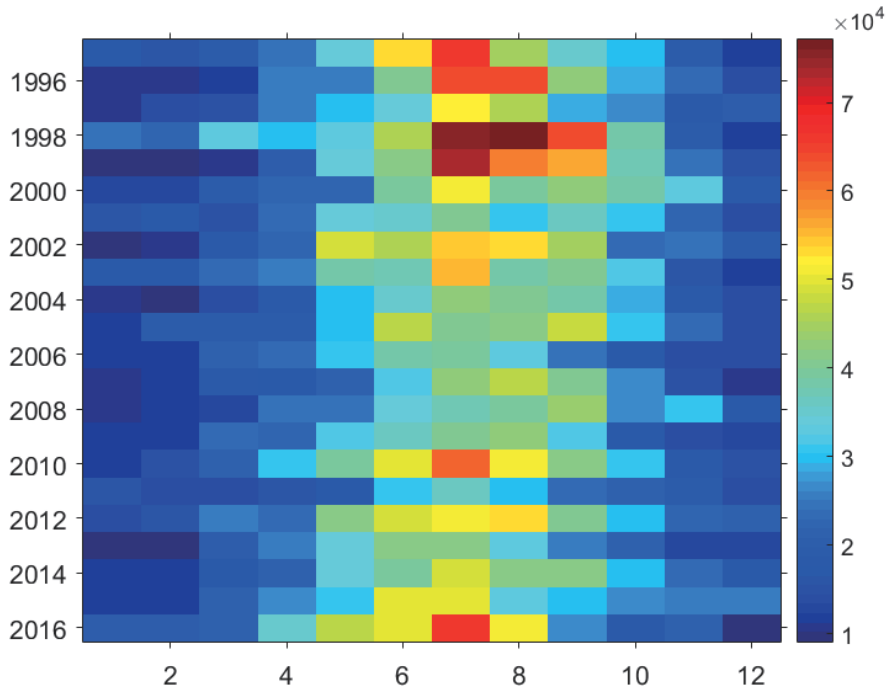

Fig. 34. Year-to-month variation in Yangtze River discharge (m^3/s).

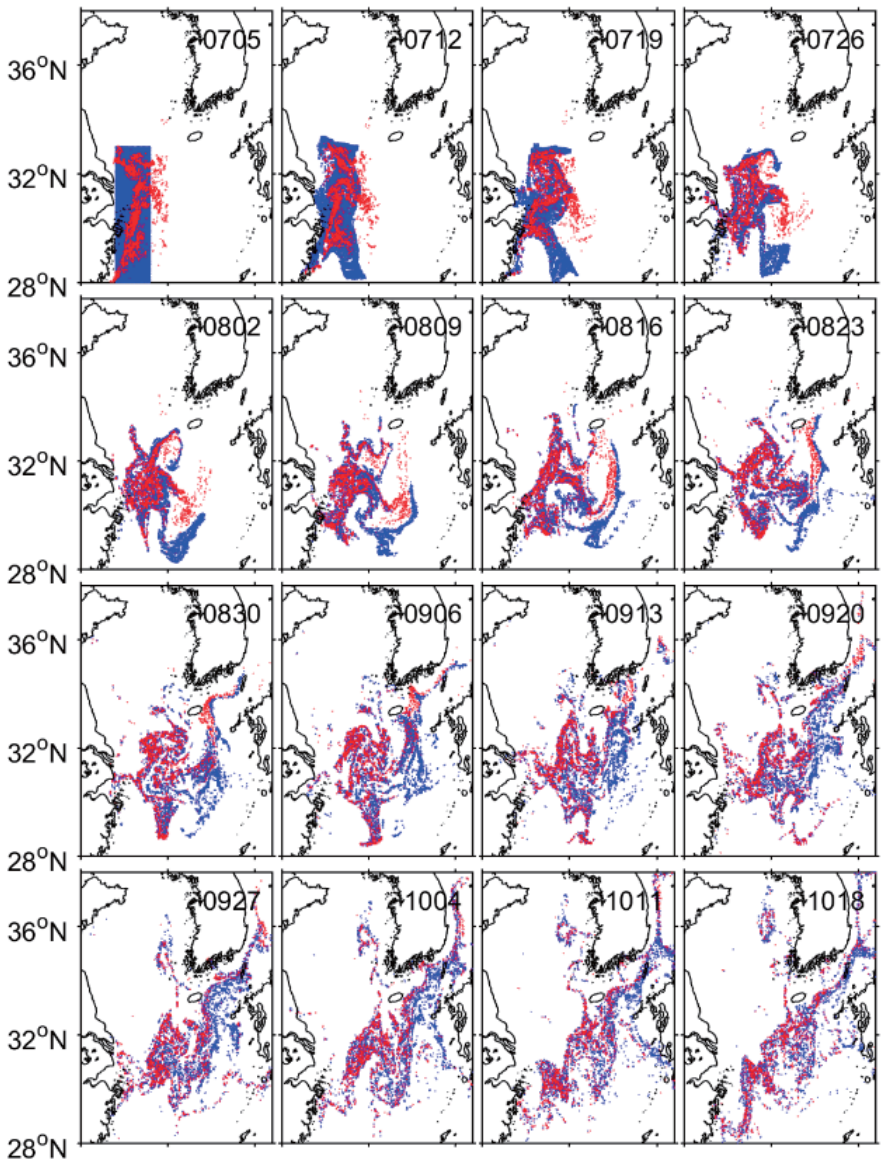

Fig. 35. Tracking result of Yangtze River discharge (blue) and red tide bloom at the river mouth.

4.3.5.3. In-situ red tide occurrence around Jeju island

According to the red tide probability map (Fig. 20), red tides have occurred 20% of the time during the period from June to October in the last six years. Yoon et al. (1991) measured eight species of red tide around Jeju Island and reported monthly density at in-situ points from June to October (Fig. 36). Shah et al.(2013) found new species of red tide at Jeju Island and suggested that red tides around Jeju should be further researched and monitored. However, the NFRDI red tide report does not mention red tides around Jeju Island; they are not well-known.

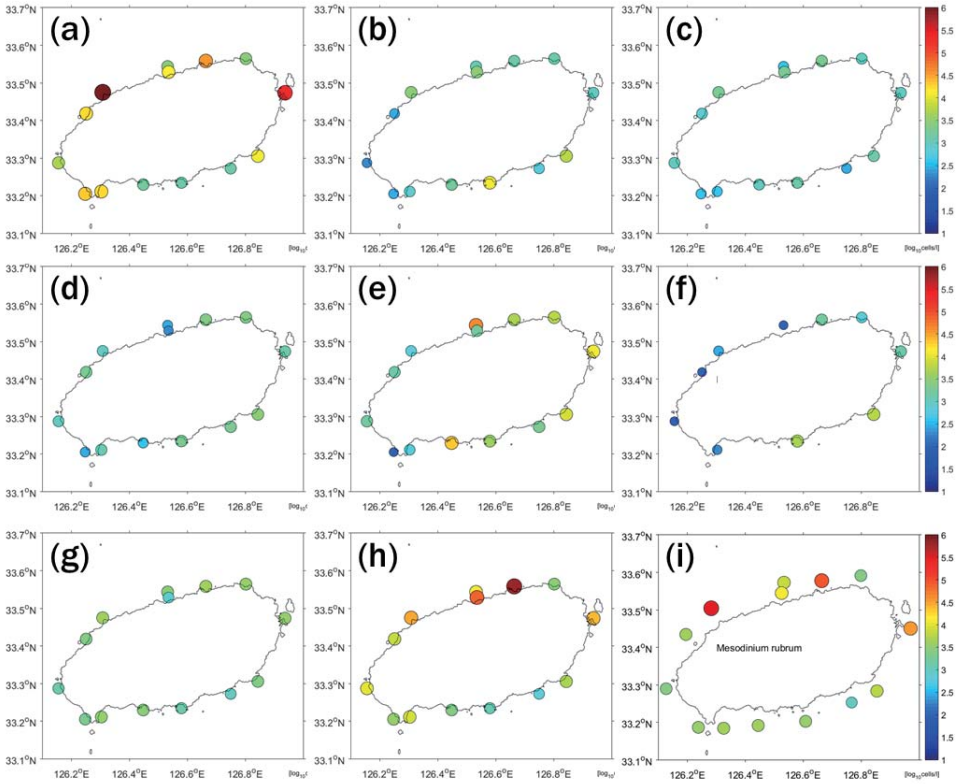

Fig. 36. In situ red tide density (Yoon et al., 1991) of (a) Chaetoceros spp., (b) Eutreptiella spp, (c) Gymnodinium spp., (d) Gyrodinium spp., (e) Heterosigma akashiwo, (f) Mesodinium rubrum, (g) Prorocentrum triestinum, (h) Skeletonema costatum, and (i)mean density of All around Jeju Island from June to October in 1989.

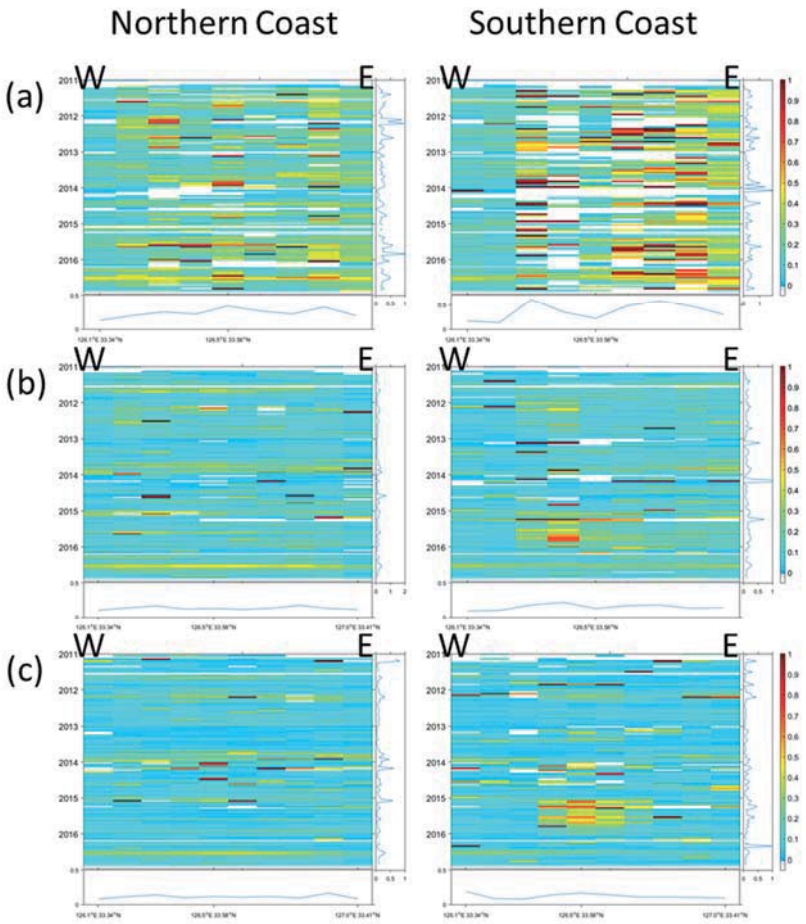

Fig. 37. RTI time series along the Northern/Southern (left/right) (a) < 1 km (b) 1–5 km coastal regions (c) offshore of Jeju from 2011 to 2016, and time series of the along–coast RTI averages (right), and RTI spatial mean during the period from 2011 to 2016.

4.3.5.4. Spatial variability of red tides around Jeju island

To elucidate the spatial characteristics of red tides around Jeju Island, we divided the sea into northern coast and southern coast, and more specifically into distance from land: inner region (<1 km), intermediate region (1–5 km), and offshore (5–10 km). Fig. 37 shows the time series of RTI along the coast divided into the six regions. Red tides have occurred more often and with greater intensity in the inner region, especially on the southeastern coast of Jeju. This coincides with the in-situ map (Fig. 36). Red tide occurrence shows a different tendency to that of the area surrounding the Korean peninsula. The pattern at Jeju Island seems to be affected by local phenomena over short timescales. Peculiar RTI variation in 2016 is shown in Fig. 37 as a yellow horizontal line during August 2016, with a wide range in the distance from land in the northern part, and in the coastal region in the southern part.

4.4 Potential Causes of Red Tide Bloom

To identify the proper temperature of red tides, we collected Sea Surface Temperature (SST) data at in-situ red tide bloom regions based on the NFRDI red tide report map. Fig. 38 shows the frequency of different SST at red tide bloom regions. Where there is a red tide bloom, SST falls within the range of 18 ℃ to 30.5 ℃ and shows bimodal tendency at 20.5 ℃ and 24.5 ℃. This is in agreement with the proper water temperature of red tide species reported in previous research.

As red tide species photosynthesize to maintain metabolic activity, PAR is crucial to red tide growth. PAR is radiation in the range of visible channels from 400 nm to 700 nm. Visible channels can be obscured by cloud. Therefore, cloudiness can replace PAR as its reciprocal. To elucidate the relationship between solar radiation and red tide bloom, cloudiness calculated by GOCI data observation rate can be compared with one week-delayed RTI at the same location. Fig. 39 shows RTI variation as a function of cloudiness on the southern coast of Korea. There is also a time delay before the intensity of radiation or the accumulated amount of solar radiation elicit a response, such as the promotion of red tide photosynthesis, increases in SST, or stabilization of the water column.

The occurrence of red tide bloom phenomena triggered by nutrient supply from upwelling is a well-known theory. Selecting a year with severe red tides, we tried to reveal the relationships between red

tide bloom and wind-driven effect. One week-delayed RTI (box region in Fig. 40) shows a positive relationship with U-component wind, across the coastal line, in 2013. It is assumed that the response of red tides to wind is not instant.

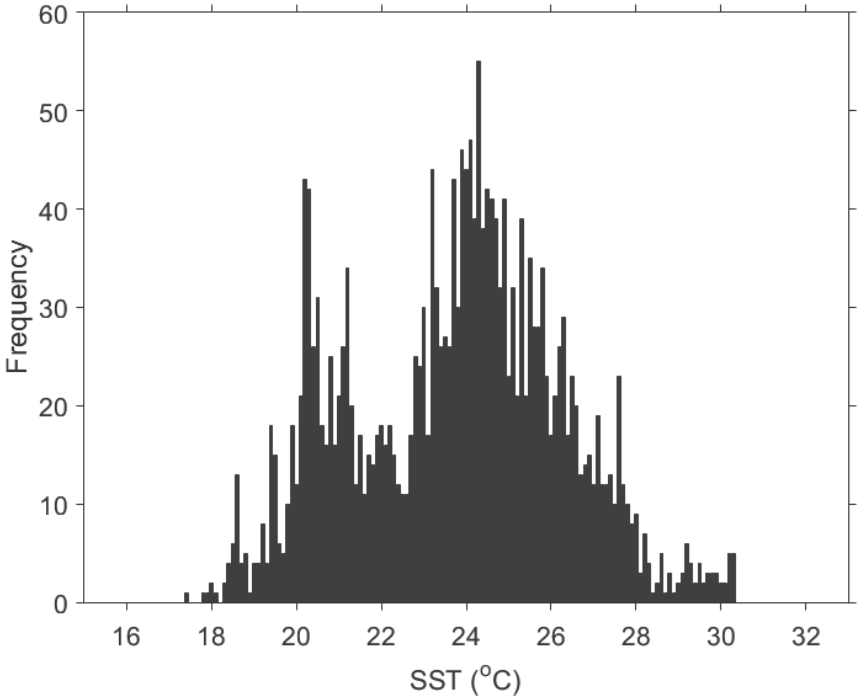

Fig. 38. SST frequency for the in situ red tide bloom region.

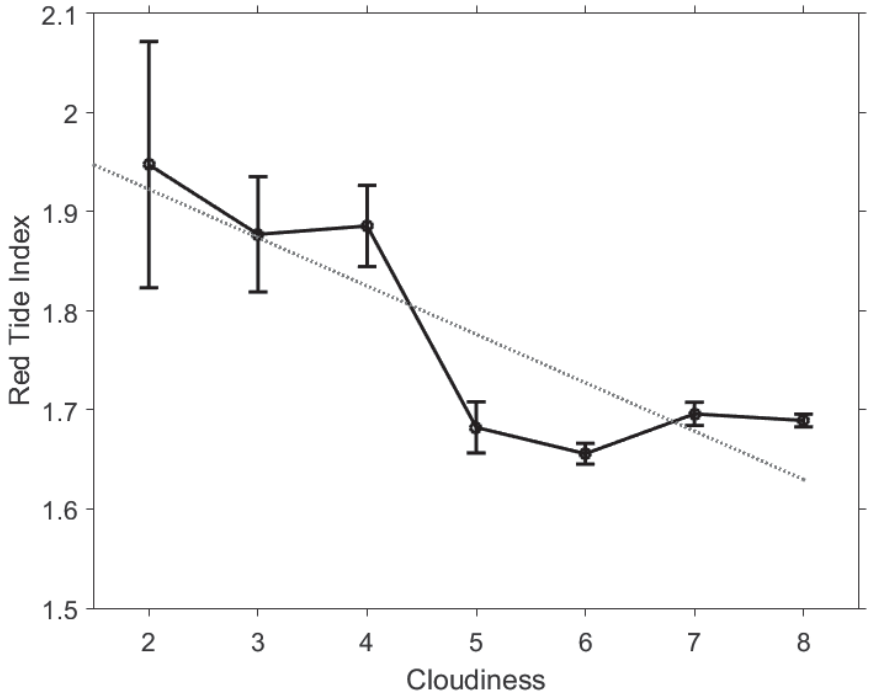

Fig. 39. Spatial mean RTI of subsampled area along the southern coast of Korea presented as a function of cloudiness from 2011 to 2016.

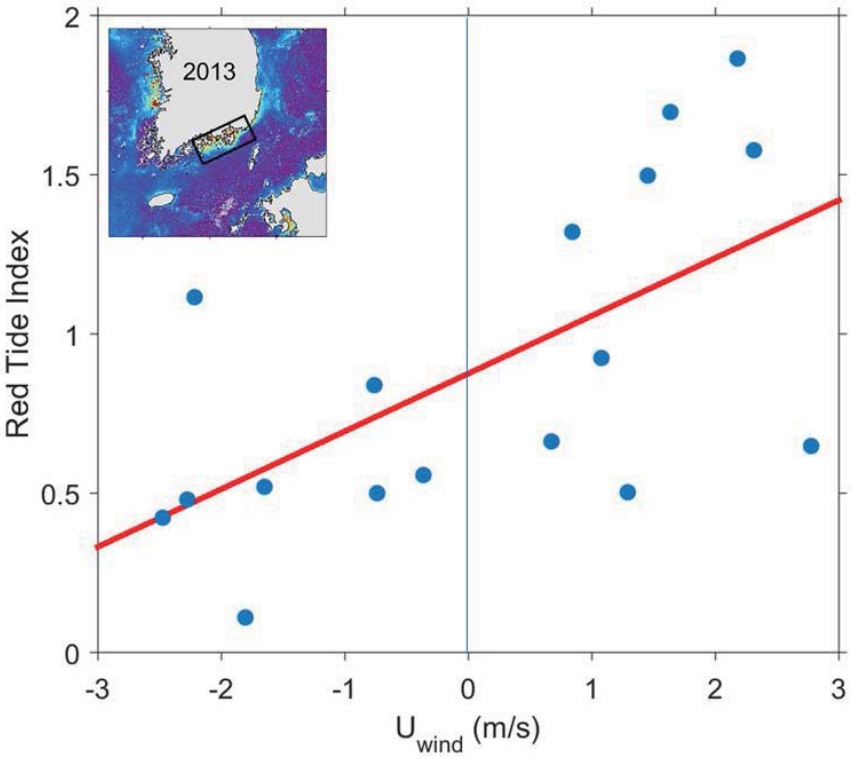

Fig. 40. RTI spatial mean of subsampled area along the southern coast of Korea presented as a function of Uwind from 2011 to 2016.

Chapter 5. Discussion

5.1. In-situ Measurement Data and RTI Validation

Usually, red tides reveal the line-shaped features in seas, and their spatial distribution can be observed from high-resolution satellite images, such as those provided by Landsat OLI (Figs. 41a and b). GOCI can observe the features with an accuracy of up to 1 km (Fig. 41c). In order to validate the RTI, the in-situ red tide report map provided by NIFS was digitized to create a database. However, the regions in which the red tide appeared were denoted by an ambiguous ellipse and the in-situ red tide density is a representative value for a wide area of the coastal region, over tens of kilometers, and not for each ellipse (Figs. 41d and e). This ambiguity can cause an uncertainty in the estimation of the location and intensity of the red tide using satellite data. On comparing Figs. 41b and e, it can be seen that while the red tide features obtained from satellite images are spatially distributed with a unit of tens of meters, the NIFS map expresses the red tide points roughly based on the inputs of local researchers or fishermen. The relationship between RTI and the in-situ red tide density is shown in Fig. 10. It shows a wide range of mean standard deviation due to the lack of a matchup database. For

this reason, the red tide index, instead of the red tide density, was utilized to reveal the spatial and temporal variations of the red tide. The threshold determined as 0.2 RTI value has to be identified what circumstance this value indicates.

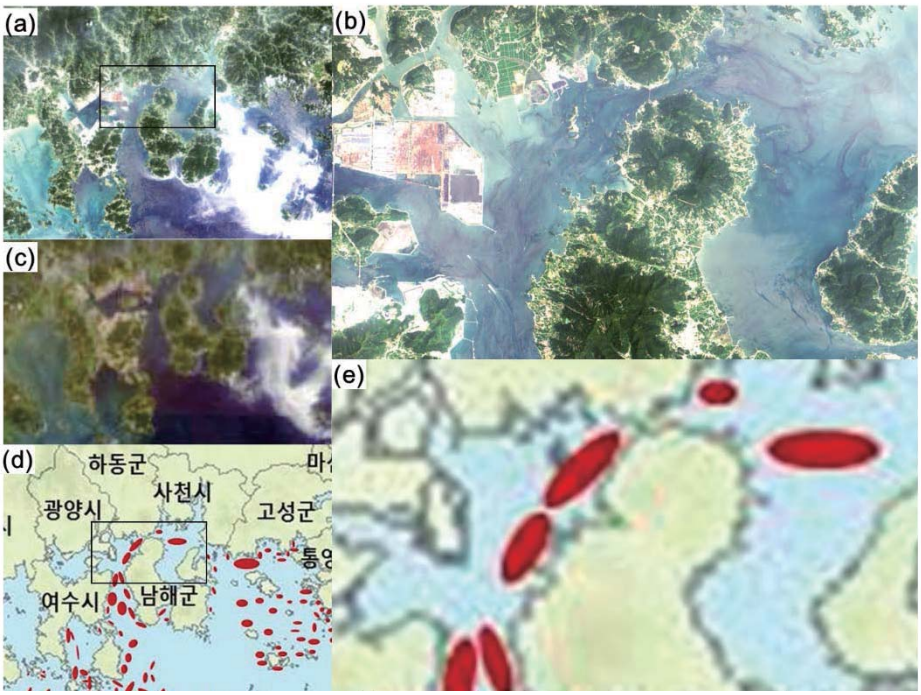

Fig. 41. (a) Landsat OLI, (b) enlarged image of the black box in (a), (c) GOCI RGB image, (d) NIFS red tide report map, and (e) enlarged image of the black box in (d) on August 8, 2013. Red ellipse indicates the region where red tide was observed.

5.2 Satellite Sensor-Generated Problems

Due to the problems with the instruments in the satellite vehicle, there is a slot difference between adjacent slots in GOCI (Kim et al., 2015). This can cause an uncertainty in the dataset, which results in spatial disconnection, leading to a reduction in the spatial consistency. It needs to be verified whether this affects the calculation of red tide index. Since this type of error is amplified by the presence of water vapor or thin small clouds (Part II), high-accuracy atmospheric correction should be applied to the GOCI data. The GOCI shows spatially averaged data with sub-kilometer unit features, when compared to Fig. 41b. Although it is an inevitable limitation, it need to be confirmed the relationships between RTI and when GOCI can detect red tide as how fraction red tide occupied the region. Despite these uncertainties, GOCI provides an unprecedented chance to reveal the ecology and phenology of red tide and diurnal variations through the 2-dimensional time series data.

5.3 Limitation of RTI Index

The spectral distribution of oceans include the effect of ocean color parameters such as SPM, Chl-a, CDOM, red tide, and green tide. In order to detect red tides with high accuracy, the original signals of the red tide should be subtracted from the natural reflectance of the ocean. As shown in Fig. 13, CDOM and Chl-a affect the height of the spectral peak. CDOM and Chl-a show a strong positive correlation with RTI; when RTI is high, CDOM and Chl-a are also high. CDOM is generated by the metabolism of red tide bloom and the Chl-a concentration is attributed to the photosynthesis of red tide. However, it is not a necessary and sufficient condition, since there is a possibility of exceptions. In-situ measurements of these parameters are required for obtaining their spectral characteristics. There are various algorithms for Chl-a, CDOM, and SPM. As seen in Fig. 42, two different Chl-a concentration maps show significantly different spatial patterns and absolute values. In the case of CDOM, considerable difference can be observed, especially in the East Sea. Therefore, the proper selection of ocean color parameters is the key to reveal the relation between RTI and other ocean color parameters. In order to test the performance of RTI in areas with turbid water, the red tide region in Goheung, which has highly turbid water, was chosen as an example, as shown in Fig. 43. In the regions with turbid water, RTI showed high values for the areas where the NIFS map

reported the occurrence of red tide. Apart from the red tide features of these coastal areas, the RTI also reveals those along the 34 ° N latitude.

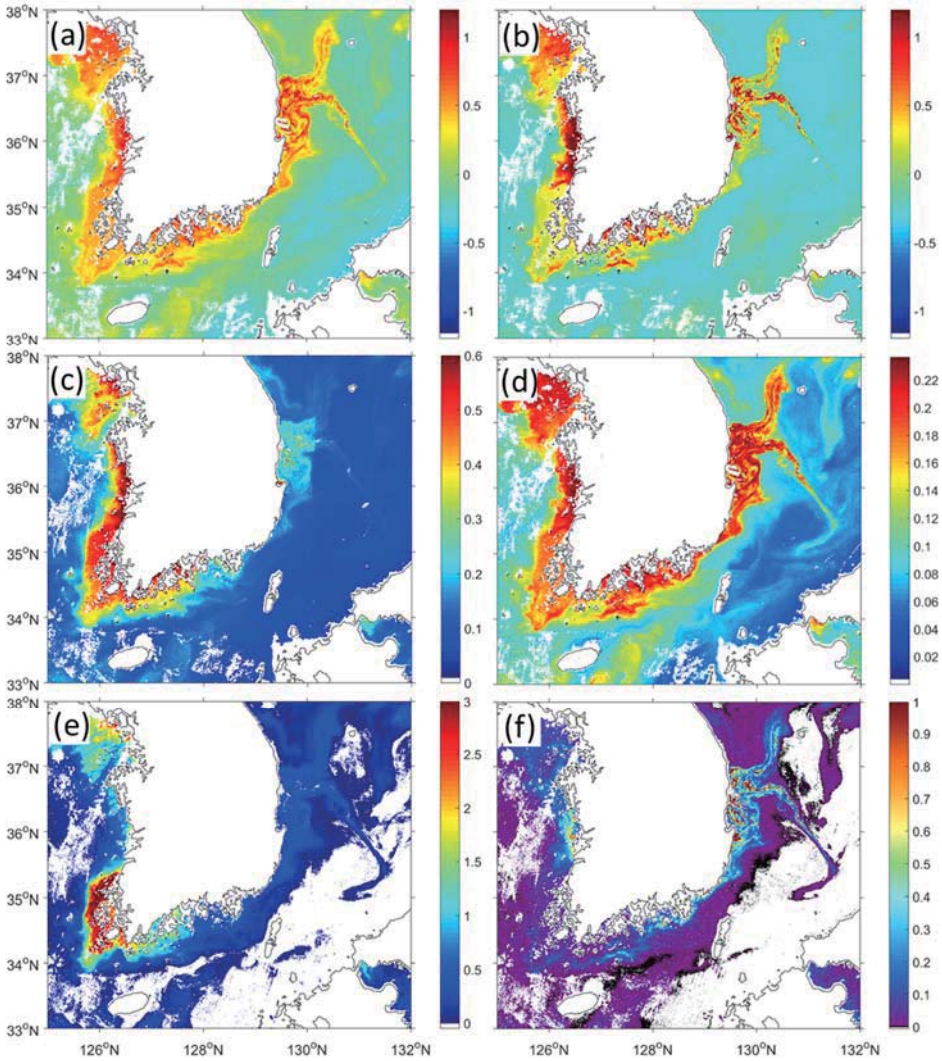

Fig. 42. Spatial distribution of chlorophyll-a concentration estimated by (a) OC3, (b) YOC algorithm, (c) CDOM absorption rate by Moon et al.,(2010), (d) YOC algorithm, (e) SPM by YOC algorithm, and (f) red tide index.

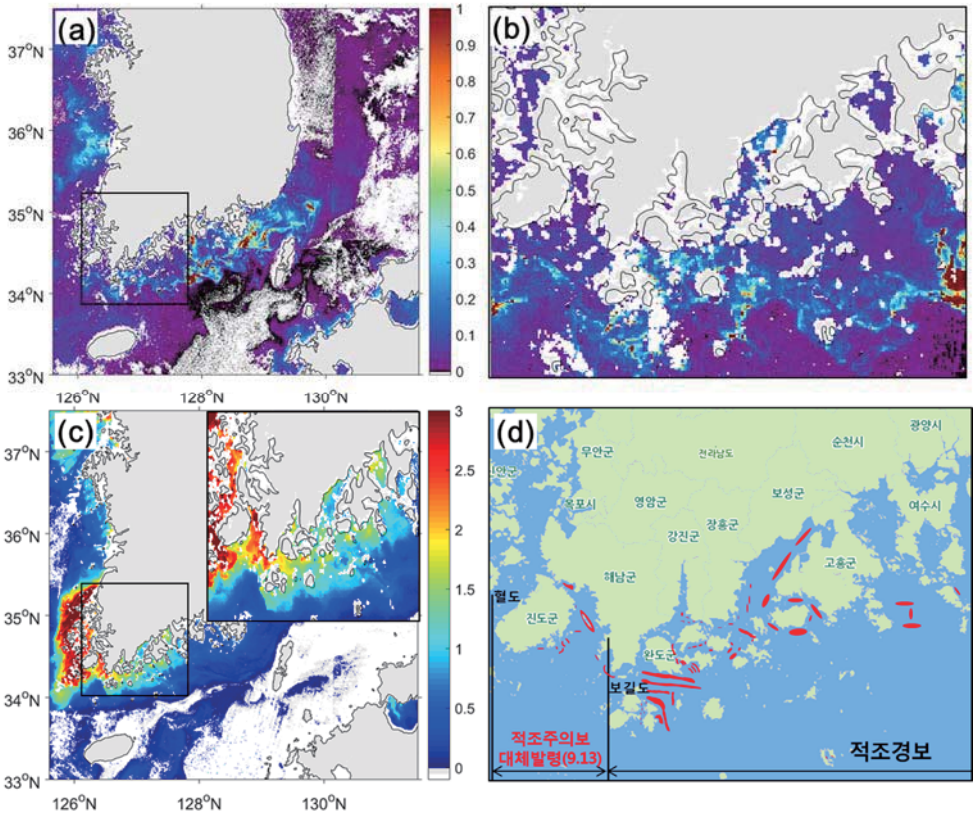

Fig. 43. (a) Red Tide Index, (b) enlarged image of box in (a), (c) Suspended Particulate Matter (SPM) concentration and its enlarged image of box, and (d) NIFS red tide report map on September 13, 2015. Red region indicates the areas where red tide bloom was observed.

5.4 Red Tide Species around Jeju

Previous researches have reported that new tropical red tide species were found (Fig. 36). As all these species are constituents of red tide, their spectral characteristics are assumed to be similar to each other. However, the damage caused by each species is different; therefore, a discrimination between the different red tide species is required. The in-situ measurement of red tide species is crucial to differentiate between the various species and a periodic long-term monitoring of the region is needed to develop the knowledge about red tide.

5.5 Case of Yellow Sea

Although, the red tide in Yellow Sea is rarely issued, a strong indication of the presence of red tide in this region was obtained using RTI. In 2012 and 2013, a strong red tide flourished near Taean and Seosan, and damaged the fish farming cages in those regions (http://www.greenpostkorea.co.kr/news/article.html?no=18841, Fig. 44). The fishermen who were eyewitnesses of this incident in the Yellow Sea often addressed the fishing community. It is necessary to inspect the characteristics such as geological bottom reflectance or color, and the ecological system of the region near Saemangeum Bank.

Fig. 44. Spatial distribution of in-situ red tide mapped by NIFS near around the western coast of Korea.

5.6 Difference between Region Classifications between Scientists

Biologists have a tendency to refer to the inner bay as onshore and the other regions as offshore. However, it is difficult to detect oceanic signals from regions too close to the inner bay, using remote sensing satellites. If the standards of inner region, onshore, and offshore region are established, it would be possible for the biologists and users of remote sensing satellites to work together and share research results. High-resolution satellite data, such as that from Landsat OLI, is necessary to observe the inner regions, where biologists prefer to do research. It shows the detailed patterns of the ocean coloring phenomena (Fig. 41). However, it is not equipped with specific near IR channels that are capable of detecting the second peak of the red tide at 680 nm (Fig. 45). Therefore, a different method to detect red tides is required. By using neural networks or utilizing the first peak of the red tide at 555 nm, it is possible to detect red tide with high-resolution satellite data, even though there are some limitations such as coarse visiting period and a difficulty in confirming the detection results scientifically.

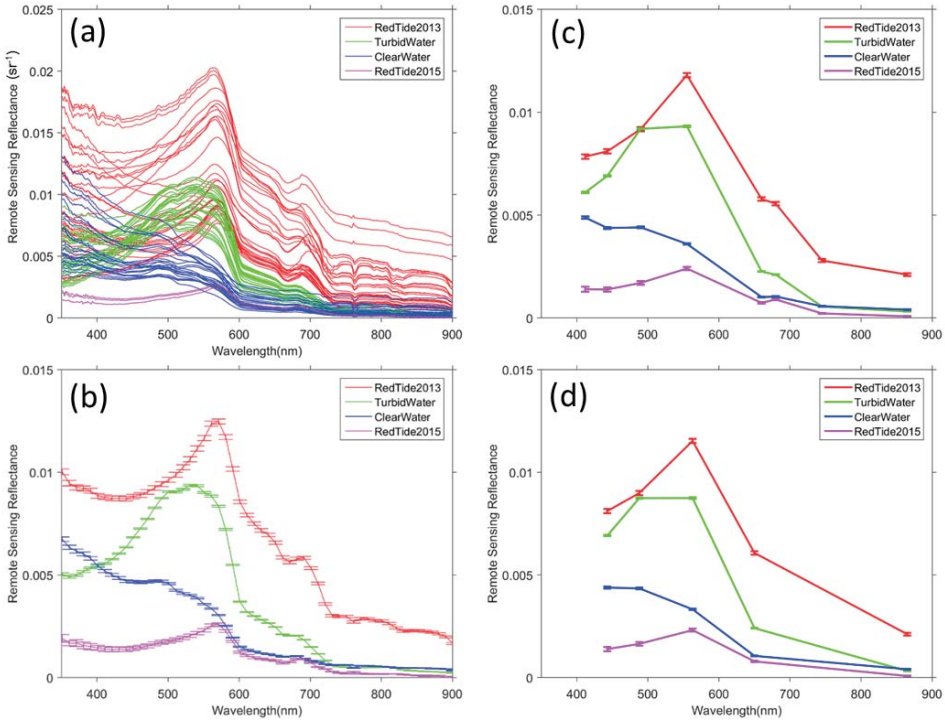

Fig. 45. (a) same as Fig. 3 (b) mean error bar of (a), remote sensing reflectance of (a) by applying (c) GOCI, (d) Landsat OLI spectral response function as a function of observation wavelengths.

5.7. Yangtze River Discharge

After the construction of the Three Gorges Dam in the Yangtze River, its flux has decreased and the composition of the water flowing into the Yellow Sea has changed. The green tides became stronger and their frequency became higher (Son et al., 2012, Fig. 45). In addition, dinoflagellates, which are strong in Si limited condition, have bloomed continuously. Although it is certain that the Yangtze River discharge affects the regions near Korea, it has not been clearly researched where and how it will affect. In 2016, there was flood in China and a large amount of water, which was 1.5−2 times higher than usual, was discharged. It took a month for the unusually turbid water to reach Jeju from the mouth of the Yangtze River. It is necessary to research the effect of the highly turbid and low−salt sea water on the ecosystem of the southern coast and Jeju Island, in order to be prepared for such situations in future.

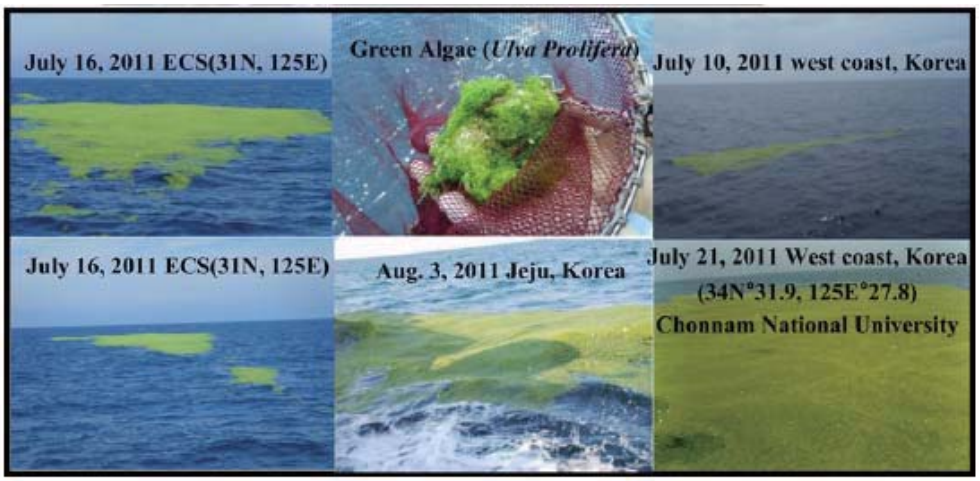

Fig. 46. Green tide near the western coast of Jeju island in 2011 (Son et al., 2012).

5.8 Further Study

The most important and crucial issue for utilizing RTI to study red tide is its validation in regions where the presence of red tide bloom is not well-known. Apart from the southern and eastern coasts, red tide index show high values in the western coast, near Jeju Island, and offshore. As these regions have relatively lower density of cage fishery farms than the southern coast or areas far from the land, the people and press do not take an interest in the presence of red tides in these regions. Although its ability to reveal new red tide zones needs to be confirmed, it provides new information for red tide research. If long-term nutrient data is also collected from a wide area, the effect of nutrients, oceanic parameters, and atmospheric factors on red tide can be researched with this unprecedented high-frequency 2-dimensional time series red tide data.

Chapter 6. Summary and Conclusion

We conducted in-situ measurements when red tides bloomed and elucidated the spectral characteristics of red tides. Red tides have bimodal peaks over visible wavelengths at 555 nm and 680 nm. Based on this characteristic of red tides, we developed the red tide index (RTI) and applied it to GOCI reprocessed data with speckle removal. The results of the RTI were validated with the NFRDI red tide report map and in-situ density. RTI shows a positive exponential relationship with in-situ red tide density and therefore, can be used as a representative of red tide density.

A satellite RTI database was created for the period from 2011 to 2016 from GOCI observations. There are annual spatial variations in RTI. In 2013, when there was severe damage resulting from a red tide, RTI shows its highest value over the broadest region over the six years. Along or across the coast, we can discover the movement of red tides and calculate their velocity by radon transform. The maximum annual RTI values and their time of occurrence reveals the advection of red tide intensity. Red tide patterns move from the southern coast to the eastern coast or eastward or northward. Using the dates when RTI is greater than a threshold value, the duration of a red tide is estimated. When damage was severe, the region with long duration also covered a wide area and the red tide started earlier than usual.

Red tide density is known to fluctuate daily. Satellite RTI also shows diurnal variation and its patterns coincide with in-situ measurements. Although the information on red tides around Jeju Island is not provided by NFRDI, we identified the probability of red tide appearance based on in-situ measurements from previous research. There are several potential parameters that can affect the progression of a red tide. Among them, one week-delayed RTI shows a positive relationship with wind across the coast and a negative relationship with cloudiness in the southern coastal area. Where red tides bloom, CDOM and Chl-a concentration show strong positive relationships with RTI. However, these are not the only necessary conditions. Red tides were most frequent when SST was 20.5 ℃ or 24.5 ℃.

Unprecedented high-resolution RTI data were calculated. Utilizing this database, we can monitor red tides offshore, where humans cannot frequently observe. If we know the phenology or location of a red tide before it reaches the coastal area, then the fishing industry can prepare for an emergency situation. It is anticipated that this approach can improve research by revealing the relationship between red tides and the factors that may affect their occurrence. Further survey based on in-situ measurements is necessary for verifying less known red tide events that were observed in the satellite data (e.g., blooms observed off shore, west coast area near Saemangeum, and East sea). These case studies will shed light on new research

directions for previously unreported events of red tide.

References

Ahn, Y.H., and Shanmugam, P., 2006. Detecting the red tide algal blooms from satellite ocean color observations in optically complex Northeast-Asia coastal waters. *Remote Sensing of Environment*, 103(4), 419-437.

Ahn, Y.H., Shanmugam, P., Ryu, J.H., and Jeong, J.C., 2006. Satellite detection of harmful algal bloom occurrences in Korean waters. *Harmful Algae*, 5(2), 213-231.

Amin, R., Zhou, J., Gilerson, A., Gross, B., Moshary, F., and Ahmed, S., 2009. Novel optical techniques for detecting and classifying toxic dinoflagellate Karenia brevis blooms using satellite imagery. *Optics express*, 17(11), 9126-9144.

Binding C., Greenberg, C., Bukata, B., Watson, S., Rastin, S., and Gould, J., 2012. Monitoring algal blooms using the MERIS maximum chlorophyll index. *In Proceedings of Workshop for remote sensing of coastal and inland waters, University of Wisconsin-Madison*.

Cannizzaro, J.P., Carder, K.L., Chen, F.R., Heil, C.A., and Vargo, G.A., 2008. A novel technique for detection of the toxic dinoflagellate, Karenia brevis, in the Gulf of Mexico from remotely sensed ocean color data. *Continental Shelf Research*, 28(1), 137-158.

Choi, J.K., Min, J.E., Noh, J.H., Han, T.H., Yoon, S., Park, Y. J., Moon, J.-E., Ahn, J.-H., Ahn, S.M., and Park, J.H., 2014. Harmful algal bloom (HAB) in the East Sea identified by the Geostationary Ocean Color Imager (GOCI). *Harmful Algae*, *39*, 295-302.

Chu, P.C., and Kuo, Y.H., 2010. Detection of red tides in the Southwestern Florida coastal region using ocean color data. *In Proceedings on MTS/IEEE OCEANS 10, Seattle, Washington, USA,* 1001-1006.

Gobler, C.J., Berry, D.L., Anderson, O.R., Burson, A., Koch, F., Rodgers, B.S., Moore, L.K., Goleski, J.A., Allam, B., Bowser, P., Tang, Y., and Nuzzi, R., 2008. Characterization, dynamics, and ecological impacts of harmful Cochlodinium polykrikoides

blooms on eastern Long Island, NY, USA. *Harmful Algae*, 7(3), 293-307.

Gower, J.F.R., 1994. Red tide monitoring using AVHRR HRPT imagery from a local receiver. *Remote Sensing of Environment*, 48(3), 309-318.

Gower, J.F.R., Doerffer, R., and Borstad, G.A., 1999. Interpretation of the 685nm peak in water-leaving radiance spectra in terms of fluorescence, absorption and scattering, and its observation by MERIS. *International Journal of Remote Sensing*, 20(9), 1771-1786. doi:10.1080/014311699212470.

Ishizaka, J., Kitaura, Y., Touke, Y., Sasaki, H., Tanaka, A., Murakami, H., Suzuki, T., Matsuoka, K., and Nakata, H., 2006. Satellite detection of red tide in Ariake Sound, 1998-2001. *Journal of Oceanography*, 62(1), 37-45.

Kim, D.I., Matsuyama, Y., Nagasoe, S., Yamaguchi, M., Yoon, Y.H., Oshima, Y., Imada, N., and Honjo, T., 2004. Effects of temperature, salinity and irradiance on the growth of the harmful red tide dinoflagellate ochlodinium polykrikoides Margalef (Dinophyceae). *Journal of Plankton Research*, 26(1), 61-66.

Kim, D.W., Jo, Y.H., Choi, J.K., Choi, J.G., and Bi, H., 2016. Physical processes leading to the development of an anomalously large Cochlodinium polykrikoides bloom in the East sea/Japan sea. *Harmful Algae*, 55, 250-258.

Kim, G., Lee, Y.W., Joung, D.J., Kim, K.R., and Kim, K., 2006. Real-time monitoring of nutrient concentrations and red-tide outbreaks in the southern sea of Korea. *Geophysical research letters*, 33, L13607. doi:10.1029/2005GL025431.

Kim, Y., Byun, Y., Kim, Y., and Eo, Y., 2009. Detection of Cochlodinium polykrikoides red tide based on two-stage filtering using MODIS data. *Desalination*, 249(3), 1171-1179.

Lee, Y.W., Kim, G., Lim, W.A., and Hwang, D.W., 2010. A relationship between submarine-groundwater borne nutrients traced by Ra isotopes and the intensity of dinoflagellate red-tides occurring

in the southern sea of Korea. *Limnology and oceanography*, 55(1), 1-10.

Lou, X., and Hu, C., 2014. Diurnal changes of a harmful algal bloom in the East China Sea: Observations from GOCI. *Remote Sensing of Environment*, 140, 562-572.

Matthews, M.W., Bernard, S., and Robertson, L., 2012. An algorithm for detecting trophic status (chlorophyll-a), cyanobacterial-dominance, surface scums and floating vegetation in inland and coastal waters. *Remote Sensing of Environment*, 124, 637-652.

Park, J.G., Jeong, M.K., Lee, J.A., Cho, K.-J., and Kwon, O.-S., 200l. Diurnal vertical migration of a harmful dinoflagellate, Cochlodinium polykrikoides (Dinophyceae), during a red tide in coastal waters of Namhae Island, Korea. *Phycologia*, 40, 292-297.

Shah, M., Mahfuzur, R., An, S.J., and Lee, J.B., 2013. Presence of benthic dinoflagellates around coastal waters of Jeju Island including newly recorded species. *Journal of Ecology and Environment*, 36(4), 347-370.

Shanmugam, P., Ahn, Y.H., and Ram, P.S., 2008. SeaWiFS sensing of hazardous algal blooms and their underlying mechanisms in shelf-slope waters of the Northwest Pacific during summer. *Remote Sensing of Environment*, 112(7), 3248-3270.

Siswanto, E., Tang, J., Yamaguchi, H., Yuhwan, A., Ishizaka, J., Yoo, S., Sangwoo, K., Kiyomoto, Y., Yamada, K., Chiang, and C., Kawamura, H., Empirical ocean-color algorithms to retrieve chlorophyll-a, total suspended matter, and colored dissolved organic matter absorption coefficient in the Yellow and East China Seas. Journal of Oceanography. 2011, 67, 627–650.

Tang, D., Kawamura, H., and Baker, J., 2006. Satellite evidence of harmful algal blooms and related oceanographic features in the Bohai Sea during autumn 1998. *Advances in Space Research*, 37(4), 681-689.

Tomas, C.R., and Smayda, T.J., 2008. Red tide blooms of Cochlodinium polykrikoides in a coastal cove. *Harmful Algae*,

7(3), 308-317.

Wei, G., Tang, D., and Wang, S., 2008. Distribution of chlorophyll and harmful algal blooms (HABs): a review on space based studies in the coastal environments of Chinese marginal seas. *Advances in Space Research*, 41(1), 12-19.

Yoon, Y.H., Rho, H.K., and Kim,Y.G., 1991. Red tide organisms in the coastal waters of Cheju island, Southern Korea. *Bull, Mar, Res. Inst Cheju Nat. Univ.,* 15, 1-14.

국문초록

고해상도 광학위성을 이용하여 연안에서의 기름유출 공간분포와 시간에 따른 분산을 조사하였다. 기름 유출을 탐지하기 위하여 인공신경망기법을 Landsat과 DubaiSat-2에 적용하였다. 기름유출해역과 기름이 없는 해역의 스펙트럼 특성을 측정하는 현장관측을 수행하였다. 위성영상에서 선박과 선박의 그림자에 해당하는 화소를 탐지하고 제거할 수 있었고, 기름탐지 성공 결과를 내었다. 근적외 채널을 활용하여 인공신경망기법을 반복하며 기름 종류를 두껍거나 필름 같은 얇은 형태의 기름으로 구별하는 새로운 기법을 개발하고 그 면적을 추정하였다. 유출된 기름의 시간에 따른 이동의 가능한 원인을 이해하기 위하여, 대기와 해양 입력장으로 수치모델을 수행하였다. 전체적으로, 조류에 의해 이동하는 기름입자의 궤적이 위성영상 기름탐지 결과와 잘 부합함을 보였다. 위성자료와 조류만을 고려한 모델수행 결과 사이에 약간의 차이가 발생하였는데, 특히 유막 형태의 기름이 남동방향으로 이동하거나 해협의 안쪽인 북쪽으로 이동한 것이었다. 이는 바람에 의한 에크만류에 의한 것이다. 이 연구는 연구해역인 만에서 바람이 약할 때, 기본적으로 조류가 기름의 시간변동에 중요한 역할을 하였으며, 바람이 강하고 조류가 강한 시기에는 에크만류가 기름의 이동을 주로 제어하였다는 것을 제시하였다.

정지궤도해색위성의 부유사자료에 나타나는 스펙클을 시공간적으로 분석하였다. 스펙클은 네가지 형태: 고립된 형태, 구름주변에서 나타나는 경우, 패치 모양으로 나타나는 경우와 슬랏과 관련되어 나타나는 경우로 구분되었다. 스펙클을 제거하기 위하여 스펙클 탐지 및 분류 과정을

개발하였다. 스펙클 제거는 정지궤도해색위성의 부유사농도 자료의 질을 향상시켰다. 스펙클의 광학적 특성을 통해 가능한 스펙클 발생 원인을 제시하였다. 완벽하게 제거되지 않은 구름 주변부와 수증기, 위성의 채널별 관측 중 움직인 작은 구름에 의해 스펙클이 생기는 것으로 결론지었다.

한반도 주변해에서의 현장관측을 통하여, 적조가 555nm, 680nm 에서 두개의 최고값을 보이는 이정곡선 형태의 광학특성을 갖는다는 것을 발견하였다. 적조지수 알고리즘을 적조를 실측한 스펙트럼의 광학특성에 기반하여 개발하였고, 적조 실측 자료에 대하여 검증하였다. 적조지수 알고리즘을 2011년부터 2016년까지 스펙클이 제거된 정지궤도해색위성자료에 적용되었다. 번성시작 시기, 소강시기, 지속기간, 발생확률의 공간분포와 같은 적조의 특성을 위성 적조지수 자료를 이용하여 추정하였다. 해안선에 나란하거나 수직한 방향으로의 적조의 이동과 전파를 시간적 공간적으로 조사하였다. 적조지수와 해수면온도, 운량, 해수면 바람, 강유량, 유색용존유기물, 클로로필-a, 부유물질과 같은 환경인자와의 관계를 밝혔다.

주요어: 기름유출, 스펙클, 적조, 광학현상, 위성원격탐사, 정지궤도해색위성

학 번: 2011-30457